Phase I Final Report

THE DEVELOPMENT OF LOW-COST INTEGRATED COMPOSITE SEAL FOR SOFC: MATERIALS AND DESIGN METHODOLOGIES

Reporting Period:
Sept 04~Oct 06

Principal Authors:
Xinyu Huang
Kristoffer Ridgeway
Srivatsan Narasimhan
Serg Timin
Wei Huang
Didem Ozevin (PAC)
Ken Reifsnider

Report Issued:
Oct 2006

DOE Award Number:
DE-FC26-04NT42228

Connecticut Global Fuel Cell Center
University of Connecticut
44 Weaver Rd, Unit 5233, Storrs CT 06269

DISCLAIMER

ABSTRACT

This report summarizes the work conducted by UConn SOFC seal development team during the Phase I program and no cost extension. The work included composite seal sample fabrication, materials characterizations, leak testing, mechanical strength testing, chemical stability study and acoustic-based diagnostic methods. Materials characterization work revealed a set of attractive material properties including low bulk permeability, high electrical resistivity, good mechanical robustness. Composite seal samples made of a number of glasses and metallic fillers were tested for sealing performance under steady state and thermal cycling conditions. Mechanical testing included static strength (pull out) and interfacial fracture toughness measurements. Chemically stability study evaluated composite seal material stability after aging at 800ºC for 168 hrs. Acoustic based diagnostic test was conducted to help detect and understand the micro-cracking processes during thermal cycling test. The composite seal concept was successfully demonstrated and a set of material (coating composition & fillers) were identified to have excellent thermal cycling performance.

TABLE OF CONTENTS

1. EXECUTIVE SUMMARY

UConn SOFC seal development team has conceived and demonstrated a multilayered composite seal concept that relies on a three-layer structure deposited by plasma spray to satisfy the requirement of a SOFC seal. Part of the seal or complete seal (including filler glass) can be an integrated part fabricated directly onto interconnects. Low cost materials were selected to produce the structure and high throughput automated atmospheric plasma spray can be used to fabricate the seal. The phase I work has demonstrated the concept based on sub-scale "button" samples. The work included materials characterization, leak performance test, mechanical test, chemically stability study, and acoustic-emission based diagnostics.

Materials characterization revealed a set of desirable properties suitable for SOFC seal applications. The thin refractory ceramic layer (Al_2O_3 & YSZ over bond coat) deposited on interconnect was found to have excellent adhesion to the substrate (pull out strength ~31MPa). SEM and XRD results showed that the ceramic layer itself is a composite of polycrystalline zirconia (tetragonal phase) and alumina (cubic phase). There exists a unique micro-cracked and somewhat porous microstructure consists of flattened splats. This morphology imparts excellent thermal shock resistance. However, the porosity does not seem to generate extensive continuous leak path as proved by the low bulk permeability measured. The coating layer also demonstrated a unique elastic anisotropy. Specifically, the through the thickness elastic modulus is other the order of 20GPa. The high through-the-thickness compliance ceramic layer will help maintain the bolt load during thermo-cycling and long term service. In contrast, the higher in-plane modulus and relative low CTE of the ceramic constituents will help reduced the effective CTE of the interconnect alloy and thus reduced CTE mismatch. The refractory ceramic layer was also found to have adequate high temperature area specific resistivity and good wetting to glasses. Certain glass that did not bond strongly the Fe-Cr alloys was found to form strong bond between ceramic coated Fe-Cr substrates because of the good surface wetting properties. A ceramic coating composition that results in good overall properties was selected as a standard composition for Phase II work. The functional performance of the composite seal was demonstrated in leak testing at steady state and thermo-cycling conditions. A sophisticated SOFC leak test stand was implemented to enable the leak testing. A total of 5 glass compositions (4 from SECA peers and one from commercial sources) and a metallic gasket were tried out in the leak testing. The initial sealing performance for almost all fillers was satisfactory based on the SECA initial leak performance target. However, the thermo-cycling resistance varied significantly. Two out 5 samples based on glass filler were found to fail in the very first thermal cycle, one can sustain about 10 cycles and another can sustain over 60 cycles. The composite seal with a metallic gasket was found to have gradually improving sealing performance with the number of thermo-cycles. Two types of composite seal have shown excellent thermo-cycling resistance. In the Phase I work, mechanical testing included tensile adhesion test and interfacial fracture toughness test using composite

beam samples. The tensile strength for one glass based composite seal was found to be around 17MPa. The interfacial toughness was found to depend on loading conditions such as opening or shear. The resistance to crack propagation was found to be about four time higher if loaded in shear as compared to loaded in tension (opening). Finite element modeling of interfacial crack in the composite seal was used to calculate the fracture driving force. The numerical model took into account the elastic properties of glass layer, ceramic layer and the metallic layer. The calculated strain energy released rate compared favorable with experimental results. Chemically stability study evaluated composite seal material stability after aging at 800ºC for 168 hrs. No significantly interaction between glass and metallic substrate was observed after aging. Acoustic emission and acousto-ultrasound based diagnostic techniques was used to help understand the process during thermo-cycling test. Method to extract macro-cracking events was demonstrated. Attempt was also make to locate the cracking event in a seal sample. A test conducted at room temperature successfully demonstrated the location method.

In summary, the UConn team through Phase I work has demonstrated a composite seal concept. Extensive material characterization work has helped us better understood structure-property relationship for material properties relevant to seal applications. As a result of characterization and screening test, a composition of ceramic layer was determined for future work. Based on the leak test, two filler candidates were found to have excellent thermo-cycling resistance. Mechanical testing and modeling and acoustic based diagnostic have shed light on mechanical failure resistance and will serve as the basis for further research to enable seal design based on analysis.

2. FABRICATION & CHARACTERIZATION

Concept

SOFC sealing material must meet complex set of requirements [1], including good wetability to adherends, good chemical compatibility, good match of coefficients of thermal expansion, high electrical resistivity, etc. In addition, the aggregated material and fabrication cost of seals has to be low to ensure commercial viability. Existing glass and glass ceramic seals have shown limited failure resistance under thermo-cycling conditions. In long term service, chemical interactions [2] between sealing glass and Fe-Cr based interconnect materials sometimes results in a weakened interface. Compressive seals based on mica [3] have been shown to have excellent thermo-cycling stability. However, they require expensive high-temperature load-frame to maintain a high compressive force. The authors believe that it is unlikely that such a large set of suitable mechanical/physical/chemical properties for SOFC seal occur in one material. In an attempt to break through the current technical barriers related to SOFC seals, the authors are investigating a novel integrated composite seal concept (material and structure) and its associated thermal mechanical design methodologies.

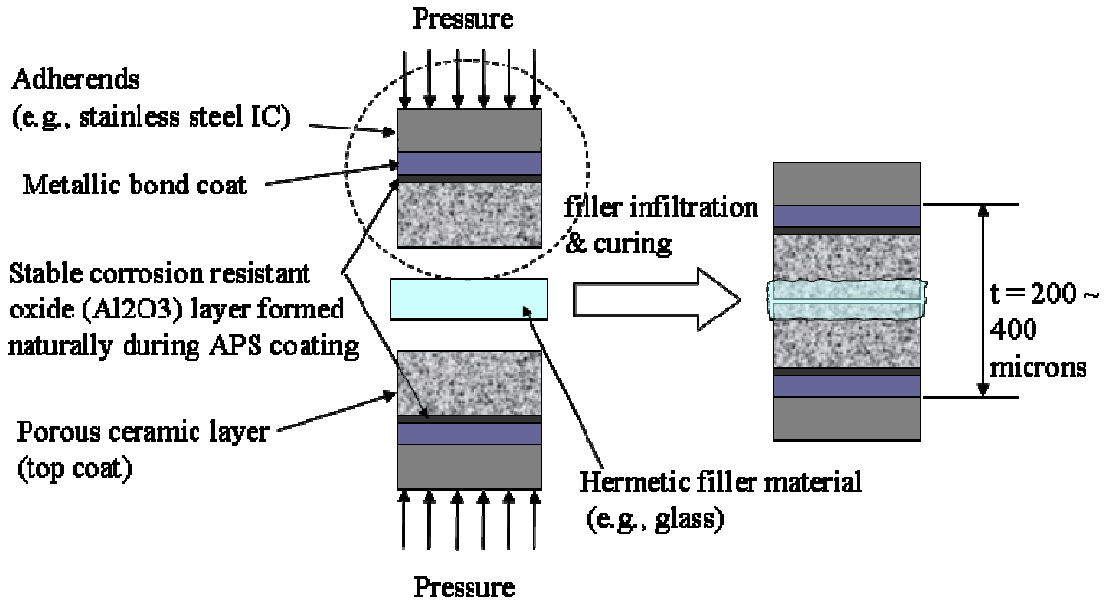

Figure 1. Schematic of the conceptual structure of the integrated composite seal. Shown here is an interconnect-to-interconnect seal.

The approach being pursued is to engineer composites of multiple constituent materials or ingredients. The authors are investigating a multilayered composite seal structure (Figure 1) that consists of thin layers of oxidation-resistant metals, porous ceramics, and fillers/glasses. The seal structure will be directly fabricated onto the surfaces of mating adherends using low-cost manufacturing methods such as atmospheric plasma spray (APS). Hence, a portion of the seal becomes an integrated part of the interconnect. During stack assembly, sealing can be achieved through a simple heat/pressure-assisted curing process. As such, stack cost can potentially be lowered by reducing the total number of parts and by simplifying the assembly process.

A properly designed ceramic layer in the composite structure can potentially play several important roles. It can enable a gradual transition of thermal-elastic properties from the Fe-Cr substrate to the glass fillers, alleviating stress concentrations. Because it has excellent refractory properties, a ceramic inter-layer can relax the requirements (wetting, dielectric, chemical properties, etc.) on the filler materials, such as glass. As such, many types of filler materials can be utilized in the composite seal structure, expanding the compositional space for usable filler glasses, for example. Eliminating direct contact between the glass and the Fe-Cr alloy, the ceramic layer in the composite seal will also help reducing adverse chemical interaction between filler and metal substrates, thus improving long-term stability.

To realize the above benefits derived from the composite structure, the ceramic layer (as a critical building block) should form a mechanically robust bond with the Fe-Cr substrate. It should also be electrically insulating at high temperatures The porosity and gas permeability should be low to avoid excess leaking through the bulk. The material needs to be chemically stable in contact with the filler glass. The raw materials and fabrication cost should be relatively low. A ceramic coating deposited by atmospheric plasma spray has been engineered to satisfy the above requirements. The details of fabrication, microstructure and property

characterization are presented. A composite seal incorporating a glass filler has been made and tested. Initial testing has been conducted to measure leak rate and thermo-cycling resistance.

Sample Fabrication:

The composition of the APS ceramic layer inlucde alumina (Metco 105SFP) and zirconia-8wt%yttria (Metco 204NS). To create a strong bond, a thin metallic layer (bondcoat) with the composition Ni-4.5wt%Al (Metco 450NS) was deposited on the Fe-Cr alloy substrate before applying the ceramic coat. All materials were purchased from Sulzer-Metco, NY, U.S.A. A mixed ceramic powder was made by mechanical blending of the alumina powder and zirconia-8wt%yttria powders. Coating samples with 5, 10, 20 and 40 vol% zirconia-8wt%yttria (top coat) were made for optimization purposes. Plasma spraying of the bondcoat of Ni-Al alloy and the ceramic top coatings of Al_2O_3/ZrO_2-8wt%Y_2O_3 was carried out with an automatic plasma system (Sulzer-Metco, NY, U.S.A) equiped with a 9MB plasma gun, a turntable, and a six-axis robot. Plasma spray parameters were optimized with Ar/H_2 working gases, spray distance, powder feeding rate and transverse speed for each of the feedstock materials. The alloy bondcoat and ceramic topcoat were deposited onto Fe-Cr alloy substrates with a thickness of 80-100μm and 200-350μm, respectively. A variety of coating specimens were produced for microstructure examination, physical and mechanical property evaluation, and leak testing.

Microstructure of the APS coating was characterized with Scanning Electron Microscopy (SEM). X-ray difraction (XRD) was utilzied to identify the crystalline phase structure of the ceramic top coat. The porosity of the top coat was measured using mercury intrusion porosimetry (MIP).

Scanning Electron Microcopy

A secondary electron image was taken on a fractured section of coating using a JEOL JSM5600LV SEM system. As shown in *Figure 2*, the bulk of the coating

consists of flattened “splats” with inter- and intra- splat micro-cracks, typical structure of APS ceramic coatings. The coating is fairly dense. A small amount of micro cracks (mostly in between the splats) and pores may or may not form connected leak path. For SOFC seal applications, it is necessary to characterize the porosity and permeability of the bulk of the top coat.

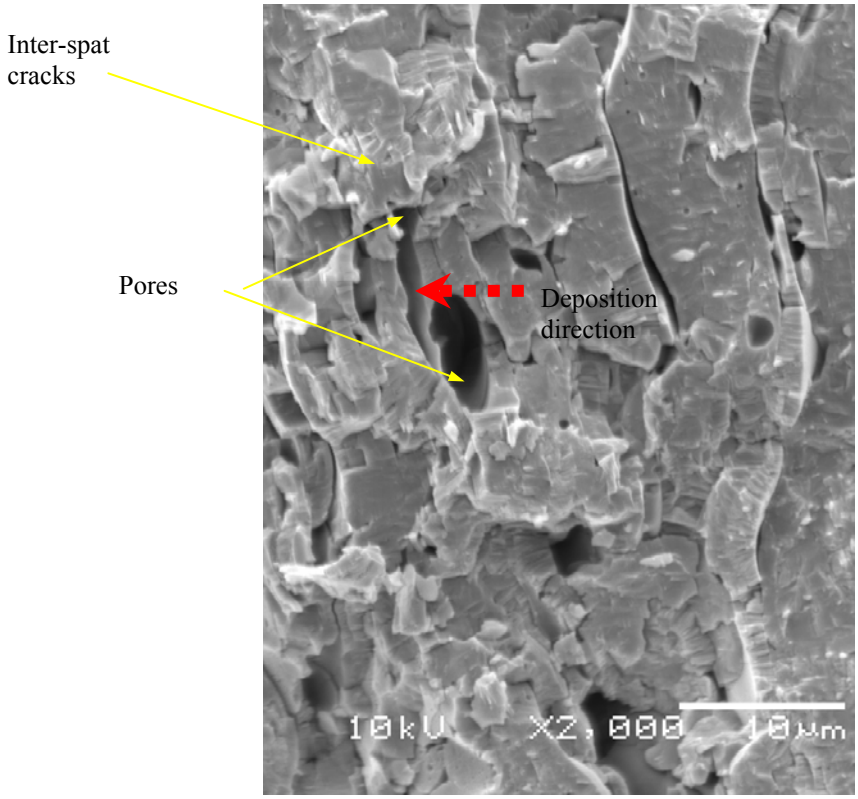

Figure 2 Secondary electron image of the fracture surface of the ceramic top coat. Pores and micro-cracks were observed.

A back-scattered electron image of polished cross section of coated substrate was obatined using a Cameca SX50 system. As shown in Figure 2, the layered strcutre was clearly displayed. In the top coat, the 8YSZ splats were seen to form elongated islands dispersed inside a matrix of alumina splats.

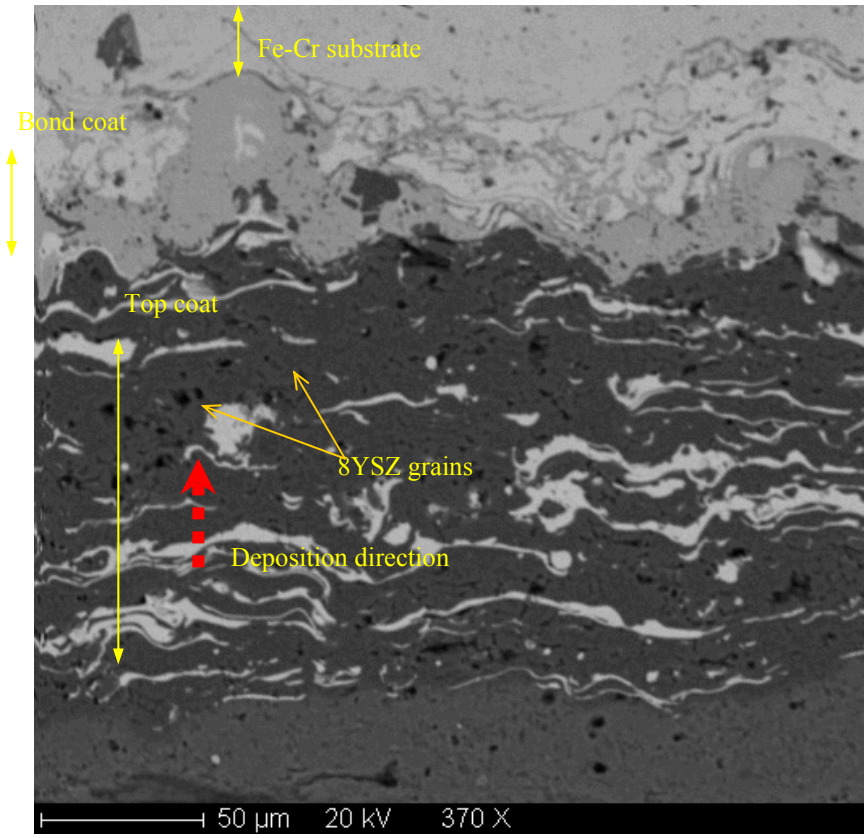

Figure 3. Back scattered electron image of the cross section of a composite seal sample. The lighter regions in the ceramic coating are YSZ splats.

XRD

The XRD analysis was performed on a Bruker D5005 Advance diffractometer. The sample was a 25.4 mm dia. disc with a 0.15mm thick ceramic layer plasma-sprayed over a Fe-Cr stainless steel substrate. The sample was aligned to be flat in a plane perpendicular to the plane of travel of the X-ray beam. It was then loaded into the diffractometer. The starting angle was 10° (2θ) and the ending angle was 100°, a range which includes most common crystalline substances. The data shown was the average of 3 continuous scans at the rate of 2°/min. Phase identification was accomplished by comparing the data (peaks and relative intensities) from the specimen with peaks and relative intensities from a large set of standard data provided by the International Center for Diffraction Data (ICDD). The phases present (*Figure 4*) were identified to be 42-1164, which is tetragonal zirconium oxide, and 10-425, which is face-centered-cubic aluminum oxide.

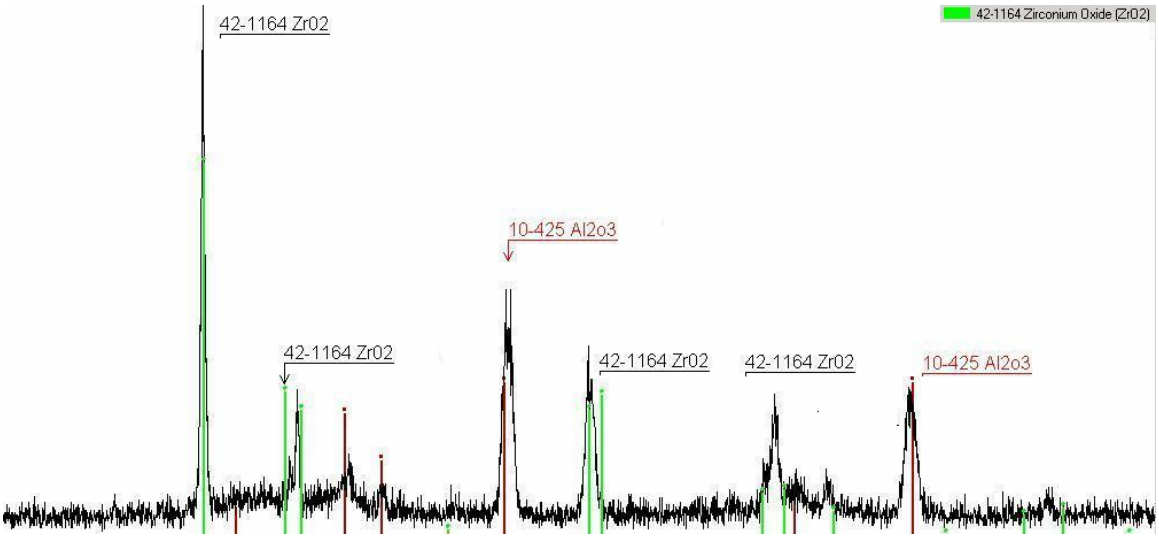

Figure 4 Powder XRD pattern for ceramic layer with phases identified. The observed peaks correspond to YSZ in tetragonal phase and alumina in cubic phase.

Porosity

A mercury intrusion porosimer (Quantachrome Corp.) was used to characterize the porosity of ceramic layers in the APS coating. A sample of metal coated with the ceramic layer was cut to a wafer of size 11.93*8.88 mm to fit the PoreMaster sample cell. The average thickness of the metal substrate was 0.587 mm, and that of the ceramic layer was 0.425 mm, which was measured using an optical microscope. The overall volume of the ceramic layer was calculated from average layer thickness to be 0.045 cc. Sample porosity was calculated by measuring intruding volume of the mercury (a non-wetting liquid) at a range of pressures, and relating the pore volume to the pore size using Washburn equation,

$$d = \frac{-4\gamma \cos\theta}{P} \qquad (2.1)$$

where ‘d’ is the diameter of the pore, ‘*P*’ is the intruding pressure, ‘γ’ is the surface tension and ‘θ’ the contact angle of the intruding fluid in contact with the sample material.

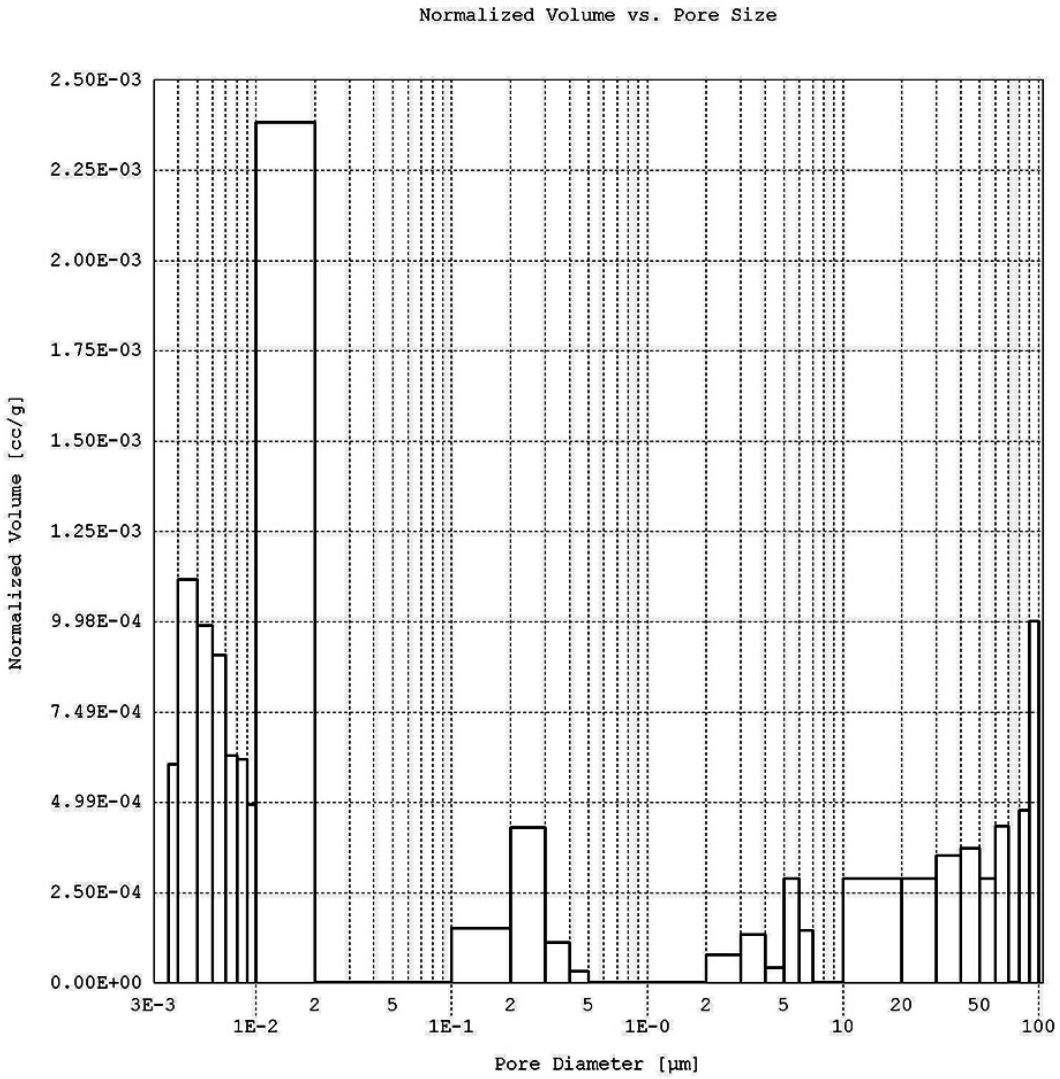

Figure 5 Pore volume distribution with respect to pore size. Three separate pore size groups can be identified.

The pore size distribution is shown in *Figure 5*. The total porosity of the coating was found to be 23.5%. However, the pore size greater than 50 microns was believed to be the contribution from asperities close to the surafce of the coating. In a composite seal, filler glass can readify infiltrate these large open pores and hence block the interfacial leaking path. The smaller intraparticle pores account for about 14.2%. It is necessary to determine if these small pores form continuous leaking paths.

Bulk Permeability

The proposed composite seal is comprised of a ferretic stainless steel substrate with a $NiAl_5$ metallic bond coat and an Al_2O_3 (80wt%) and a partially stabilized ZrO_2(20wt%) ceramic top coat. Both the top coat and the bond coat are applied using an atmospheric plasma spray (APS) process. Typical APS top coats are composed of overlapping splats oriented parallel to plane of the substrate and the coating. The resultant material has a highly anisotropic structure containing lamellar ceramic splats, intra-lamellar cracks, inter-lamellar pores and some large, irregularly shaped pores [1,2] . A schematic of the structure is show in Figure 6.

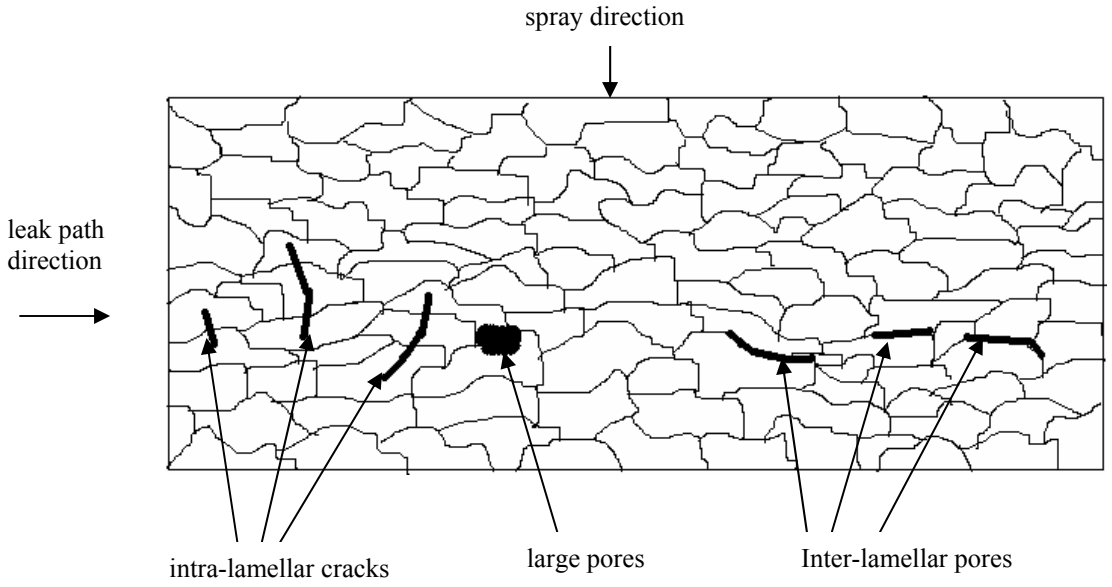

Figure 6 Atmospheric plasma spray material ceramic top coat schematic

The porosity of the top coat has been previously characterized by and the summary is shown in

Table 1. Permeability through an isotropic medium may be determined by the porosity and the geometric parameters, however, due to the inherent anisotropic structure of the top coat, the permeability through the top coat perpendicular to the spray direction can not be determined through analysis of the porosity data. The permeability for the APS coating must be determined by leak test methods in a manner similar to the actual seal application. From this, the permeability can

then be ascertained.

Table 1 Porosity summary for CGFCC APS top coat

Total Porosity	23.50	%
Interparticle Porosity	9.38	%
Intraparticle Porosity	14.12	%
Ambient Pressure	14.70	[PSIA]
Interparticle filling pressure limit	50.00	[PSIA]
Mercury surface tension	480.00	erg/cm²
Mercury contact angle (I&E)	140.00°	

To determine the permeability of the porous ceramic coating, a test cell (*Figure 7*) was constrcuted with a silicon rubber gasket sandwiched in between two coated metal disks. The sealed chamber of the cell was then pressured by helium gas and the leak rate was measrued by monitoring the steady state flow rate of the helim gas. The test was conducted at room temperature with varing applied compressive forces (P).

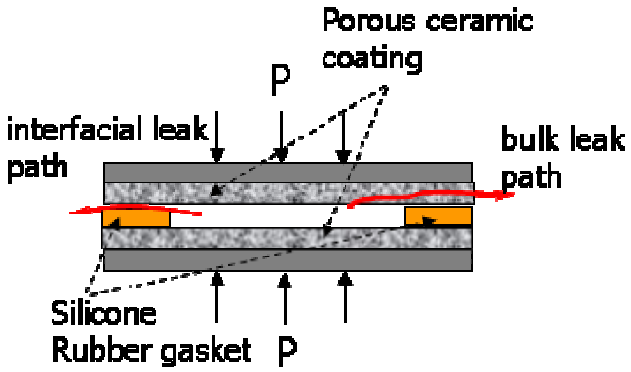

Figure 7 Test cell constructed for evaluating gas permeability of the porous ceramic coating.

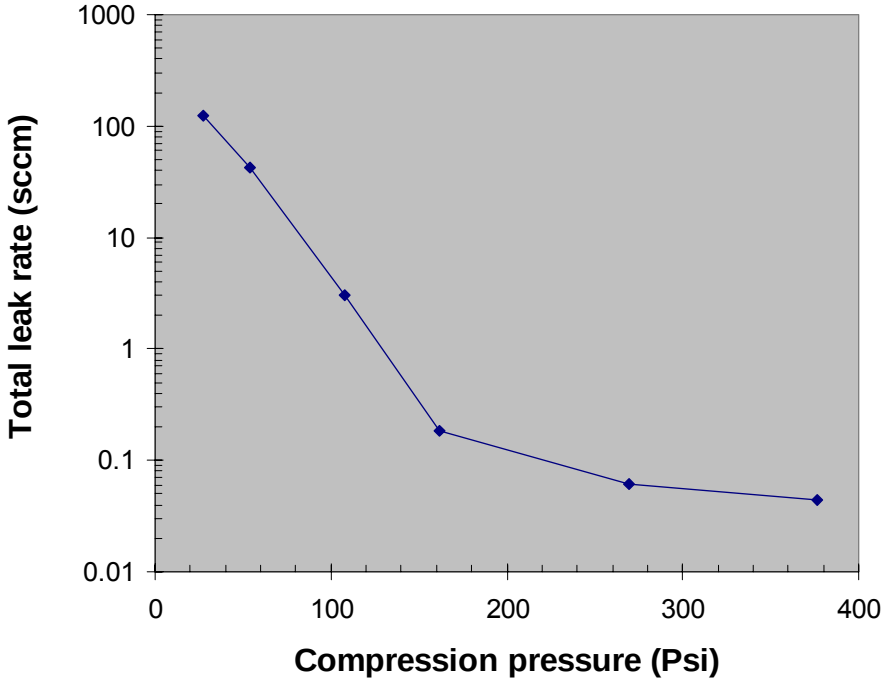

Figure 8. Gas leak rate through the coating as a function of compressive force.

With helim held at 2 Psig, the leak rate measured was found to change with applied pressure applied on the silicone gasket. The total leak rate drops about four orders of magnitude as the compressive pressure on the gasket was increased from 15 psi to 400 psi. as shown in *Figure 8.* It is believed that the leak flow switches from an interfacial path to a bulk path as the pressure on the silicone gasket is increased. Hence, the asymptote of the curve shown in *Figure 8* represents the permeability of helum gas through the bulk of the APS coating. The leak rate is negligible compared to the requirment on the leak rate of SOFC gas seals. It is thus concluded that most of the small pores in the bulk of the porous ceramic coating do not form continous leak paths.

Permeability Theory: The permeability of the coating can be measured utilizing the flow rate measurements and a variation of Darcy's equation [3]. The atmospheric plasma spray (APS) coating can be considered to be a cylinder as shown in Figure 5. The inside of the cylinder is filled with a test gas at pressure,

p_i and the gas is allowed to leak out to the atmosphere, p_o. Considering the ideal gas law and the area of a cylinder Darcy's law take the form of equation 2:

$$\frac{\dot{m}RT}{2\pi rhp} = \frac{\kappa}{\mu}\frac{dp}{dr} \tag{2.2}$$

The equation can then be solved by integrating p and r:

$$\int_{p_o}^{p_i} pdp = \int_{r_i}^{r_o} \frac{\dot{m}RT\mu}{2\kappa\pi h r} dr \tag{2.3}$$

Finally, the resultant equation can be solved for the specific permeability constant, κ:

$$\kappa = \frac{\dot{m}RT\mu}{\pi h(p_i^2 - p_o^2)} \ln\left(\frac{r_o}{r_i}\right) \tag{2.4}$$

The coefficient, κ, is an intrinsic property of the porous medium, independent of the gas properties and is expressed in units m^2 [3].

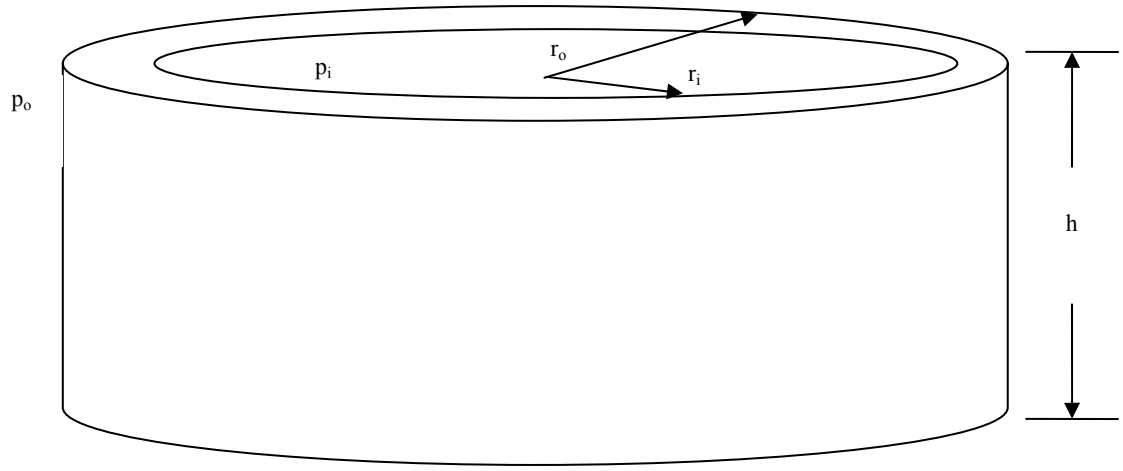

Figure 9 Schematic of APS coating

Permeability Test Procedure: A ferritic stainless steel (AL 453) substrate was coated with the standard $NiAl_5$ metallic bond coat and an Al_2O_3 (80wt%) and a partially stabilized ZrO_2(20wt%) ceramic top coat using the APS method by Inframat Corp. This sample was identical to those used in seal leak tests and contains gas ports. The sample was then adhered to a bare metal sheet of AL 453 using Magna-Tac M777 epoxy. Great care was taken to avoid blocking the

leak path through the top coat with the epoxy. This was accomplished by use of masking tape and controlling the spread of epoxy. Pressure was applied to the bonded samples using c-clamps and the sample was allowed to cure at room temperature for the recommended 24 hours. The sample was then leak tested at approximately 6,7,8,9 and 10 psi of helium using the apparatus setup according to Figure 8. This sample was then compared to the leak rate of a sample made with no coating. Since the incremental test pressures are very close to the actual gas pressure recorded, the leak rate at each increment was determined by assuming the leak rate to be proportional. The uncoated sample leak rate was then subtracted from the coated sample leak rate to find the leak rate through the coating. The permeability constant of the APS top coat material was then found using equation 2.4.

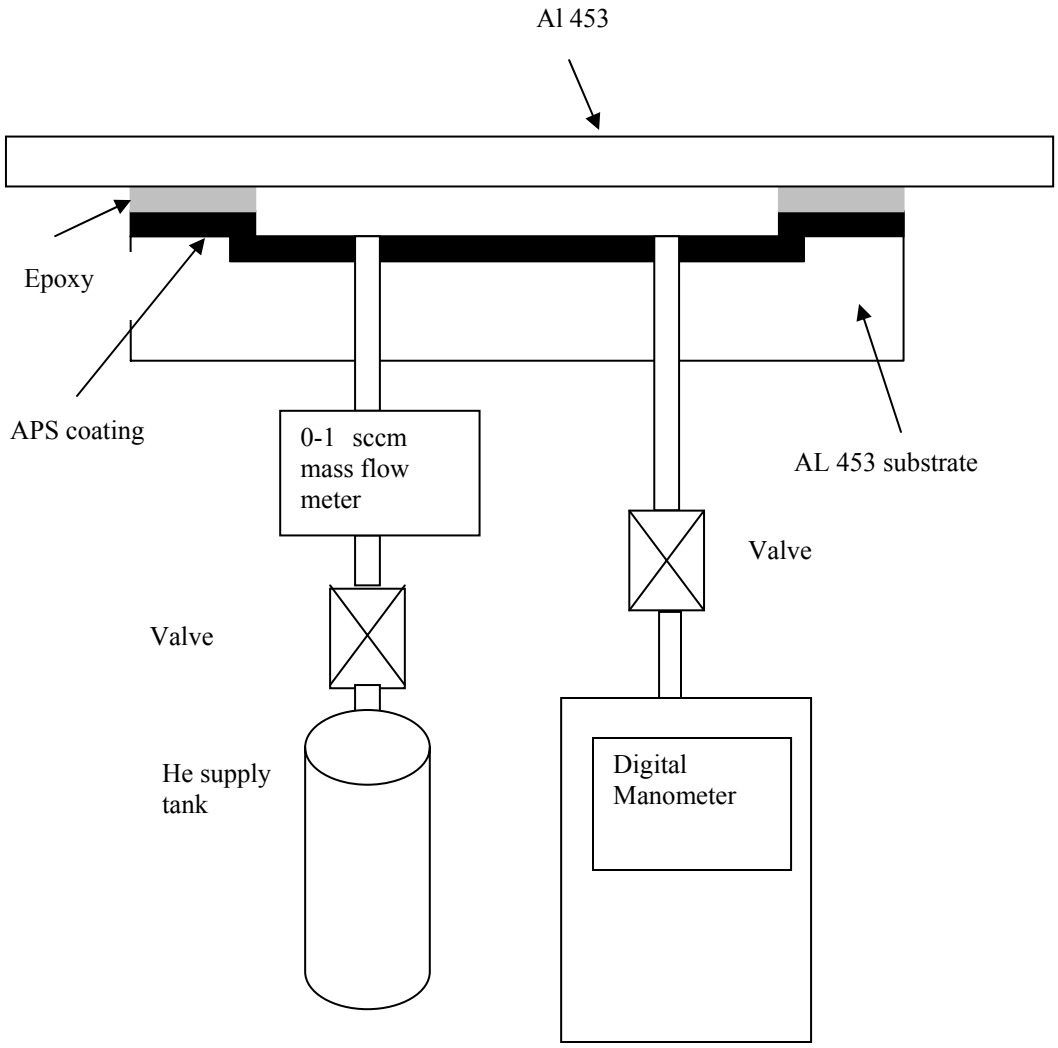

Figure 10 Permeability test apparatus schematic

Permeability Test Results: The compensated room temperature permeability for the Al_2O_3 (80wt%) and a partially stabilized ZrO_2(20wt%) ceramic top coat is presented in Table1. Note that the leak rate of the uncoated sample only accounted for less than 15% of the leak rate of the coated sample so there is confidence that leak path was primarily through the coating. When compared to the leak test samples present in Table 1, the leak through the coating would only account for less than 10% of the total seal leak. However, since the permeability of a porous medium generally increases with increasing temperature, an assumption can be made that in the operational temperature range of 600-800

^{o}C, the leak through the top coat material becomes significant. In order to properly understand this, repeated testing would need to be done at higher temperatures, which is not easily accomplished. Nonetheless, these tests provide a baseline for potential future changes in top coat formulation.

Table 2 Permeability of Al2O3 (80wt%) partially stabilized ZrO2(20wt%) top coat

Temperature T K	viscosity u kg/(m*s)	Diff. Pressure psi	Absolute Pressure p pa	Leak Rate q sccm	kg/s	Permeability K (m^2)
297	2.012E-05	6	1.43E+05	0.122	1.99E-08	2.25E-14
297	2.012E-05	7	1.50E+05	0.151	2.46E-08	2.32E-14
297	2.012E-05	8	1.56E+05	0.167	2.73E-08	2.18E-14
297	2.012E-05	9	1.63E+05	0.188	3.08E-08	2.14E-14
297	2.012E-05	10	1.70E+05	0.184	3.01E-08	1.83E-14

Mean	2.14E-14
Max	2.32E-14
Min	1.83E-14
S.D.	1.87E-15

Electrical Condutivity

A four-wire DC resistance method was used to measure the resistivity of the ceramic coating. The test was conducted with 2 volts exitation for two types of samples at two temperature.

Table 3 Measured area specific resistance (ASR) of the ceramic coating layer at high temperature in air

Temperature (in air)	10vol% YSZ ASR (10^3 ohm-cm^2)	20vol% YSZ ASR (10^3 ohm-cm^2)
800ºC	320.7	9.25
920ºC	189.1	2.61

The resistivity measurement results are shown in Table 3. The resistivity of the ceramic coating was found to increase with decreasing temperautre and volume fraction of YSZ. At 800 ºC , the typical SOFC operation temperature, coating with 10vol% YSZ has an ASR of 320,700 Ohm*cm^2, which is more than adequate for avoiding electrical short-circuiting between the interconnects.

CTE

The coefficient of thermal expansion is defined as the change in dimension per unit change in temperature. It is measured using a dilatometer, an instrument which is capable of recording expansion at a range of temperatures. CTE mismatch is one of the major driving forces of seal failure. Hence, accurate measurements of CTE of the interconnect, cell and seal materials is of critical importance.

Theory: The theory behind the operation of a dilatometer is fairly simple. The instrument consists of a high temperature chamber which houses the sample during testing, position transducers that record sample expansion or contraction.

Experimental Procedure: Measurement of CTE requires accurate determination of sample length, and requires samples at least 0.5” long with polished end

faces. To this end, samples of AL453 stainless steel (Allegheny Ludlum), YSZ, and commercial sealing glass ESL 4460 (ElectroScience) were prepared. The stainless steel and YSZ were cut from discs of material already available. ESL 4460, however, is a sold in the form of viscous paste. Glass powder was made by drying the glass for 1 hour at 125C. The powder was collected and pressed into pellets. These pellets were joined and subsequently cured at 850C to yield glass cylinders. The cylinders were then cut to required dimensions. The prepared samples were sent to Netzsch Instruments Lab (Burlington, MA) for measurement of CTE.

The thermal expansion was measured in accordance with ASTM E288 using a NETZSCH model 402 C pushrod dilatometer. This dilatometer is equipped with a SiC furnace capable of operation between room temperature and 1600 °C. The system is vacuum-tight, allowing measurements to be carried out in pure inert or oxidizing atmospheres, as well as under vacuum. Data acquisition and evaluation, as well as instrument control, are accomplished with a thermal analysis software package. The software includes semi-automatic routines for correction of the sample holder expansion, as well as, computation of the expansion coefficients, onset and peak temperatures, inflection points, rate of expansion, etc. Sample holder expansion was corrected by calibration using a single crystal sapphire standard.

A brief summary of the test parameters is presented in Table 3.

Table 4 CTE Test Parameters

Temperature range	25-1250 °C
Heating rate	5 K/min
Atmosphere	air, 20 ml/min
Sample holder	Alumina
Contact force of push rod	30 cN
Sample length (YSZ)	26.10 mm
Sample length (AL453)	24.01 mm
Sample length (ESL 4460)	16.37 mm

The data obtained is presented graphically below.

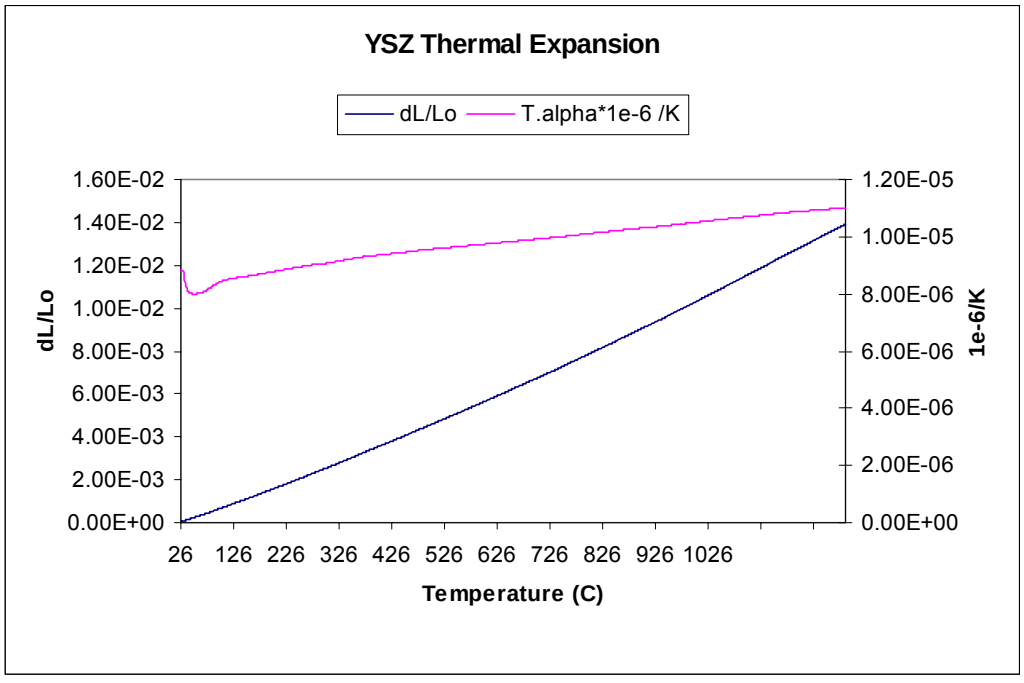

Figure 11 Thermal expansion and technical alpha for YSZ

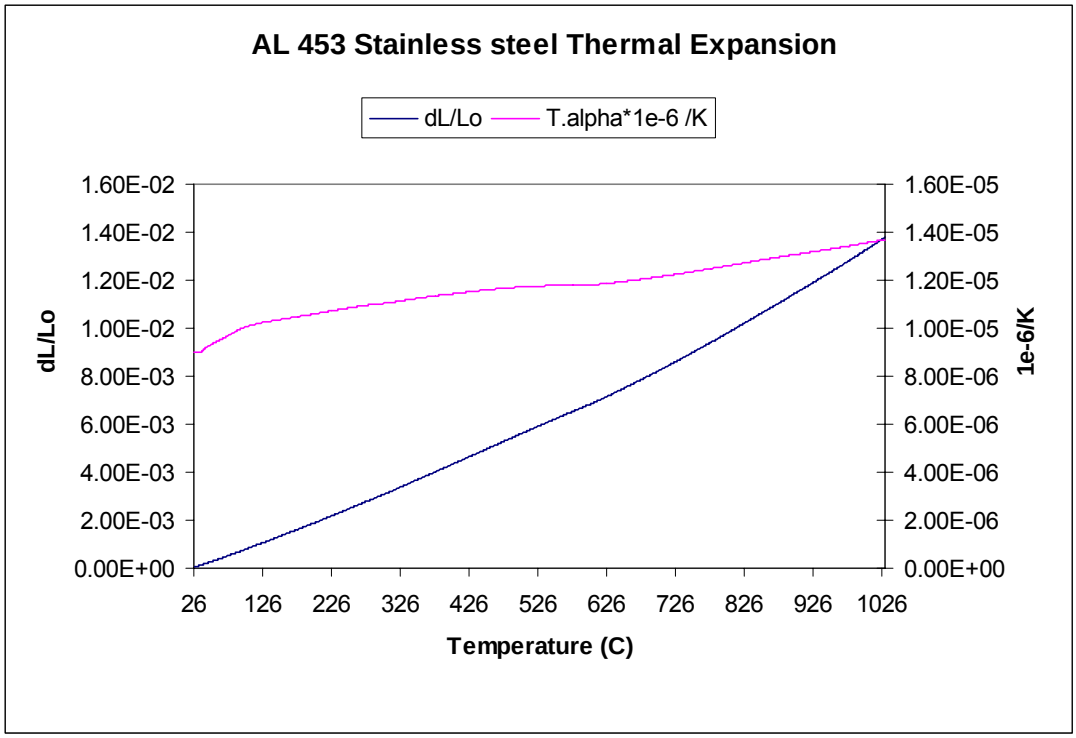

Figure 12 Thermal expansion and technical alpha for AL 453

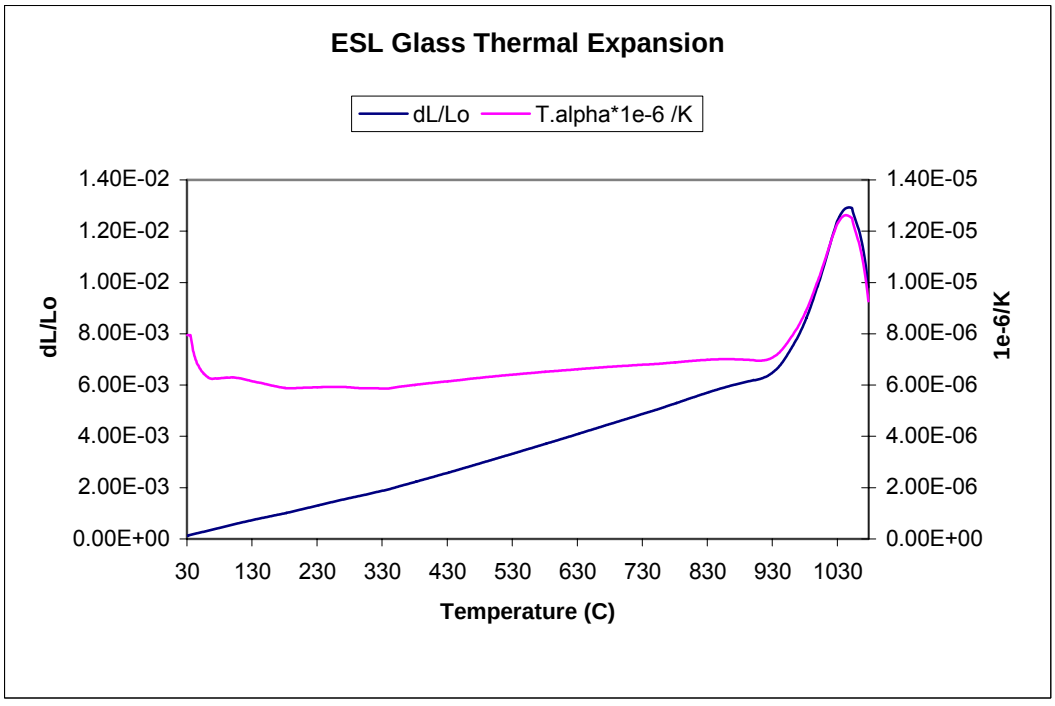

Figure 13 Thermal expansion and technical alpha for ESL 4460

The expansion of the sealing glass shows a sudden change at 950 C, indicating

that this is the glass transition temperature (Tg) for this glass. The glass softening point (T_d) is seen to be 1040°C.

The average CTEs of the stainless steel and the sealing glass the temperature range 100-850°C differ by roughly 0.5E-6/K, which results in considerable thermal mismatch stresses. The ceramic layer makes this CTE transition less abrupt and this mitigates thermal stresses.

3. SEALING PERFORMANCE

As part of the SECA Seal Technology development program, a Solid Oxide Fuel Cell seal test stand has been designed. The test stand will be used to quantify leak rates of existing seals as well as the integrated composite seal being developed by the Connecticut Global Fuel Cell Center. The test stand has been developed to simulate the environment of a typical SOFC and measure the leak rate by methods previously established in other seal tests.

Test Apparatus

The seal test stand required three functional areas of design; 1) the heater area, 2) applied compressive load, and 3) leak flow measurement. The test stand assembly can be seen in Figure 15. The details of the components will be discussed.

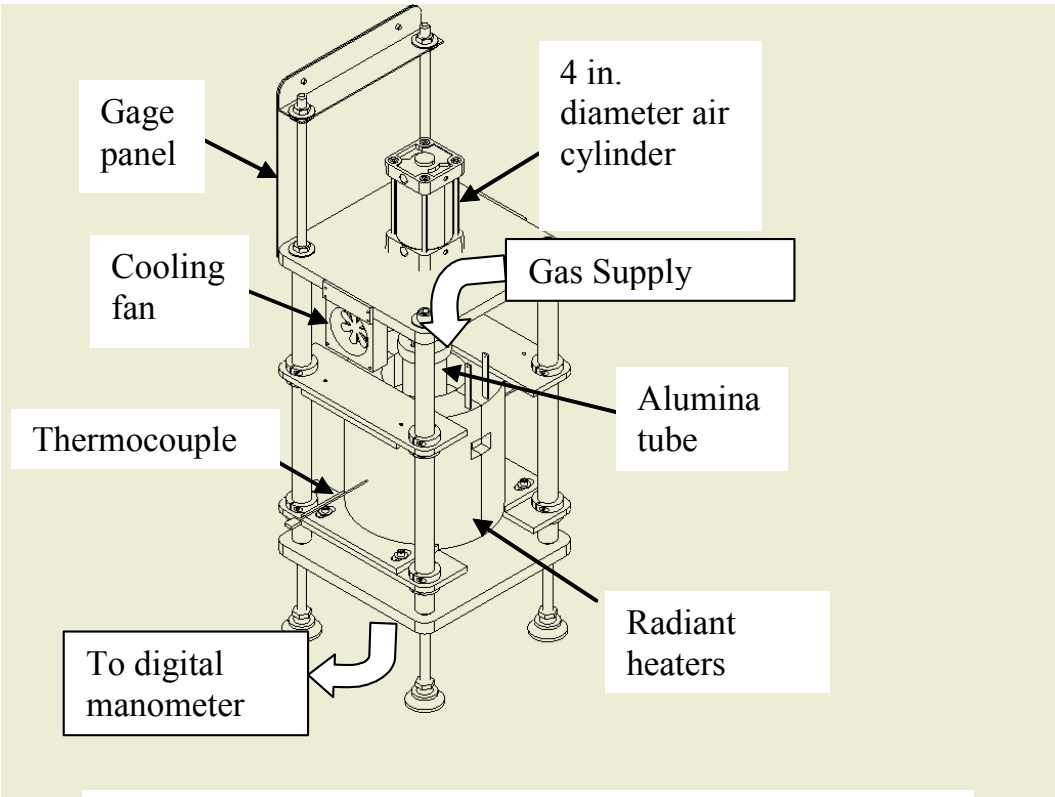

Figure 14 SOFC seal test stand orthographic view

Seal Test Stand Heaters: Heaters are required to bring the samples up to the

operating temperature of a Solid Oxide Fuel Cell. The radiant heaters specified for this test stand are capable of temperatures up to 1115 ^{o}C. The temperature is controlled by thermocouples imbedded into the Inconnel 600 sample holders (Fig. 16) and a PID temperature controller. A redundant temperature measurement is made at the heaters to ensure that the system is not out of control or the heaters are not too hot. The heater control is also capable of ramping and time/temperature control. The heater control is capable of 33 usable steps that may be used for thermal cycle tests.

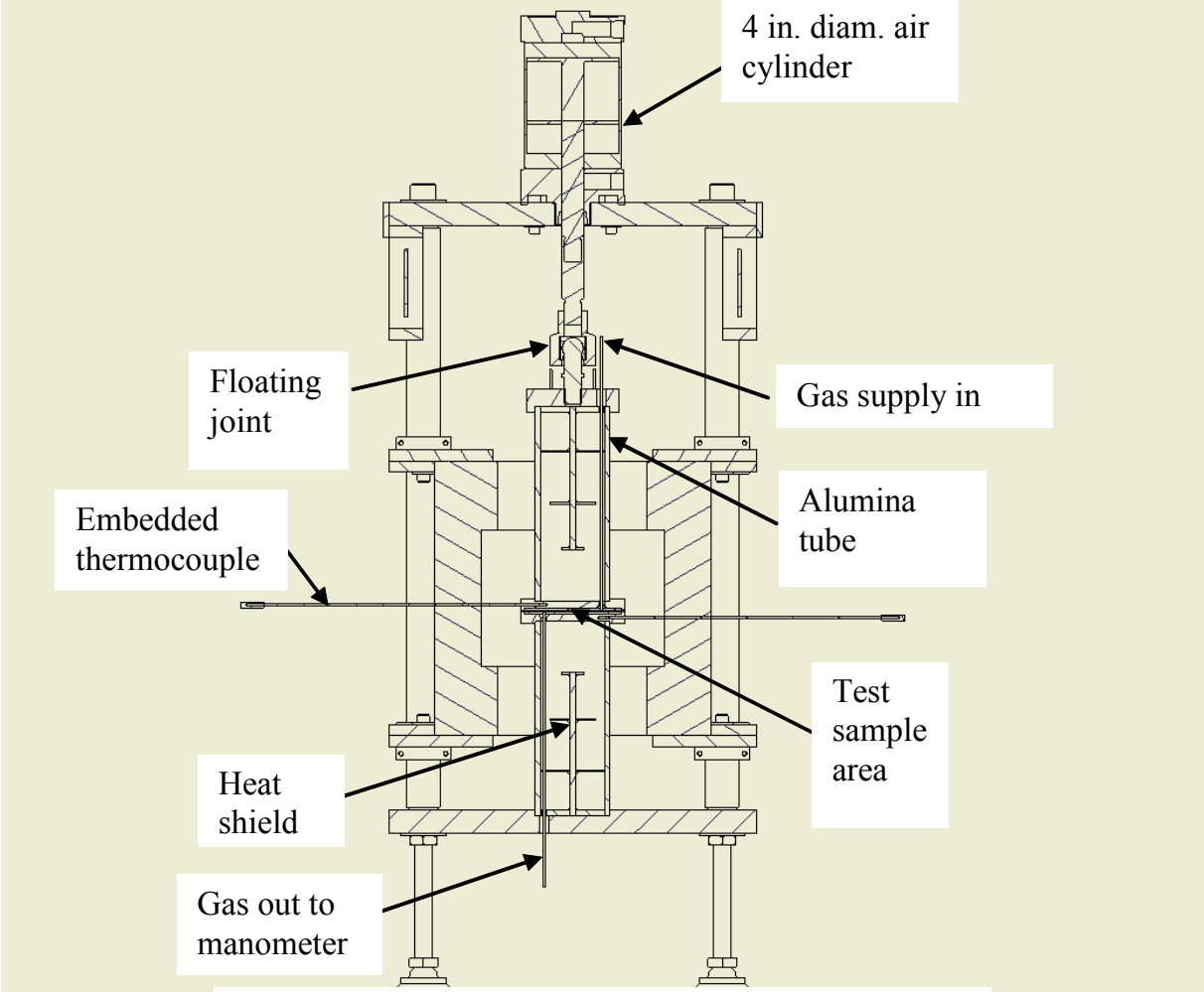

Figure 15 SOFC seal test stand cross-section

Seal Test Stand – Applied Compressive Stress: Compressive load is applied to the seal area via a four-inch (100 mm) air cylinder. The cylinder is capable of forces up to 1880 lbf (8.4 KN). (@ 150 psi = 1.034MPa) but will likely be regulated to pressures less than 60 psi with resulting forces less than 753 lbf (3.35 kN). This pressure range should be sufficient to apply compressive stresses needed for all size seals to be tested. Pressure is to be controlled using a precision regulator with an appropriate precision gage. Note that during testing the mass of the cylinder and connecting parts must be compensated for while determining the final applied compressive stress. The cylinder is connected to a tie rod which has a floating joint on the end. A floating joint is used so load is applied evenly across the seal area. The floating joint is the connected to a mounting plate which is used to hold the Alumina tube that compresses the seal area. Alumina tube is used to insulate the cylinder from the conductive heat from the sample. The system is also insulated from radiant heat by use of heat shields located at the top and bottom of the connecting tubes. To ensure that the air cylinder remains within its proper operating range the tie rod is cooled by cooling fans. Hot air is also carried away by central exhaust vents (not shown).

The sample test area consists of an Inconel 600 sample holder and the sample. The sample is supplied gas, typically helium, via a 1/8 in (3.125 mm). tube welded to the sample. Samples are also coated with seal material. The seal area of the actual design is shown in Figure 17. Note that sample material, size and shape may vary depending on the particular test A schematic is used in Figure 1 to better communicate all materials.

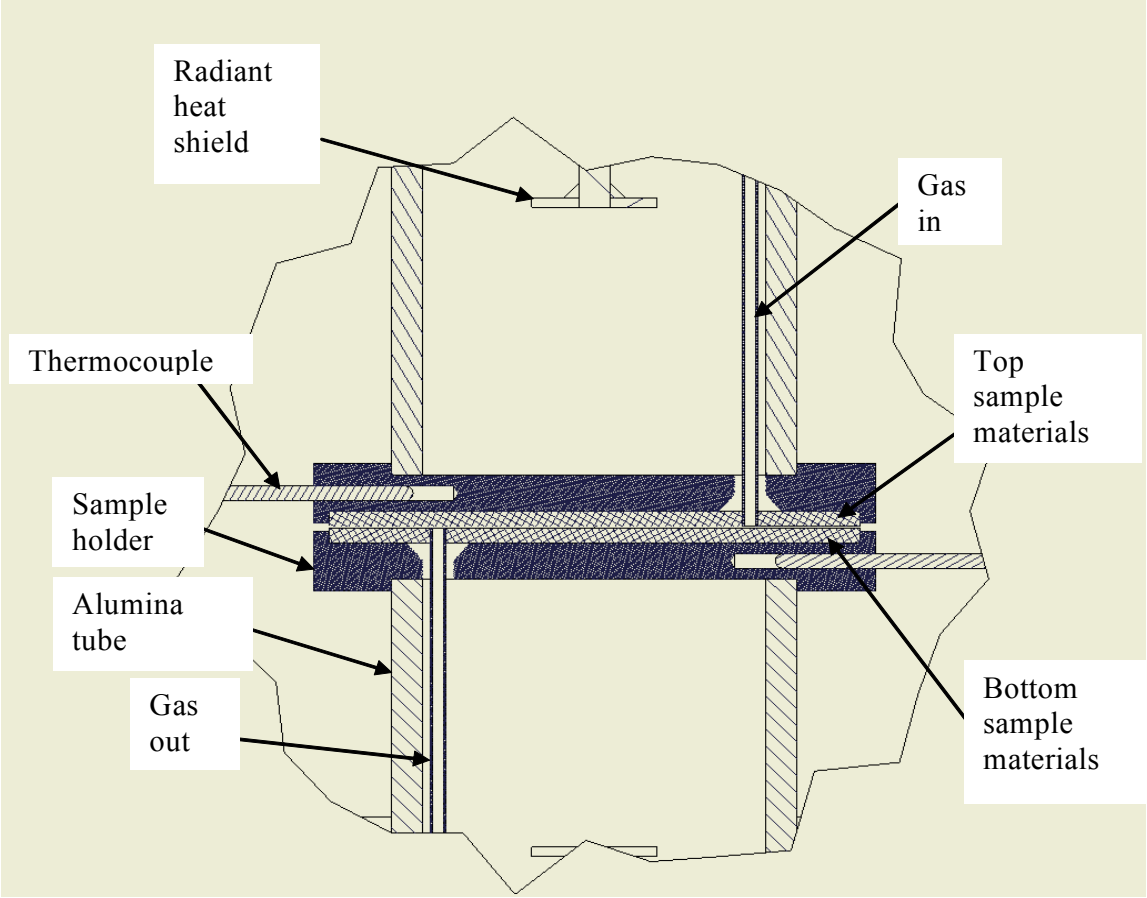

Figure 16 Seal area cross-section

Seals may be of different types; compressive, bonded, and the proposed integrated composite seal. For the compressive seal (e.g. mica seal), the seal will be placed on the metal sample adherent (e.g.) and a compressive force will be applied via the air cylinder. For the bonded seal (e.g. glass) and the integrated composite seal, the seal will be adhered to both sample adherents and the sample will be placed in the holder for testing. An additional compressive force may be applied.

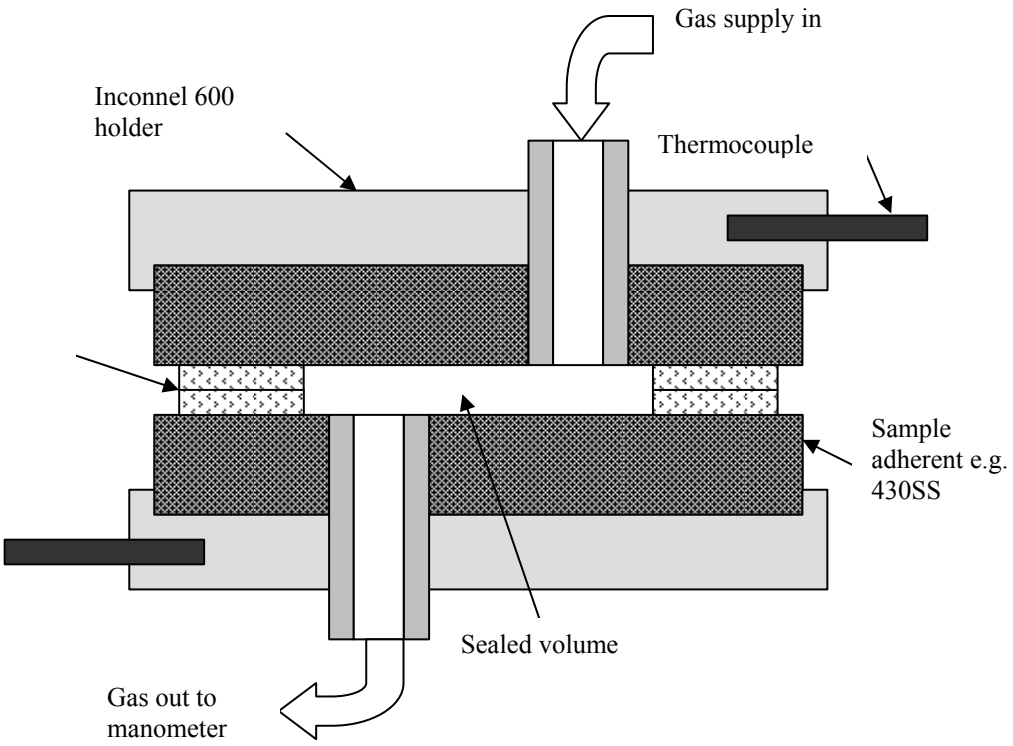

Figure 17 Seal Area Schematic

Seal Test Stand Leak Rate Measurement: Leak rate was determined using two different methods depending; 1) direct flow rate measurement using mass/volumetric flow meters for high flow (0.1-100 sccm) and 2) leak down rate for both high flow and low flow (<0.1 sccm). The current design allows either of the tests to be run by opening and closing different valves (Fig. 19).

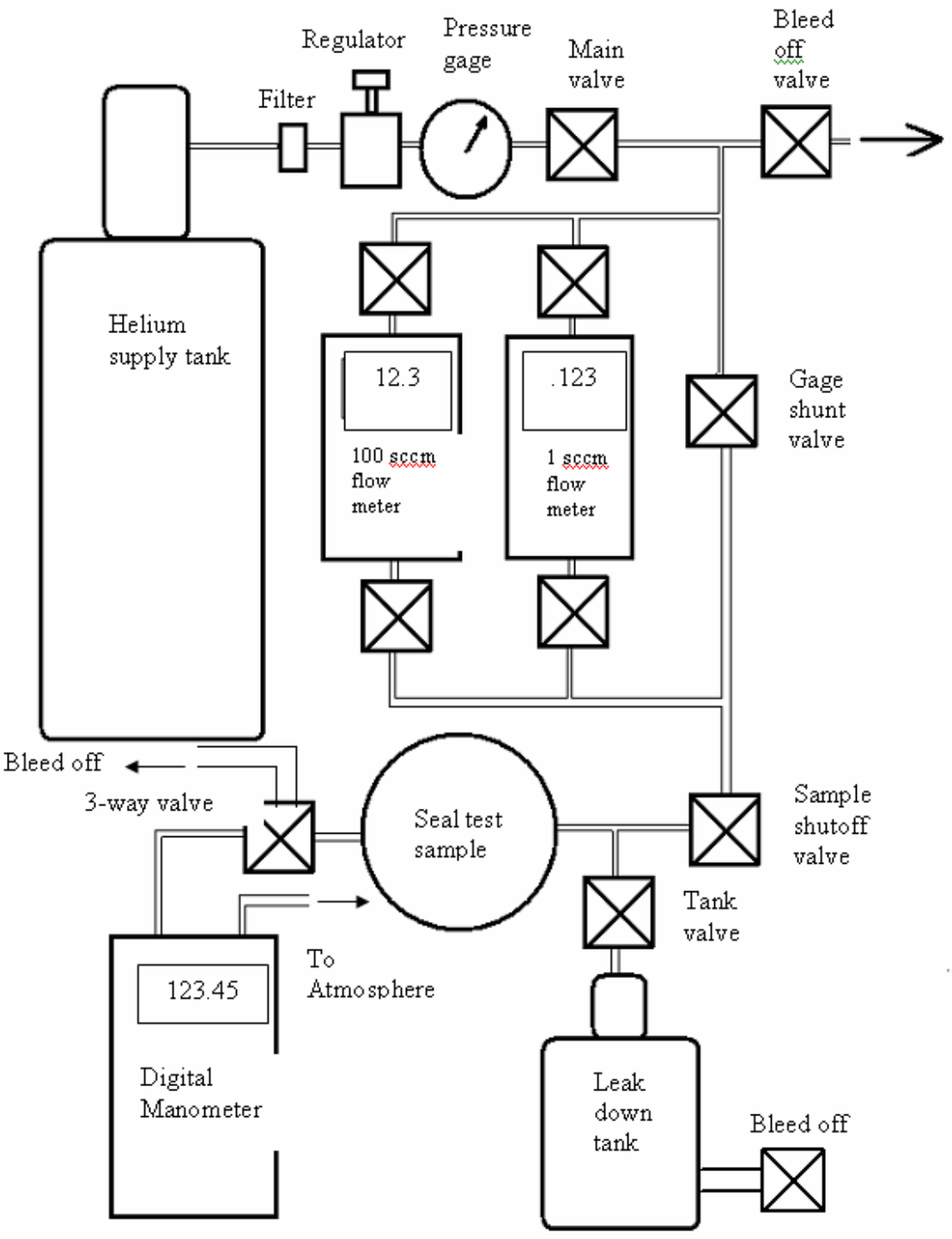

Figure 18. Leak rate testing schematic.

Direct flow measurement is enabled by closing the gage shunt valve and opening the valves to the appropriate mass/volumetric flow meter. The two mass flow meters used primarily for the leak testing are the Alicat Scientific M-100SCCM-

D(He)) with 0-100 sccm measurement range and the M-1SCCM-D(He) with 1 sccm full scale. The main valve is opened and the sample shutoff valve is then opened. Readings may then be made either from the readout on the meter or by an analog output to a data acquisition system. The meter can either read the mass or the volumetric flow. The mass/flow meter is capable of measuring flow rates of different gases but has been calibrated using helium.

Leak down testing is accomplished by opening the main valve, then opening the tank valve, manometer valve, and sample valve. Once the system has reached equilibrium at the set pressure, the main valve is closed. Additional fine pressure adjustment may be made using the bleed off valve. At this time the leak down test is started and the sample pressure decay is measured. The time/pressure information is saved in the digital manometer (Omega HHP-2082) using an internal datalogger. Different tank sizes and tank pressures may be used depending on the expected leak rates.

Leak Rate Test Methods Theory: As mentioned, the apparatus design is capable of providing seal leak rate by two methods; 1) direct flow rate measurement using mass/volume flow meters and 2) leak down rate. The direct flow rate measurement method allows for the leak test to be run continuously for a long period of time and would be most practical during thermocycling. However, when ultra-low rate measurements are necessary the method will not provide the accuracy of the leak down test. The leak down test provides an accurate method to determine the leak rate through the seal but is not capable of providing continuous leak rate data as it is necessary to pressurize and depressurize for each measurement.

Method 1: Direct Flow Rate Measurement: The general method for the direct flow rate measurement was provided courtesy Fuel Cell Energy and is similar to practices suggested by the manufacturers of mass flow meters. The seal is compressed between the test substrates using the air cylinder. The pressure regulated test gas is supplied in-line with the mass/flow meter. The leak rate is

then measured continuously as the gas leaks through the seal.

The exact method for measurement using the mass/volumetric flow meter is proprietary to the manufacturer, however, the general theory is supplied by Alicat Scientific. The Internally Compensated Laminar (ICL) meter measures flow by using differential pressure techniques and the use of Poisuille Equation:

$$Q = K(P_1 - P_S)/\eta \quad (3.1)$$

Where :

Q = Volumetric flow rate

P_2 = Inlet static pressure

P_2 = Outlet static pressure

η = Absolute viscosity of the fluid

and K is a constant described by;

$$K = r^4 \pi / 8L \quad (3.2)$$

Where:

r = Hydraulic radius of the restriction

L=Length of the restriction

The ICL device uses a discrete temperature measurement and a microprocessor to determine th absolute viscosity of the gas. Also, the pressure drop is created using a restriction know as a Laminar Flow Element (LFE). In order to relate the volumetric flow rate, the density and temperature must be related to standard conditions (STP). Then through use of the ideal gas laws the mass flow may be written as;

$$M = Q(T_s/T_a)(P_a/P_s) \quad (3.3)$$

Where:

M = Mass flow rate

Q = Volumetric flow rate

T_s = Absolute temperature at flow condition

T_a = Absolute temperature at Standard condition

P_a = Flow absolute pressure

P_s = Absolute pressure at Standard condition

Method 2: Leak Down Rate Measurement: For the leak down test, a gas reservoir is pressurized to a set value from a main gas supply. The valve to the main gas supply is then shut and the pressure decay is then measured. By monitoring the pressure decay from the know volume, gas reservoir, the flow rate may then be determined from the pressure decay versus time data using ideal gas laws assuming that the flow is laminar:

$$L = \frac{\Delta n}{\Delta t} = \frac{n_f - n_i}{t_i - t_f} = \frac{(p_f - p_i)V}{RT(t_f - t_i)} \tag{3.4}$$

Where:

L = Leak rate

n_i, n_f = Initial and final molar quantities of gas

t_i, t_f = Intial and final test times

p_i, p_f = Initial and final gas pressures

V = Gas reservoir volume

R = Gas constant

The reported leak rate in standard cubic centimeters per minute at standard temperature and pressure is then the calculated leak rate normalized with respect to the outer seal length.

Alternatively, the reservoir may be evacuated and the leak rate is measured in a similar manner as air leaks through the seal and into the evacuated space. Both the vacuum method and the pressure method have been used in determining seal leak rates in SOFCs. Since helium gas (He) is more similar to hydrogen gas

(H_2) than air, in terms of molecular size, results using pressurized helium should be more representative of leak rates in an actual SOFC.

In order to size the measurement equipment for each seal, the following equation may be developed from equation 3.5:

$$p_f = p_i \exp^{-t/\tau} \tag{3.5}$$

Where:

p_i, p_f = Initial and final gas pressures (Pa)

t = Time (s)

τ = Time constant = V/cRT where

V = Volume of the reservoir (m^3)

R = Gas constan t(J/mol • K)

C is a constant for a given seal arrangement for a particular gas and is a function of gas viscosity and density, seal permeability, seal area, and distance across the seal. C is given in mol/s • Pa and can be related to Darcy's equation for flow through a porous media:

$$Q = -\frac{\kappa A}{\mu}\left(\frac{dp}{dx}\right) \tag{3.6}$$

Where:

Q = Volumetric flow (cm^3/s)

κ = Permeability (Darcys,(cm^2cP/s • atm)

A = Exposed area of seal (cm^2)

μ = viscosity (cP)

dp = Differential pressure across x (atm)

dx = Differential of length across seal (cm)

Equation 2.5 can then be used not only to estimate the gas reservoir volume, test time, sampling rate, seal size and differential pressure across the seal but also to help determine the test method to be used. For example, a high flow (poor seal) test would be better tested using method 1 because the flow rate may be too high for the leak down test to accurately measure the flow rate since dp/dt will be too high and the sampling rate of the manometer will not be able to capture an

accurate value. Alternatively, for leak rates below 0.1 sccm the mass/volumetric flow meter will not sufficiently accurate to measure the flow. Note that the lowest flow meter is 0-1 sccm with 1% of full scale accuracy.

Test Method Comparison

In the development of the new composite seal, it is important to first verify that the measurement techniques are valid and qualify the results with those previously published. The two methods of leak testing were first compared, direct and indirect. Also, the relationship of gas pressure to leak rate was tested. In this section the leak down method which is commonly used for leak measurement is compared to the direct flow rate measurement using a mass flow meter.

Leak Method Experimental Procedure: The equipment was first setup as shown in **Error! Reference source not found..** The system including all lines, valves, specimen and tank is then flushed with the test gas. In this case, helium is the main test gas. All testing for this system was done at room temperature. The test specimen in this case was ferritic stainless steel AL 453 supplied by Allegheny Technologies, Inc. The top sample had been coated with a 20% Zirconium Oxide/ 80% Alumina atmospheric plasma spray (APS). The bottom sample was AL453 in “as rolled” condition. The top sample was adhered to the bottom sample using industrial adhesive. The inner diameter of the seal was 1.5 in. (38.1 mm) and the outer diameter was 2.0 in. (50.8 mm). The downstream valve closest to the mass flow meter was closed and the meter was zeroed. All down stream valves were closed to test all connections. Also, all hose connections were tested by removing them from the specimen and plugging the hose. The downstream valve closest to the meter was then opened and zero was verified for each subsequent valve with the exception of the tank valve.

The mass flow meter (Alicat Scientific M-1SCCM-D(He)) was used to directly record the leak rate of the specimen. The direct flow rate measurement was then

performed at various pressures adjusted by the precision regulator and verified by the digital manometer located near the test specimen. Both the mass flow meter and the digital manometer were zeroed at room temperature and ambient pressure conditions prior to testing. Readings at five different pressures were recorded going from approximately 1 psi to 5 psi. This was then repeated going from 5 psi to 1 psi to check for any hysteresis. It is important to note that when recording these readings with very low leak rates, one had to wait approximately 20-30 minutes in between each reading for the system to fully stabilize in order to get accurate results. The results were then interpolated for readings to be expressed in increments of 1 psi. A linear extrapolation was assumed here but was later be tested.

The indirect flow rate measurement was made in a manner similar to the direct flow rate measurement except that the leak down tank was used to supply helium test gas to the specimen. The system was pressurized to 5 psi and all upstream valves were closed. The manometer (Omega HHP-2082) was set to log pressure every 1 minute. The flow rate was determined using equation 2.4. For most of the test results, the flow rate reported is in standard cubic centimeters per minute per centimeter of outer diameter of seal (sccm/cm).

The leak rate was also tested as a function of differential gas pressure from 0-3 psi. (0~20.68 kPa) This was performed so that estimate of leak rates at pressures other than those tested can be made. Typically leak rates for SOFC sealing materials have been performed between 14 kPa (2 psi) and 50 kPa (7.25 psi), however, tests have also been performed under vacuum conditions [c,1] . Most SOFCs are designed to operate with differential gas pressures less than 7 kPa (1 psi). All of the measurements done for this test were performed using the mass flow meter in a manner similar to that already present in this section.

Leak Test Method Comparison Results and Discussion: The result of the

comparison of leak test methods is shown in Figure 2.6. For the indirect method, the leak rate at a particular pressure was found by using the pressure gradient from the 10 preceding and 10 following samples. There is very little difference noted in the test results. The maximum deviation from the direct to the indirect method is approximately 10%. Although the results are not shown here, it should be noted that similar tests were performed with the seal at the operating temperature of the SOFC (600-800^{o}C). There is also very little hysteresis within the direct flow rate measurement and the indirect method with all direct data being within 10%.

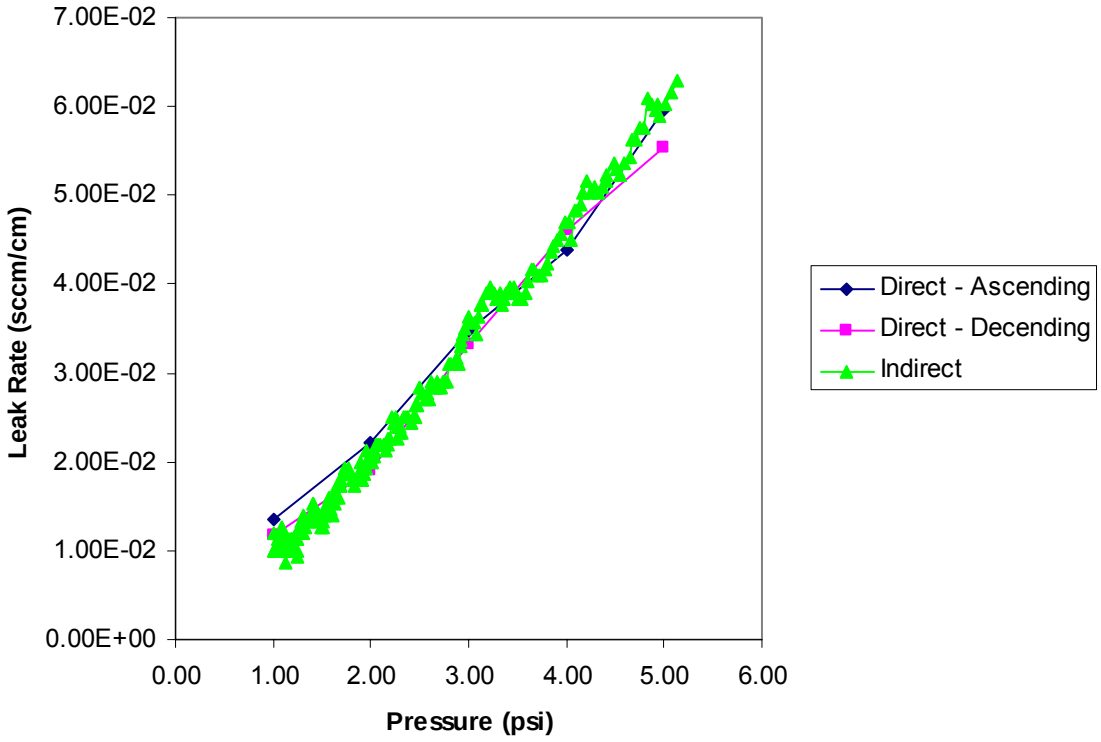

Figure 19 Comparison of leak rate measurement methods

The direct method is an inherently a better method when continuous monitoring of the flow rate is necessary thus making it more desirable for long term thermal cycle testing. The indirect leak down test, however, is appropriate when leak rates are not within the range of the mass flow meter or if leak rates need to be determined at many different pressures.

The leak rate as a function of differential pressure is shown in Figure 20. The coefficient of correlation is .9983 suggesting that considering the leak rate to be linear is a reasonable assumption. Also, gas leaks similar to this are likely to be primarily in the laminar flow region. Therefore, in future testing it is only necessary to report the leak rate at one standardized pressure and all other leak predictions at different pressure may be made depending on the application.

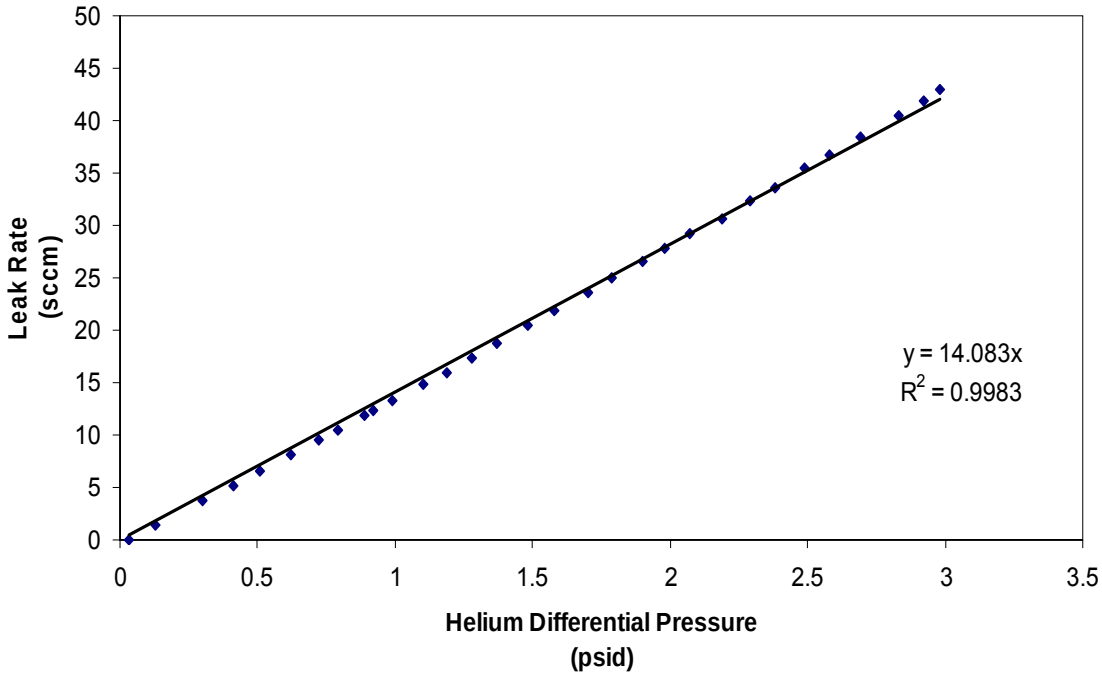

Figure 20 Leak rate linearity

Initial Leak Performance

Various materials have previously been utilized for sealing SOFCs. In order to quantify how well the composite seal performs, it was necessary to compare the initial sealing results of other materials with composite seal design being studied by the Connecticut Global Fuel Cell Center (CGFCC). Several configurations were considered for this comparison; mica, glass to metal seal, glass/ceramic composite and metal/ceramic composite.

Initial Seal Performance Evaluation Experimental Procedure: Mica has been studied extensively as a potential sealing material, therefore mica was used as a

control seal sample for testing seals. The test substrate in this case was a ferritic stainless steel, AL 453 supplied by Allegheny Technologies, Inc. The top and bottom substrates were AL453 in “as rolled” condition. The inner diameter of the seal was 1.5 in. (38.1 mm) and the outer diameter was 2.0 in. (50.8 mm). The seal material tested was 100 micron thick muscovite paper purchased from McMaster-Carr. The seal was cut roughly to size and a 1/8 in. (3.2 mm) hole was cut into the center. The seal and the substrates were then placed into the seal test station and the seal was compressed between the two substrates at 5 psi (34.47 kPa) cylinder pressure.

All the standard leak checks were performed and the system was flushed with helium. The specimen was then heated to the operating temperature of 800 ^{o}C. The temperature was measured using a K-type thermocouple input to the Watlow SD3R-HCUA-AARG temperature controller. At this point compressive stress and gas pressure were altered and data was recorded. The compressive stress was adjusted using a precision regulator in-line with the four inch (100 mm) dia. air cylinder. Mass compensation of all the components above the specimen was made and additionally compensation of the gas pressure inside the test specimen was made. Data were recorded at seal compressive stress of 100, 300, 500 and 700 psi (.689, 2.069, 3.448 and 4.827 MPa). Although measurement at different gas pressures were made only those readings at 2 psid (14 kPa) are presented here.

All other samples were tested in a similar manner.
Table 5 Seal test materials matrix shows the test matrix of materials and substrates. The glass samples had to go through cure cycles prior to testing the cycle for each particular glass as shown in Figure 21-Figure 24. For those glasses that in tape form, the glass powder was mixed with a binder (Cerabond 552-T, Aremco Product, Inc) and cured per a recommended schedule.

Table 5 Seal test materials matrix (All APS coatings are 20% YSZ and 80% Al2O3)

Sample #	Top Substrate	Bottom Substrate	Seal Materials	Seal Diameters	Cure Schedule
1	Ferritic SS – AL453	Ferritic SS – AL453	.1 mm Muscovite paper	50.8 mm OD 38.1 mm ID	N/A
2	Inconnel 600	Al453 w/ APS coat	UMR #27 glass powder	50.8 mm OD 38.1 mm ID	Fig. 2.9a
3	Al453 w/ APS coat	Al453	ESL 4460 glass (100 micron tape)	25.4 mm OD	Fig. 2.9b
4	Al453 w/ APS coat	Al453 w/ APS coat	ESL 4460 glass (100 micron tape)	50.8 mm OD 38.1 mm ID	Fig. 2.9b
5	Al453 w/ APS coat	Al453 w/ APS coat	Singh glass powder	50.8 mm OD 38.1 mm ID	Fig. 2.9c
6	Al453 w/ APS coat	Al453 w/ APS coat	.1 mm single crystal (SC) muscovite	50.8 mm OD 38.1 mm ID	Held at 800^{o}C & 3.45 MPa Compress.
7	Al453 w/ APS coat	Al453 w/ APS coat	Gold o-ring Scientific Instrument P/N GG140025	37.2 mm OD 35.6 mm ID measured after testing	Compress stress = 3.1 MPa
8	Al453 w/ APS coat	Al453 w/ APS coat	UMR #27 glass powder	50.8 mm OD 38.1 mm ID	Fig. 2.9a
9	Al453 w/ APS coat	Al453 w/ APS coat	SNL glass	50.8 mm OD 38.1 mm ID	Fig. 2.9d

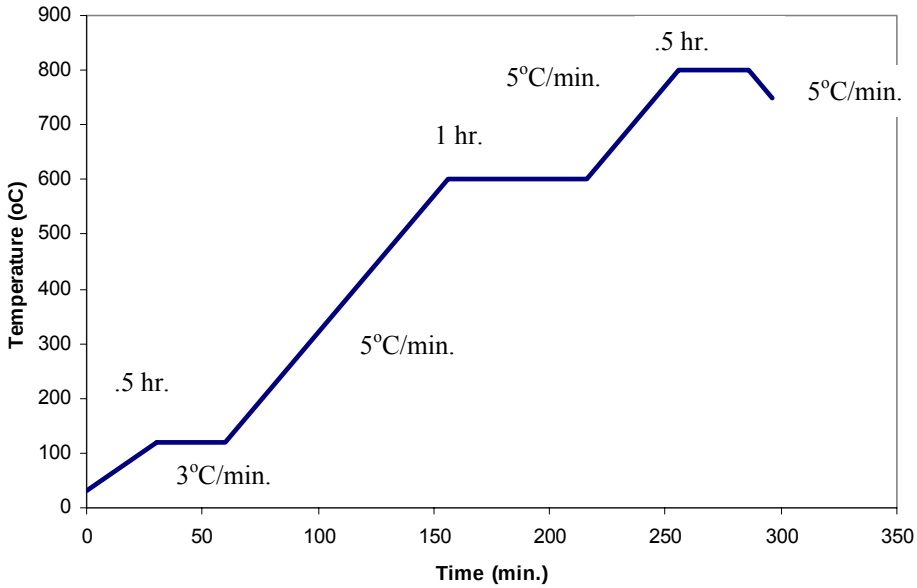

Figure 21 Cure schedule for UMR#27 glass

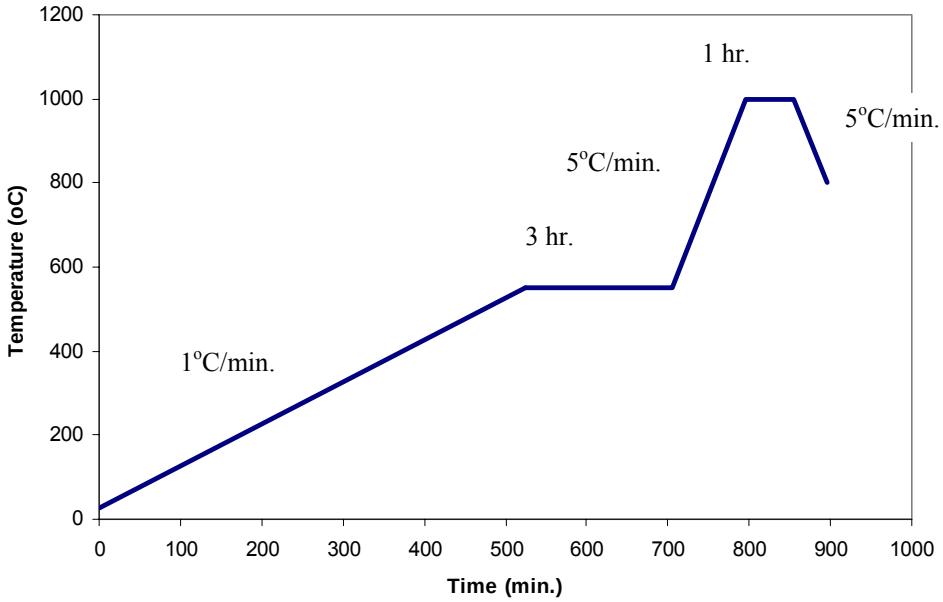

Figure 22 Cure schedule for ESL 4460 glass (100 micron tape)

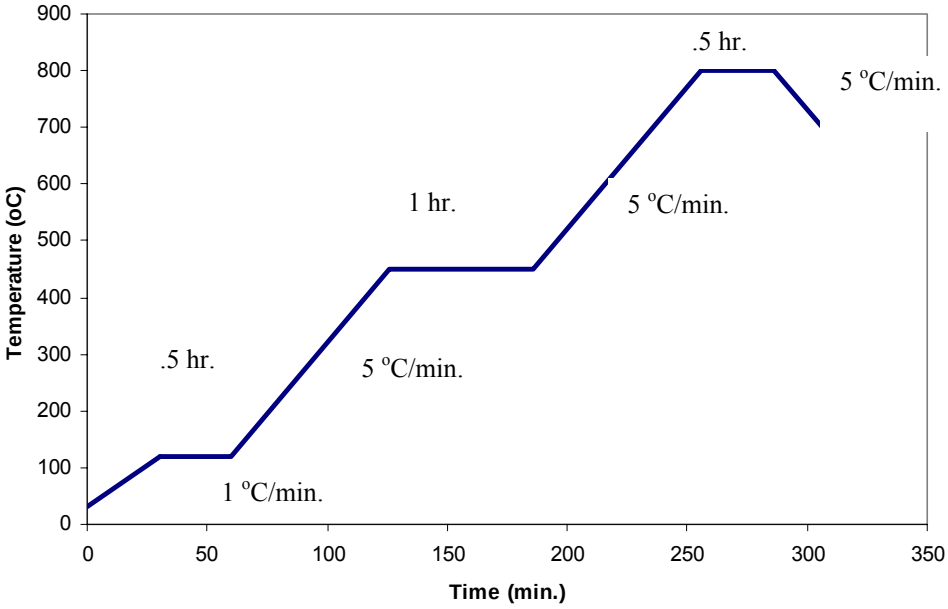

Figure 23 Cure schedule for Singh glass

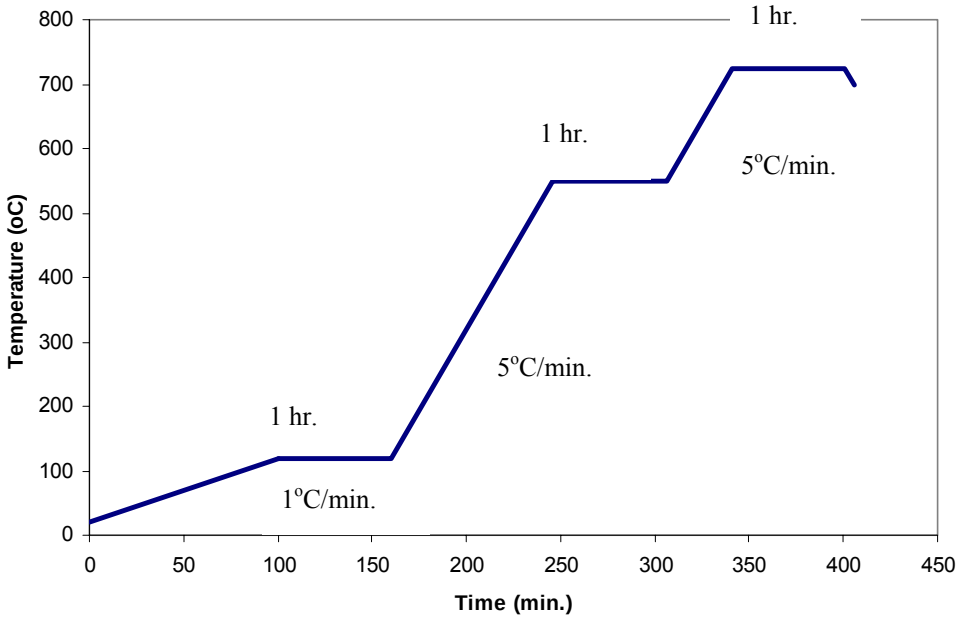

Figure 24 Cure schedule for SNL glass

Initial Seal Performance Evaluation Results and Discussion: The .1mm muscovite paper did provide sealing characteristics similar to those shown by Chou et. al.[4,5], however, a lower overall leak rate was found (Figure 25).Chou et al. reported that defects in the metal and alumina tube are major leak path for compressive seals such as these mica seals. The substrate material used by the Connecticut Global Fuel Cell Center (CGFCC) team was a ferritic stainless steel, AL453 in the "as rolled" condition. This is likely a smoother surface than the Inconnel tube hand ground with #400 grit paper and alumina tube. By reviewing similar data presented by J.W. Fergus [6] as shown in Figure 25, it is apparent that the results are of the same order of magnitude as similar type seals and there is no dramatic difference. As this is not the focus of study, there was no further investigation into reasons for slight inconsistencies. This control experiment did, however, suggest that the leak test results for the CGFCC system are valid.

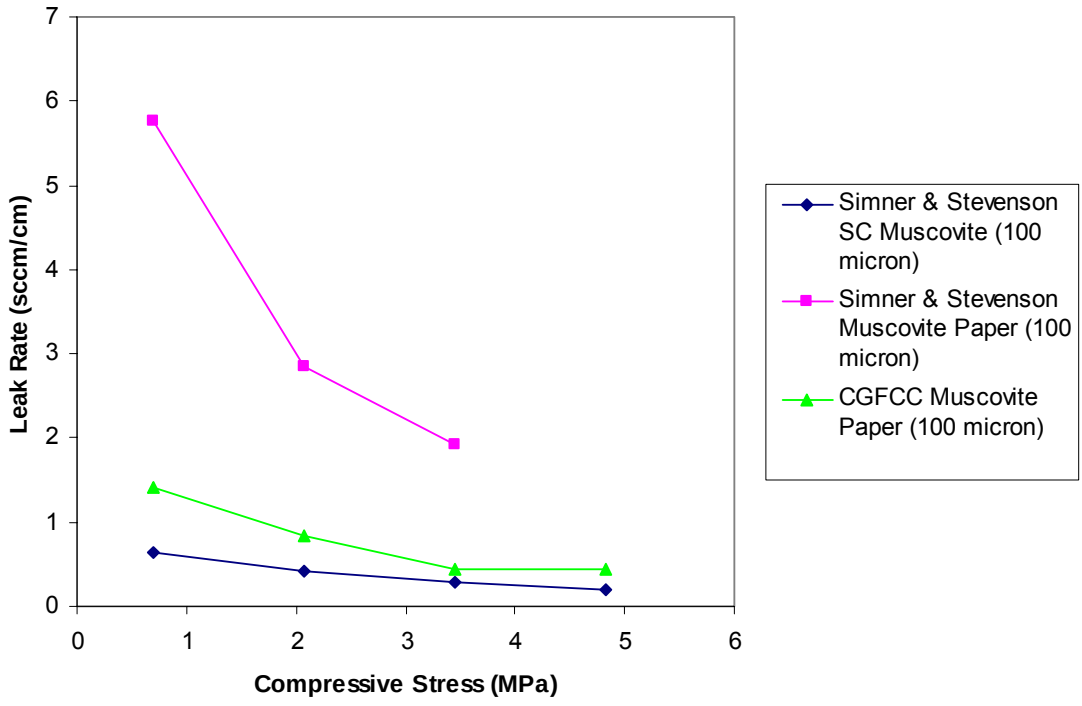

Figure 25 Comparison of muscovite seals test results

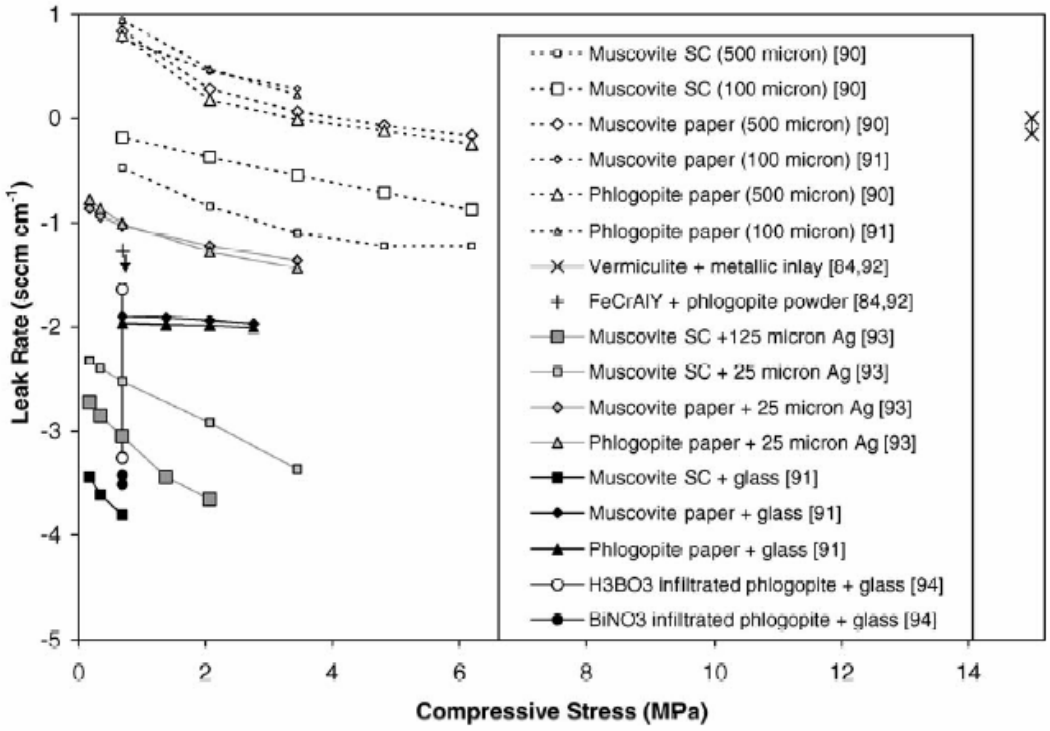

Figure 26 Leak rates for mica based seals

The initial seal performance for the samples shown in the leak test matrix is shown in Table 5. All flow rate rates reported are standardized with respect to the outer diameter of the seal and a helium differential gas pressure of 2 psi (13.8 kPa). The best seal performance was found to be sample 5 (Singh glass with APS coated substrate) and sample 9 (SNL glass with APS coated substrate). The constraint with these systems is that these glasses are not designed to be utilized at sustained temperatures in the 800^{o}C range necessary for some SOFC applications due to crystallization issues. The gold o-ring to APS coated metal also demonstrated remarkable seal performance of approximately 0.137-.125 sccm/cm at force ranges of 279-1117N which is similar to the performance found by Chou et al. for mica seals with gold interlayers (**Figure 26**) [6,7].

Table 6 Initial seal leak performance results (All APS coatings are 20% YSZ and 80% Al2O3)

Sample #	Top Substrate	Bottom Substrate	Seal Materials	Leak Rate (sccm/cm)	Temp. (^{o}C)
1	Ferritic SS – AL453	Ferritic SS – AL453	.1 mm Muscovite paper	1.42 @ 690 kPa 0.83 @ 2.06 MPa 0.44 @ 3.44 MPa 0.44 @ 4.83 MPa	800
2	Inconnel 600	Al453 w/ APS coat	UMR #27 glass powder	0.275	800
3	Al453 w/ APS coat	Al453	ESL 4460 glass (100 micron tape)	0.225	800
4	Al453 w/ APS coat	Al453 w/ APS coat	ESL 4460 glass (100 micron tape)	4.41	800
5	Al453 w/ APS coat	Al453 w/ APS coat	Singh glass powder	0.0222	650
6	Al453 w/ APS coat	Al453 w/ APS coat	.1 mm single crystal (SC) muscovite	3.44 @ 690 kPa 3.20 @ 2.06 kPa 2.87 @ 3.44 MPa	800
7	Al453 w/ APS coat	Al453 w/ APS coat	Gold o-ring Scientific Instrument P/N GG140025	0.137 @ 279N 0.125 @ 559N 0.125 @ 1117N	800
8	Al453 w/ APS coat	Al453 w/ APS coat	UMR #27 glass powder	No seal, glass crystallization	800
9	Al453 w/ APS coat	Al453 w/ APS coat	SNL glass	0.0601	700

The gold o-ring and the mica seals both show dependence on compressive force of the seal quality. The glass seal was also tested to see if there is any correlation between compressive force and the leak rate of the seal. Figure 27 shows that Singh glass tested at different amounts of compression show no obvious correlation of seal compression to the leak rate as expected.

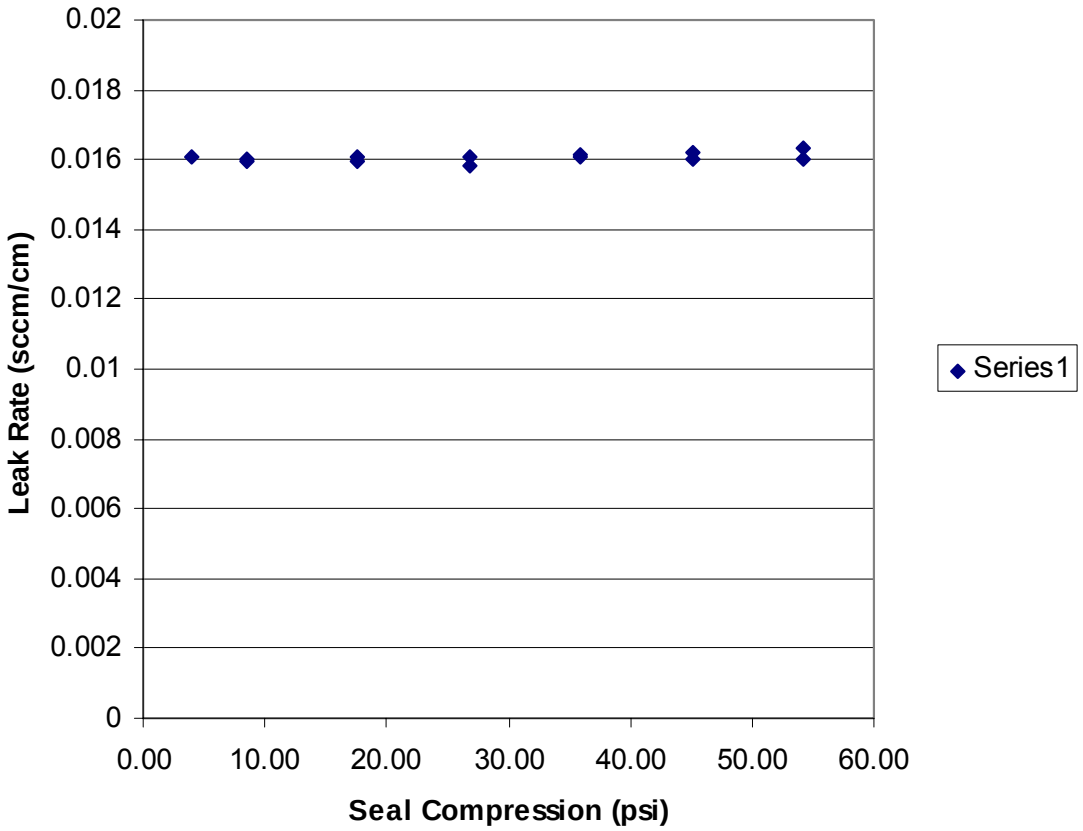

Figure 27 Effect of seal compression on glass / APS composite seals

Thermal Cycling Performance

A SOFC stack may be subjected to many thermal cycles throughout the life of the system. It is therefore important that the SOFC seal can withstand rigorous thermal cycling. Rigid glass seals are particularly subject to failing during thermal cycling. The CTE difference between cell components creates mismatch stresses that eventually lead to failure of the seal. One advantage of using the 20% Zirconium Oxide and 80% Alumina APS coating is to help mitigate mismatch stresses. Glass that is "self-healing" can be used to reseal a SOFC seal after cracking has occurred by heating the seal back up above the glass transition temperature of the glass. Several glasses were studied here as candidates for "self-healing" glass materials to be used for SOFC seals. Another option to solving the CTE mismatch issues is to use a compliant material instead of the glass as the filler in the composite seal. A gold o-ring was used as the trial compliant material. The melting point of gold is 1064 ^{o}C which higher than the operating point of a typical SOFC. Also, gold is known to be relatively compatible

with the materials in the stack and is relatively soft making the sealing characteristics good. However, the cost of gold may make it not feasible as good seal material. A thin gauge oxidation resistance alloy is being investigated as a cheaper replacement of gold.

Thermal Cycling Test Procedure: **The equipment was setup as shown earlier in section 3. Datalogging was accomplished using both National Instruments and Physical Acoustics data acquisition systems. All data recorded for the Singh glass (sample 5**
Table 5) thermal cycling was accomplished using National Instruments Labview 7.0 in conjunction with National Instruments PXI-1011 data acquisition chassis outfitted with an 8-channel thermocouple amplifier module, SCXI-1112 and a multifunction I/O card (PXI-6052E) with terminal block (NITB-2705). The remainder of the thermal cycle testing was accomplished using the Physical Acoustic Corporation (PAC 60120-2014 rev. 4) PCI board as the main data acquisition system which includes a six channel parametric input block. The National Instruments I/O card was used to input temperature from a K type thermocouple and output a 0-10V signal to the PAC system. The gas pressure was monitored using a Druck PTX 1240 0-15 psi pressure transducers with a 4-20 mA output which was coupled with a 250 ohm resistor to give a 1-5V output. Leak rate measurements were made using Alicat Scientific M-1SCCM-D(He) and Alicat Scientific M-100SCCM-D(He) mass flow meters which output 0-5V signals.

Samples were subjected to a variety of dwell temperatures and heating rates. The material subjected to thermal cycling were samples 2,5,7 and 9 from
Table 5. Sample 2 (UMR#27 glass) was only subjected to one thermal cycle for reasons to be discussed. Sample 5 (Singh glass) was subjected a total of 63 thermal cycles. Sample 7 (gold o-ring) and Sample 9 (SNL glass) were tested for a total of 10 cycles between 100 to 800^{o}C and 100 to 700^{o}C respectively.

Thermal Cycling Results and Discussion: Seal sample #2 (AL453/UMR#27 glass/APS ceramic coating) failed after one thermal cycle (*Figure 28*) and was

not able to be resealed by heating back to the glass transition temperature. There were two factors which contributed to the failure of the seal. By observing the sample shown in Figure 29, the determination was made that the seal slipped off center but also there is a surface texture and color change indicating that there was likely a detrimental amount of crystallization within the glass. This proves to be an important characteristic of glass seals. In order to achieve a good seal, the temperature must be raised beyond the glass transition temperature for a period. However, if the sustained temperature is too high there may be some level of crystallization which can be detrimental to the seal performance.

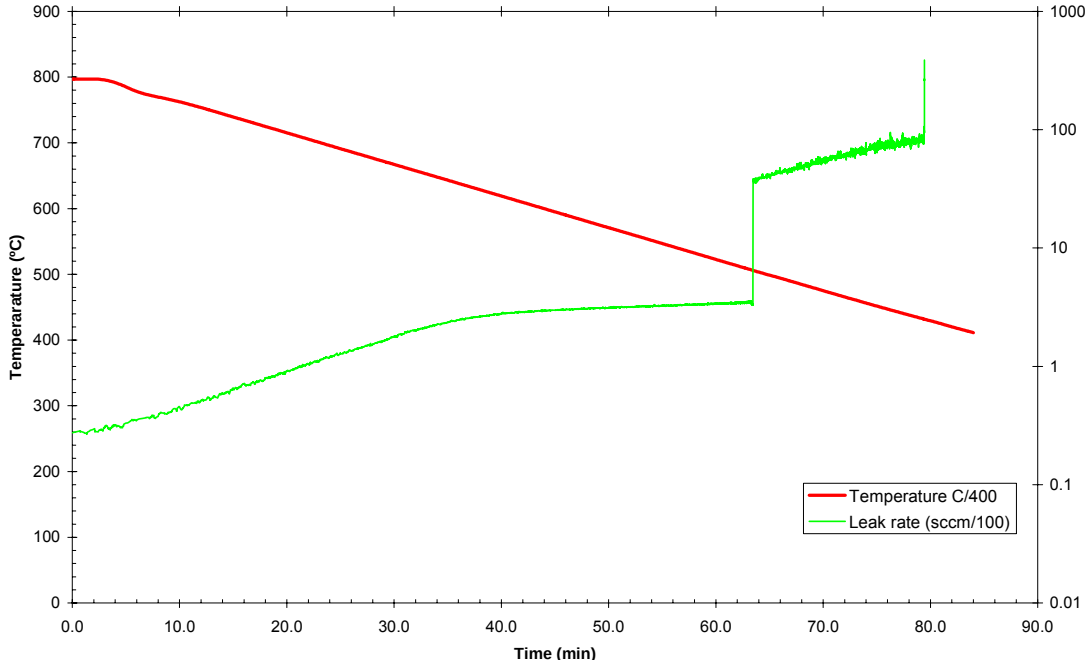

Figure 28 Sample 2 UMR #27 - first thermal cycle

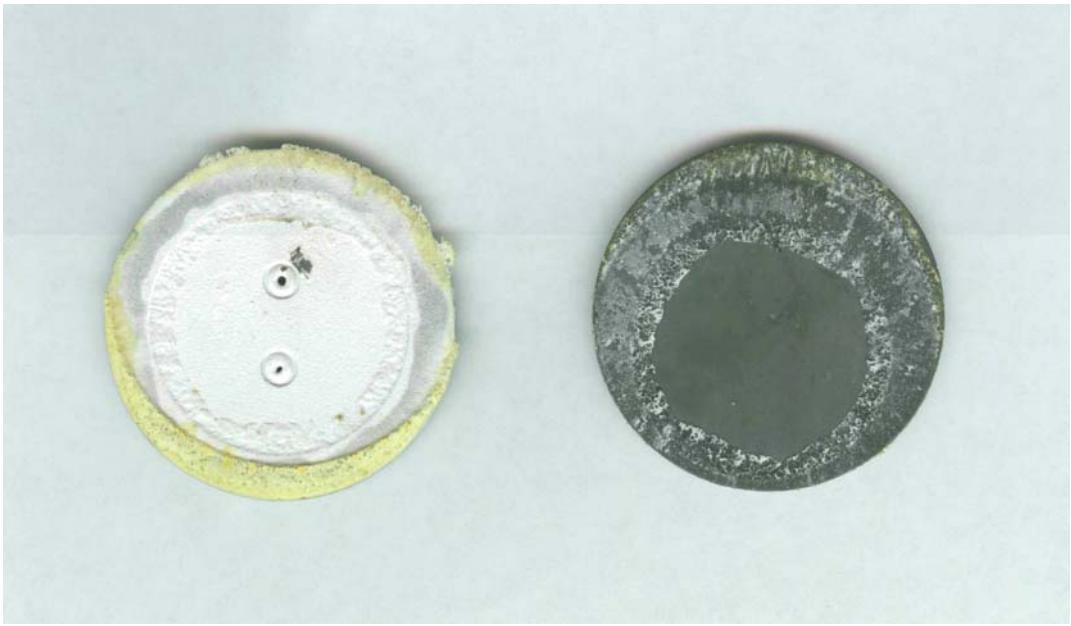

Figure 29 Seal sample 2 UMR#27 glass - post thermal cycle

Sample 5 presented the best thermal cycle performance of all the glass filler composite seals tested. Figure 30Figure 35 show the 63 thermal cycles of the Singh glass to APS ceramic coating sample. The first 15 cycles shown in Figure 30 and Figure ***31***were done between 650 and 250^{o}C at a rate of 5 ^{o}C/min. At these parameters there was very little deviation from the initial leak rate of 0.022 sccm/cm. However, when the low temperature was changed to 150^{o}C, the leak rate at the low temperature jumped to approximately 0.045 sccm/cm which indicates some level of cracking or seal degradation. Upon reheating, the seal did "self-heal" to the point where the leak rate went back down below 0.03 sccm/cm. This suggests that a good "wet" seal is achieved at the higher temperatures. After 30 thermal cycles between 650 and 150 ^{o}C, the seal was allowed to cool down to room temperature. At that point the leak rate increased dramatically to approximately 0.36 sccm/cm (Figure 33). Again upon reheating the sample resealed such that the seal integrity was at approximately the level it was prior to cooling to room temperature. However, when the sample is continually thermal cycled from 100 to 800^{o}C, there is permanent damage to the seal such that the leak rate at the high temperature increases to approximately 0.9 sccm/cm as shown in Figure 34. This permanent damage was likely due to

crystallization at the high temperature. Figure 35shows that the seal continued to degrade up until the 63rd and final thermal cycle. The final high temperature leak rate of approximately 1.9 sccm/cm remained unchanged when the sample was reheated and held at a temperature of 900°C (Figure 36). The sample gain showed signs of crystallization. This crystallization was irreversible by reheating. Since the crystals do not flow and fill voids as does the glass material, the semi-crystallized material was not capable of adequately sealing the sample.

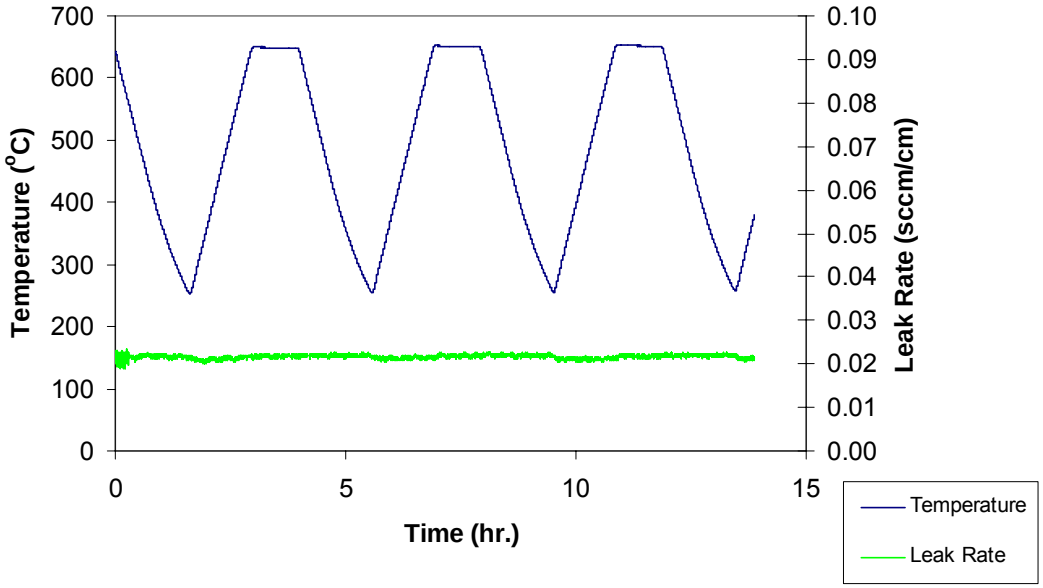

Figure 30 Singh glass - thermal cycle 1-3

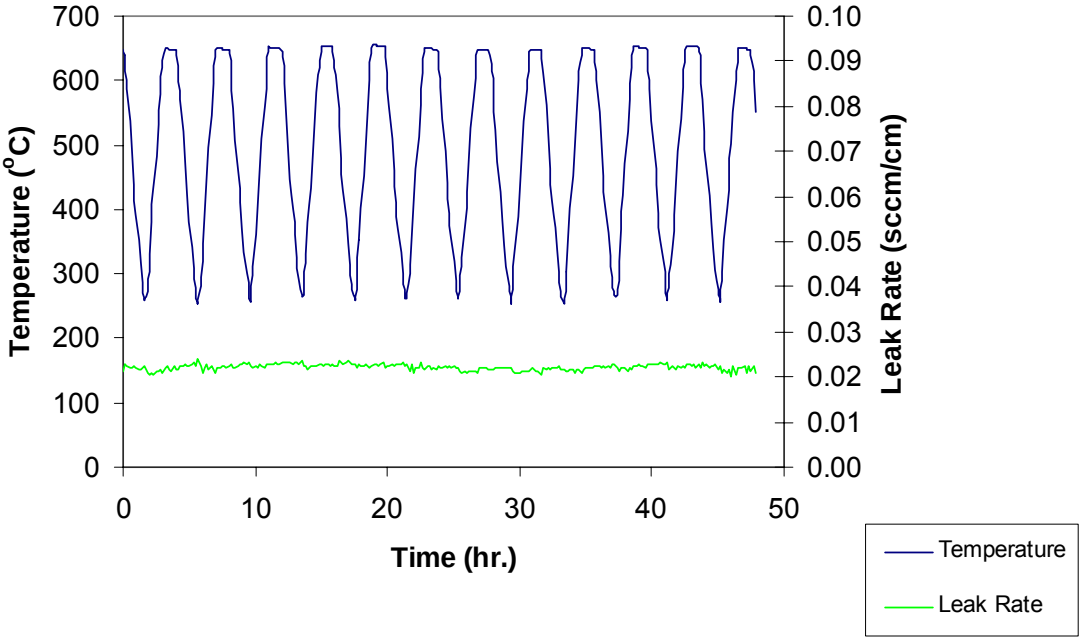

Figure 31 Sample 5 Singh glass - thermal cycles 4-15

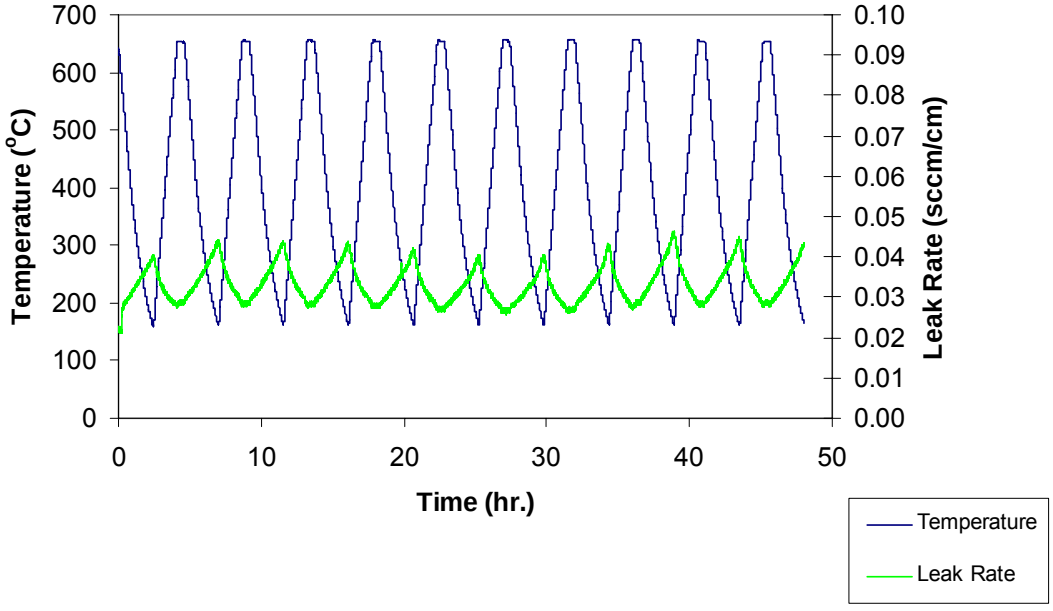

Figure 32 Sample 5 Singh glass - thermal cycles 16-25

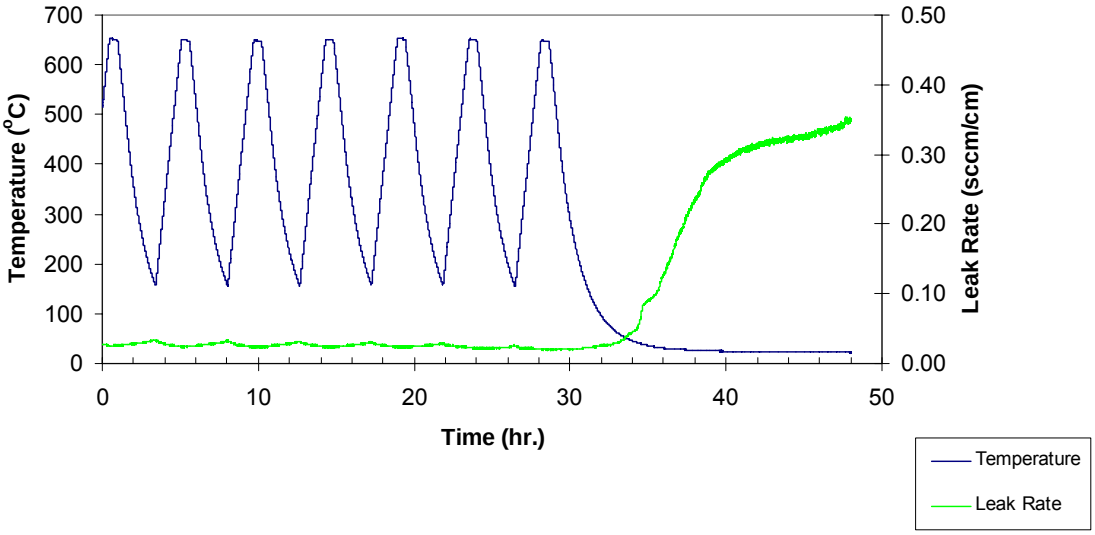

Figure 33. Singh glass thermal cycles 26-30

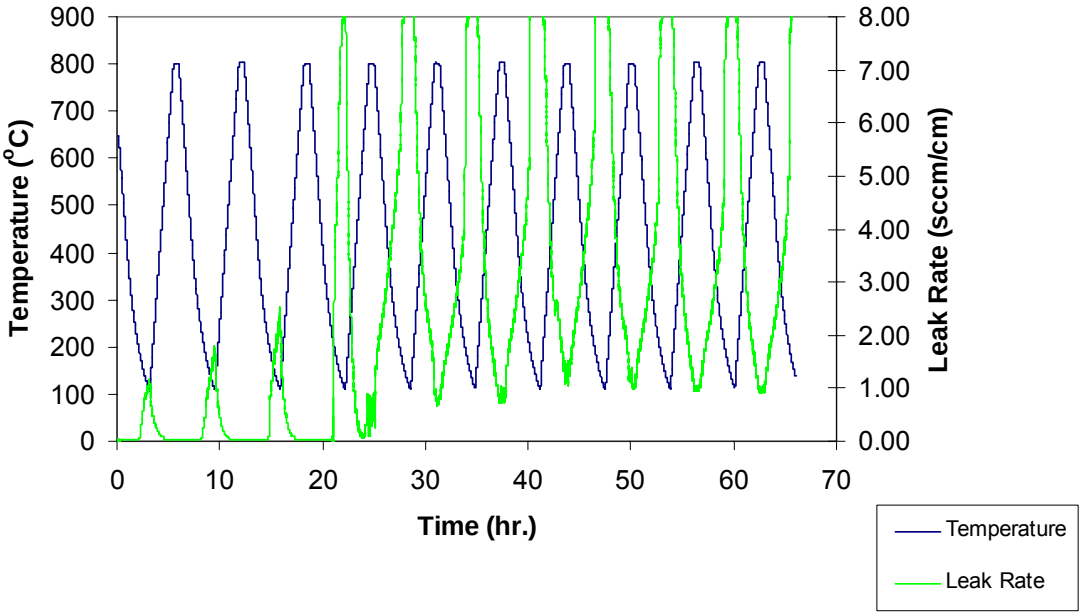

Figure 34 Sample 5 - Singh glass thermal cycles 26-30

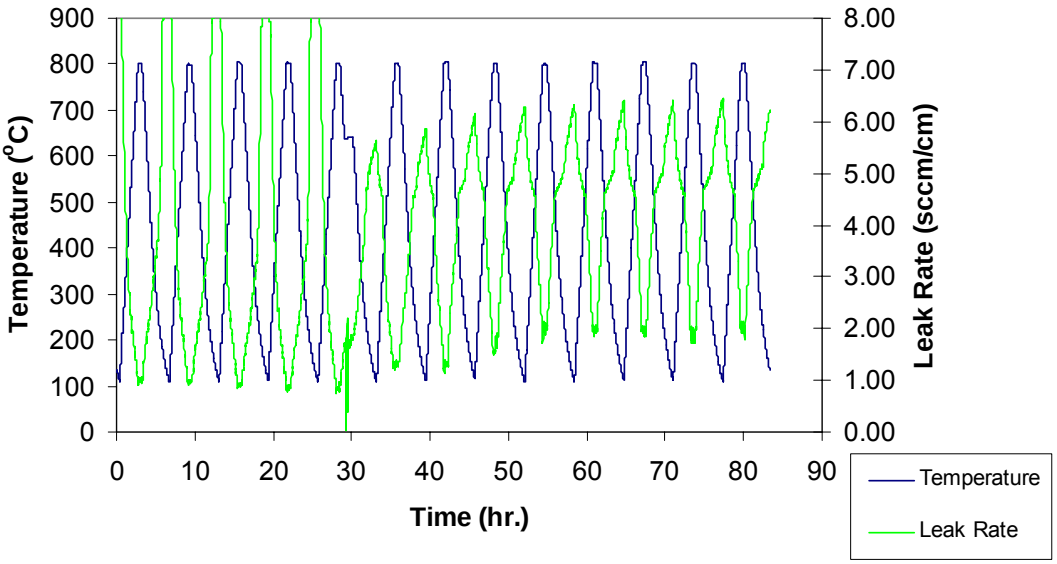

Figure 35 Sample 5 - Singh glass thermal cycles 51-63

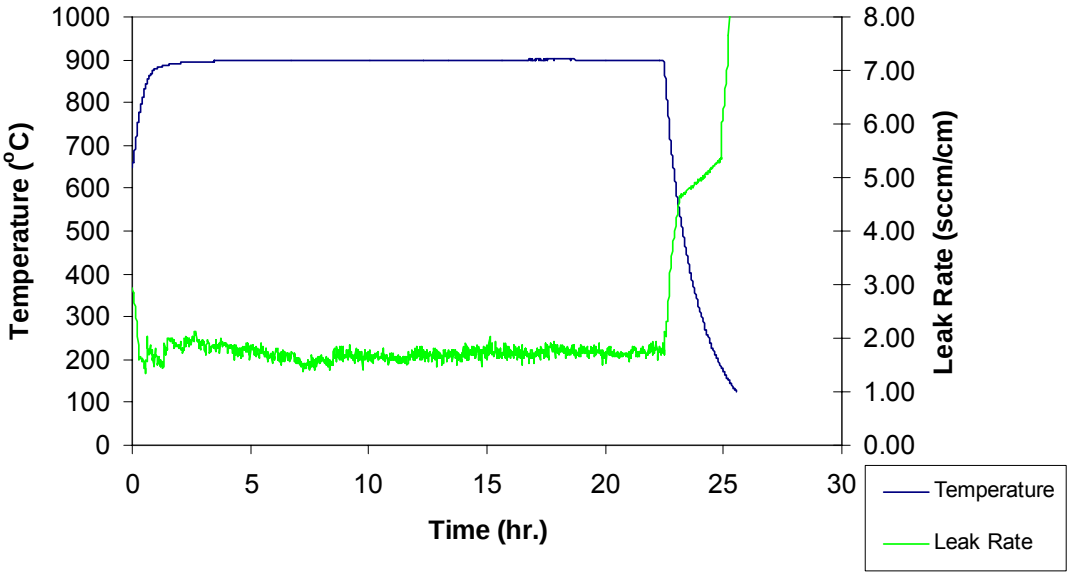

Figure 36 Sample 5 - Singh glass high temperature dwell after 63 thermal cycles

The SNL glass had similar properties to the previous two glasses during thermal cycling. Figure 37 illustrates that the leak rate was quite low at the beginning of

thermal cycling and in fact upon the second thermal cycle the leak rate actually decreased below 0.01 sccm/cm which is the lowest leak rate achieved by the glass/APS ceramic seal. The seal test data again indicated that leak rate decreases with increasing temperature from 450°C to the operating temperature probably due to the glass flow creating a "wet" type seal. Leak rate then dramatically increased when temperature dropped upon cooling to around 300°C probably due to cracking. Further investigation into the potential cracking issue is presented in section 4. During the third cycle, the seal had signs that it was degrading. The seal continued to degrade until testing stopped after 10 thermal cycles. In the end, the degradation leveled off to a high temperature leak rate of around 1 sccm/cm. This leak rate is comparable to the leak rate shown in the Singh glass sample suggesting a similar crystallization type failure. Yang et al., Misture et al, and Eichler et al., have established that control of glass crystallization, viscosity and glass transition temperatures is of vital importance when designing a glass-type seal for high temperature SOFC application [8,9]. The results from thermal cycle testing at CGFCC support these previous observations.

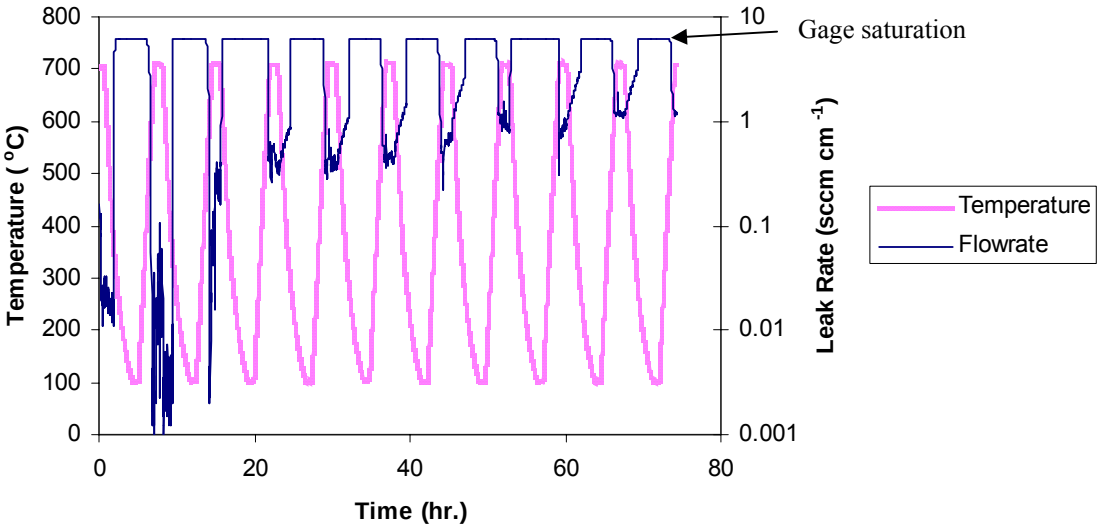

Figure 37 Sample 9 - SNL glass thermal cycles 1-10

The thermal cycle test represented in Figure 38 involves the same APS ceramic on metal substrate, however, the main filler material was a compressive metal

seal in this case a gold o-ring. Performance for this type seal, in contrast to the glass-type seals, actually improved during thermal cycling. The initial leak rate was about 0.125 sccm/cm and after ten (10) thermal cycles the leak rate was about .070 sccm/cm. It is theorized that as the gold o-ring is thermal cycled, the softening and the relative movement of the materials due to CTE mismatch allows the gold material to work into the surface roughness of the APS ceramic top coat of the substrate creating smaller and smaller surface leak paths. This suggests that by decreasing the surface roughness of the substrate, one could achieve better sealing performance when a metal compressive seal is utilized for the filler material.

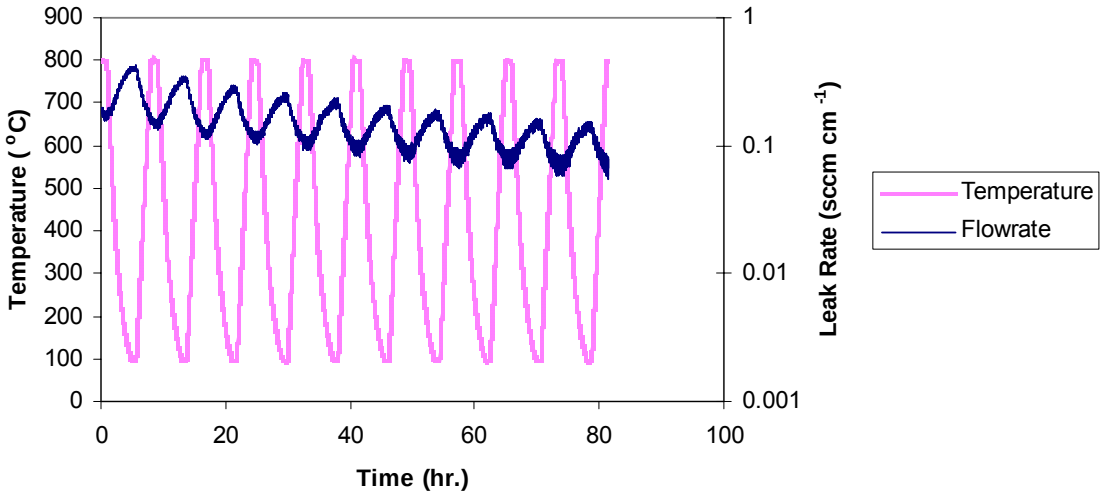

Figure 38 Sample 7 – gold o-ring seal thermal cycle performance

4. MECHANICAL TESTING & MODELING

As a critical building block of the multilayered composite seal, it is necessary that the ceramic coating is mechanically robust under an SOFC operation conditions. Thermal shock test and tensile adhesion test were employed to characterize the mechanical robustness of the coating.

The composite seal will be subjected to thermo-cycling during the start up and shutdown of SOFC stacks. Usually, the heating and cooling rate is on the order of 1 ºC/minute. In this investigation, a thermal shock test was used instead. The test is relatively easy to perform and it represents a much more severe thermo-mechanical loading conditions. The coated button samples (25.5mm dia.) were heated to 850 ºC. After dewelling for 15 minutes at that temperature, the samples were quick quenched into a cold water batch. This procedure was then repeated three times for each sample. No spallation was observed. Visual examination indicated the coating was intact after thermal shocks.

Tensile Adhesion Test

Standard tensile adhesion tests (ASTM C633-01) were conducted on plasma sprayed ceramic coatings to evaluate mechanical pull-out strength. Ceramic coated button samples were used. Steel pull rods were bonded to the either side of the coated button sample with FM1000 epoxy adhesive from Cytec Engineered Materials Inc. The pull-out bar was connected through two universal joints to an Instron servo hydraulic loading frame. The samples were pulled apart with a cross head speed of 0.015mm/sec. A total of 5 samples were tested and the results are summerized in Table 7. The average tensile strenth of the coating is found to be 31.97 MPa with a standard deviation of 7.63MPa. The fractured surface show that the crack propagted partially through the bond coat and partilly through the top coat. The strength data show that the ceramic coating formed a failrly strong bond with the Fe-Cr alloy substrates.

Table 7 Results of tensile adhesion test

	Failure load (lbf)	Failure stress (MPa)
Average	3527.7	31.97
Standard Deviation	841.9	7.63
Mimimum value	2492.4	22.59
Maximum value	4729.9	42.86

Attemp was made to measure through-the-thcikness modulus of the ceramic coating. Four clip gages were used to measure deformation in a span across the ceramic layer and the deformation of the steel cylinder was canceled out throught a test scheme. The result indicated that the modulus of ceramic layer was about *17~23GPa.*

Tensile adhesion test was also conducted for a composite seal with G18 glass as the filler. The result is show in

Table 8. Result of tensile adhesion test of composite seal with G18 glass as filler.

	Pullout Force		Failure Stress	
	N	lbf	MPa	Ksi
	3867.3	869.4	11.27	1.63
	8771.9	1972.0	23.50	3.41
	8690.6	1953.7	25.09	3.64
	5200.3	1169.1	12.96	1.88
	4322.4	971.7	11.27	1.63
avg.	6170.5	1387.2	16.82	2.44
std.	2134.5	479.9	6.16	0.89

Interface fracture toughness

SOFC seals are susceptible to fracture during thermal cycling. The strength of the bond at the interface is an important parameter in stack design. This is characterized in different ways depending on the failure modes considered most critical in the application. An SOFC stack typically has a structural frame that provides compression, which reduces the tendency of the layers to peel off in mode I fracture. However, their tendency to slide relative to each other due to thermal expansion mismatch is not reduced. Hence, the loading of sealed interface is expected to have a strong shear component; the fracture is expected to be mixed mode (I+II). Therefore it is desirable that the fracture test method reproduce a similar degree of mode mixity. The tests used to evaluate fracture toughness are the four-point beam bending test, and the 3-point mixed mode flexure test.

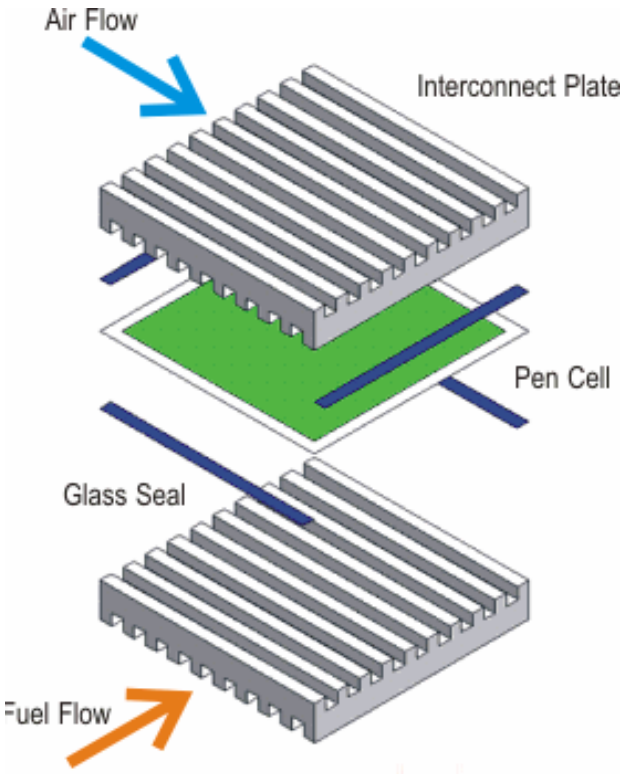

Figure 39 Schematic of a planar SOFC stack (Source:azom.com)

Previous studies [10] indicate that the fracture toughness of the plasma coated ceramic layer on metal substrate can be very high. This was further verified by

quenching a beam coated with the ceramic layer and heated to 800C, in water at room temperature. Even after this severe thermal shock, the ceramic coated layer remained intact. In comparison, the interface between the glass and the ceramic layer is much weaker and further investigations are concentrated at this interface. This section presents a brief overview of fracture mechanics, describes the methods used in this study and the results obtained.

3.1 Fracture Mechanics

Fracture loading is commonly characterized using 2 parameters [11]- the strain energy release rate and the stress intensity factor. Both of these parameters vary with specimen geometry and loading conditions.

The energy release rate is defined as the energy required for crack growth, or conversely, strain energy released from crack extension. This approach assumes that the crack grows when the energy available for crack extension exceeds the inherent resistance of the material. Accordingly an experimentally measured parameter called fracture toughness 'G_c', representing the minimum energy release rate at which crack growth occurs, is used to determine if a crack will propagate.

The stress intensity factor is mathematically defined as the amplitude of the stress field near the crack tip. This parameter describes the intensity of the geometrical distribution of stresses near the crack tip. Based on the nature of the driving force, fracture is classified into 3 main types – mode I represents opening type of fracture, mode II represents shear fracture and mode III refers to fracture caused by out-of-plane stresses.

The energy release rate and the stress intensity factor are related by

$$G = \frac{K_I^2}{E} + \frac{K_{II}^2}{E} + \frac{K_{III}^2}{2\mu} \qquad (0.1)$$

Where G is the energy release rate, K_I, K_{II} and K_{III} are the stress intensity factors corresponding to the various fracture modes, E and μ are the Young's modulus and shear modulus respectively.

Interfacial fracture represents a more complicated case than fracture in a single material, due to the oscillating nature of the associated stress singularity near the crack tip [12]. Due to the difference in elastic properties of the 2 materials, considerable asymmetry exists even if geometry and loading are symmetrical, causing the fracture in this case to be mostly mixed mode. The dependence of the fracture properties on the elastic properties of the systems is expressed in terms of non-dimensional Dundurs' parameters [13]:

$$\alpha = \frac{\Gamma(\kappa_2 + 1) - (\kappa_1 + 1)}{\Gamma(\kappa_2 + 1) + (\kappa_1 + 1)} \tag{0.2}$$

$$\beta = \frac{\Gamma(\kappa_2 - 1) - (\kappa_1 - 1)}{\Gamma(\kappa_2 + 1) + (\kappa_1 + 1)} \tag{0.3}$$

Where subscripts 1 and 2 refer to the 2 materials, $\kappa = 3 - 4\nu$ for plane strain and $\kappa = \frac{3-\nu}{1+\nu}$ for plane stress, $\Gamma = \frac{\mu_1}{\mu_2}$, 'μ' is the shear modulus and 'v' is the Poisson's ratio. The stress intensity factor for this case is complex and is generally represented as $K = K_1 + iK_2$.

Prior experimental and analytical studies [15] indicate that the presence of a small sandwich layer does not change the energy release rate so much as it affects the phase angle of loading.

The relationship between the stress intensity factor and energy release rate for this case is given by

$$G = \frac{c_1 + c_2}{16\cosh^2 \pi\varepsilon} |K|^2 \tag{0.4}$$

Where $c = \frac{\kappa + 1}{\mu}$ and $\varepsilon = \frac{1}{2\pi} \ln \frac{1-\beta}{1+\beta}$.

Closed form solutions exist for interface cracks in bimaterial system [14], sandwich specimens [15] and for a 3 material sandwich [16], but these are limited in the fact that they generally require constants that need to be numerically determined for every material combination.

The phase angle of loading for the given combination is expressed as

$$\psi = \tan^{-1}\left[\frac{\mathrm{Im}\left[KL^{i\varepsilon}\right]}{\mathrm{Re}\left[KL^{i\varepsilon}\right]}\right] \qquad (0.5)$$

Where 'L' is a characteristic length scale that depends on the given geometry. The length scale typically used in interfacial fracture is the thickness of the interfacial layer. As $\varepsilon \rightarrow 0$, the phase angle represents the relative strength of the mode I and mode II stress intensity factors.

3.2 Analytical methods

Accurate determination of fracture toughness requires optimal specimen geometry to get best results. Specimens are generally designed using analytical models that make simple assumptions about material properties and the nature of deformation This section describes the analytical models used to estimate the energy release rate for the test configurations.

3.2.1 The four-point beam bending test

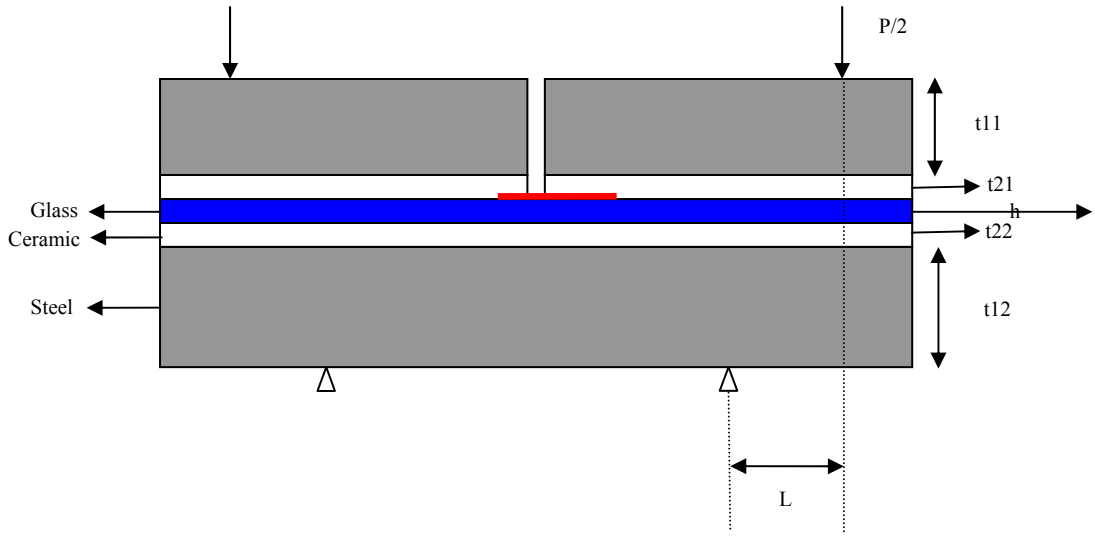

Figure 40 Schematic of four point bending test

The 4 point beam bending test was used by Charalambides et al [17] to characterize mixed mode fracture in bimaterial systems. But the method has since been successfully applied to sandwich specimens [18], and in particular to determine fracture toughness of a plasma-sprayed ceramic layer [10].

A schematic of the test geometry is shown in Fig. 41, for a system made of 3 materials. 'P' represents the applied load, 'L' the distance between the load line and the support and 'B' the sample width. In this section, an analytical formula is derived for estimating the energy release as a function of the test geometry, material and loading parameters.

The bending moment, which is the driving force for crack propagation, is constant between the inner span. This results in steady state propagation of the crack between the inner loading line (between the 2 supports), and enables estimation of energy release rate independent of crack length.

The energy release rate G is defined as the energy released per unit length of crack propagation per unit sample width. In the case of interfacial fracture, the energy driving the crack comes from the strain energy difference between the energy stored in the full composite beam, and the energy stored in the lower

uncracked portion, as the top cracked portion is released from the load after cracking.

$$G = \frac{1}{B}\frac{dU}{da} = \frac{1}{B}\frac{(U_{uncrackedbeam} - U_{crackedbeam})}{da} \tag{3.1}$$

The strain energy U stored in a beam of length 'x' with moment of inertia 'I' under a moment 'M' undergoing pure bending is given[19] by

$$U = \int_0^x \frac{M^2}{2EI} dx \tag{3.2}$$

Here the moment 'M' and section moment of inertia 'I' may vary over the length 'x' of the beam. The strain energy per unit area of crack extension undergoing pure bending for the four-point beam bending test, in which moment is constant for a crack between the inner loading lines, is dependent only on the moment of inertia of the section.

$$G = \frac{M^2}{2B(EI)_{crackedbeam}} - \frac{M^2}{2B(EI)_{uncrackedbeam}} = \frac{M^2}{2B}\left(\frac{1}{(EI)_{crackedbeam}} - \frac{1}{(EI)_{uncrackedbeam}}\right) \tag{3.3}$$

where M is the bending moment, E is the Young's modulus, B is the specimen width and I is the moment of inertia of the section.

Thus the energy release rate for a crack in the top ceramic glass interface is equal to the strain energy difference in the cracked and uncracked beams and is given by

$$G_{ss} = \frac{M^2}{2BE_1}\left[\frac{1}{I_{c3}} - \frac{1}{I_{c5}}\right] \tag{3.4}$$

where Ic_3 and Ic_5 are the moments of inertia of the cracked and uncracked beam sections respectively and 'E_1' the elastic modulus of the bottommost layer.. For the given test configuration, the moment M is given by

$$M = \frac{PL}{2} \tag{3.5}$$

The moments of inertia of the composite beams are calculated using the transformed section method. This method states that the moment of inertia of a multimaterial composite beam can be estimated by replacing the width B of one of the material layers (with Young's modulus E1) with width ηB, where

$$\eta = E1/E2 \tag{3.6}$$

The new position of the neutral axis of the beam based on the transformed areas is then found using

$$y = \frac{\sum_{i}^{n} A_i y_i}{\sum_{i}^{n} A_i} \tag{3.7}$$

where A_i is the area of section i, and y_i is the height of the centroid of section i above the reference axis (which is placed at the specimen base).

For the test specimen,

$$I_{c5} = B\left[\begin{array}{l} \frac{1}{12}\left(t_{12}{}^3\right) + t_{12}(\frac{t_{12}}{2} - y)^2 + \frac{1}{12}\eta_2\left(t_{22}{}^3\right) + t_{22}\eta_2(\frac{t_{12}}{2} + t_{22} - y)^2 + \\ \frac{1}{12}\eta_3\left(h^3\right) + h\eta_3(\frac{h}{2} + t_{12} + t_{22} - y)^2 + \frac{1}{12}\eta_2\left(t_{21}{}^3\right) + \\ t_{21}\eta_2(\frac{t_{21}}{2} + h + t_{12} + t_{22} - y)^2 + \frac{1}{12}\left(t_{11}{}^3\right) + t_{11}(\frac{t_{11}}{2} + t_{21} + h + t_{12} + t_{22} - y)^2 \end{array}\right] \tag{3.8}$$

where $\eta_2 = \frac{E2}{E1}$, $\eta_3 = \frac{E3}{E1}$,E1 – Steel, E2 – Ceramic, E3 – Glass and y is the new position of the centroid obtained from

$$y = \frac{\left[\begin{array}{l} t_{12}(\frac{t_{12}}{2} - y) + t_{22}\eta_2(\frac{t_{12}}{2} + t_{22} - y) + h\eta_3(\frac{h}{2} + t_{12} + t_{22} - y) + \\ \eta_2 t_{21}(\frac{t_{21}}{2} + h + t_{12} + t_{22} - y) + t_{11}(\frac{t_{11}}{2} + t_{21} + h + t_{12} + t_{22} - y) \end{array}\right]}{t_{12} + t_{22}\eta_2 + h\eta_3 + \eta_2 t_{21} + t_{11}} \tag{3.9}$$

The moment of inertia of the cracked beam I_{c3} is due to the lower portion of the beam which is still bending, and is obtained by setting t_{11} and t_{21} as zero in Eq.

3.6. It is to be noted that the energy release rate for any crack configuration can be obtained from these equations by setting the appropriate layers to zero thickness.

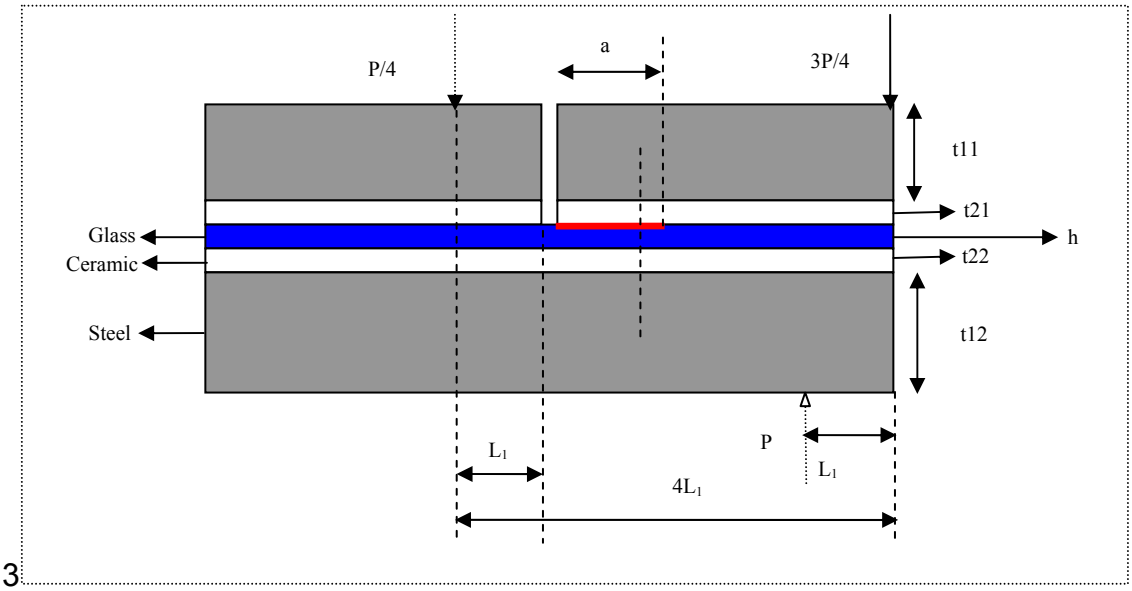

3

Figure 41 Schematic of mixed mode flexure test

3.2.2 Three-point mixed mode flexure test

As shown in Fig 42, this test is a modified version of the simpler 4-point bending test. This test provides fracture toughness measurements with a higher level of mode mixity, which is closer to the actual conditions in a planar SOFC stack. It also provides 2 independent fracture surfaces for each sample made. However, it requires accurate determination of the length of the pre-crack to determine energy release rate, as the driving force varies with the length of the crack.

The pre-crack is generated using the traditional symmetrical 3-point bend test shown in Fig 43. The advantage of this mode of opening the crack is that the bending moment, which is the driving force for crack extension, decreases linearly as the crack extends, thus limiting crack growth.

The crack length is estimated by measuring the stiffness of the cracked and uncracked beams as described below.

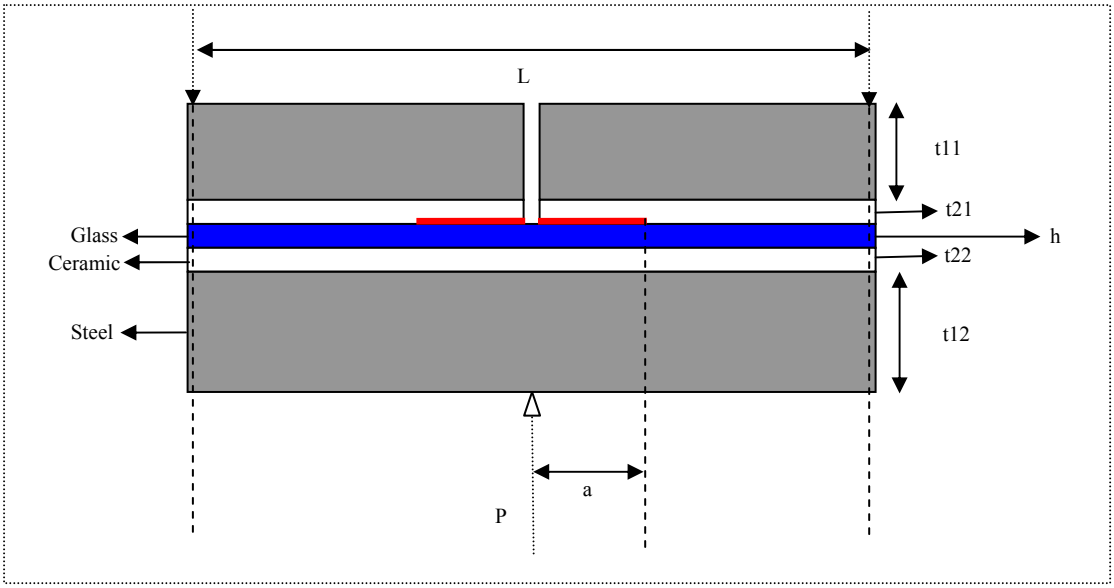

Figure 42 Schematic of 3-point bend test

The compliance is estimated using the moment-area approach. The second moment-area theorem states that the tangential deviation $t_{B/A}$ of point B from the tangent at point A is equal to the first moment of the area of the M/EI diagram between A and B, evaluated with respect to B.

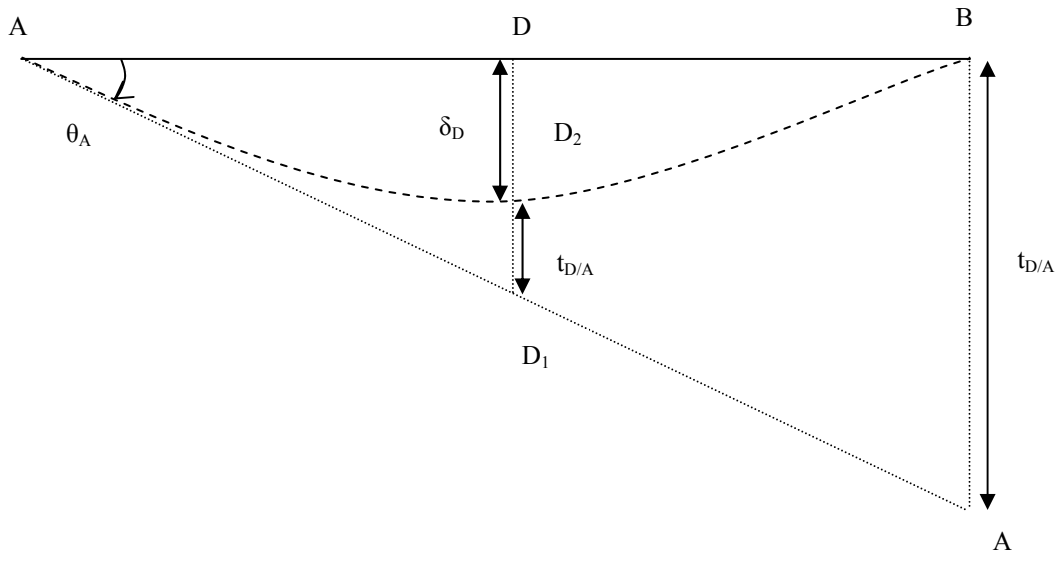

Figure 43 3-point beam bending – deflections and slopes

Fig 44 shows the beam with the deflected shape exaggerated for clarity. The deflection at mid-point D is δ_D, and is found as follows.

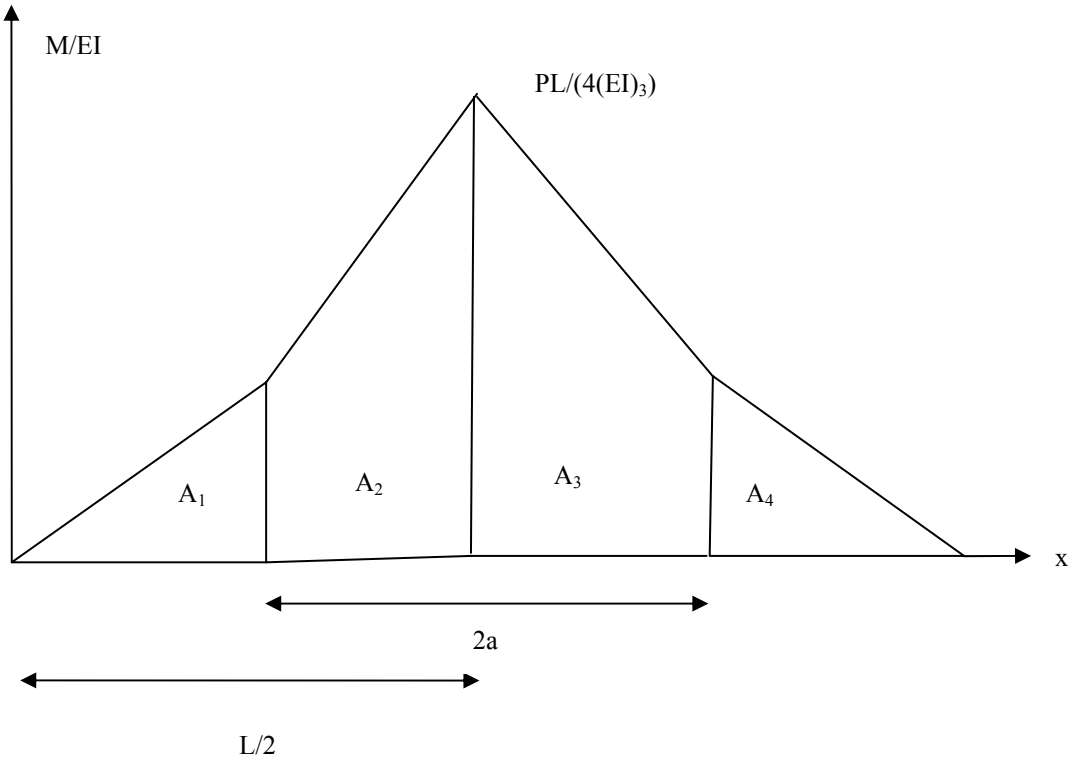

Figure 44 Moment-area diagram for 3 point-beam bending

The tangential deflection of point B with respect to A in Fig 44 is given by the first moment of the area of the M/EI diagram shown in Fig 45.

$$t_{B/A} = A_1 x_1 + A_2 x_2 + A_3 x_3 + A_4 x_4 \tag{3.10}$$

Similarly, the tangential deflection of point D with respect to A is

$$t_{D/A} = A_1 x_1 + A_2 x_2 \tag{3.11}$$

The slope at support A is seen to be

$$\theta_A = \tan^{-1}\left(\frac{t_{B/A}}{L}\right) \tag{3.12}$$

Therefore the deflection at the mid-point is

$$\delta_D = \frac{L}{2}\tan\theta_A - t_{D/A} \tag{3.13}$$

The stiffness of a beam with a symmetric crack of length '2a' can be calculated from the load P/ δ_D. The stiffness of a cracked beam obtained from experiments is compared with this stiffness, and the crack length is calculated from this. It is worthy of mention that the flexural rigidity 'EI' of the composite beam used in this calculation are those obtained experimentally from the specimens.

The energy release rate for this configuration is derived in a manner similar to the previous derivation, except that in this case the bending moment varies along the length of the crack.

The bending moment at the crack tip is given by

$$M = \frac{P(L_1 + a)}{4} \tag{3.14}$$

Proceeding in a manner similar to that described earlier, we get the energy release rate per unit area of crack extension as

$$G = \frac{P^2 \left(L_1 + a\right)^2}{32BE_1}\left(\frac{1}{I_{c3}} - \frac{1}{I_{c5}}\right) \tag{3.15}$$

Finite element analysis (FEA)

FEA is used to determine the accuracy of the analytical model and to calculate phase angle and thus the extent of the mode mixity. FEA was performed using the commercial code Abaqus. The values of the material properties for the finite element and analytical calculations are given in Table 8 below.

Table 9 Material properties used in fracture analysis [9]

Material	Young's Modulus	Poisson's ratio
Crofer 22	160 GPa	0.3
Ceramic layer	80 GPa	0.3
ESL 4460 glass	40 GPa	0.3

It is assumed in the FEM analysis that there is no residual stress in any of the layers in the coating.

3.3.1 J-integral calculation

The J-integral is a path-independent line integral used to calculate energy release rate for non-linear elastic systems [20]. The methods used by Abaqus to calculate this parameter are described in great detail in the Abaqus Theory Manual, and are summarized in this section.

ABAQUS defines the domain in terms of rings of elements surrounding the crack tip. Different “contours” (domains) are created. The first contour consists of those elements directly connected to crack-tip nodes. The next contour consists of the ring of elements that share nodes with the elements in the first contour as well as the elements in the first contour. Each subsequent contour is defined by adding the next ring of elements that share nodes with the elements in the previous contour. The value of the J-integral is then calculated at each contour using the domain integral method – which applies divergence theorem to convert the line integral into an area integral for a 2-D model.

The J-integral should be independent of the domain used provided that the crack faces are parallel to each other, but J-integral estimates from different rings may vary because of the approximate nature of the finite element solution. Strong variation in these estimates, commonly called domain dependence or contour dependence, typically indicates an error in the contour integral definition. The path-independence of the J-integral was verified for every analysis performed, and a sample graph showing the variation of J is shown below in Fig 46. This represents the value of the J-integral at each contour – the innermost contour being 1, for the 4-point test performed on the metal-ceramic-glass system.

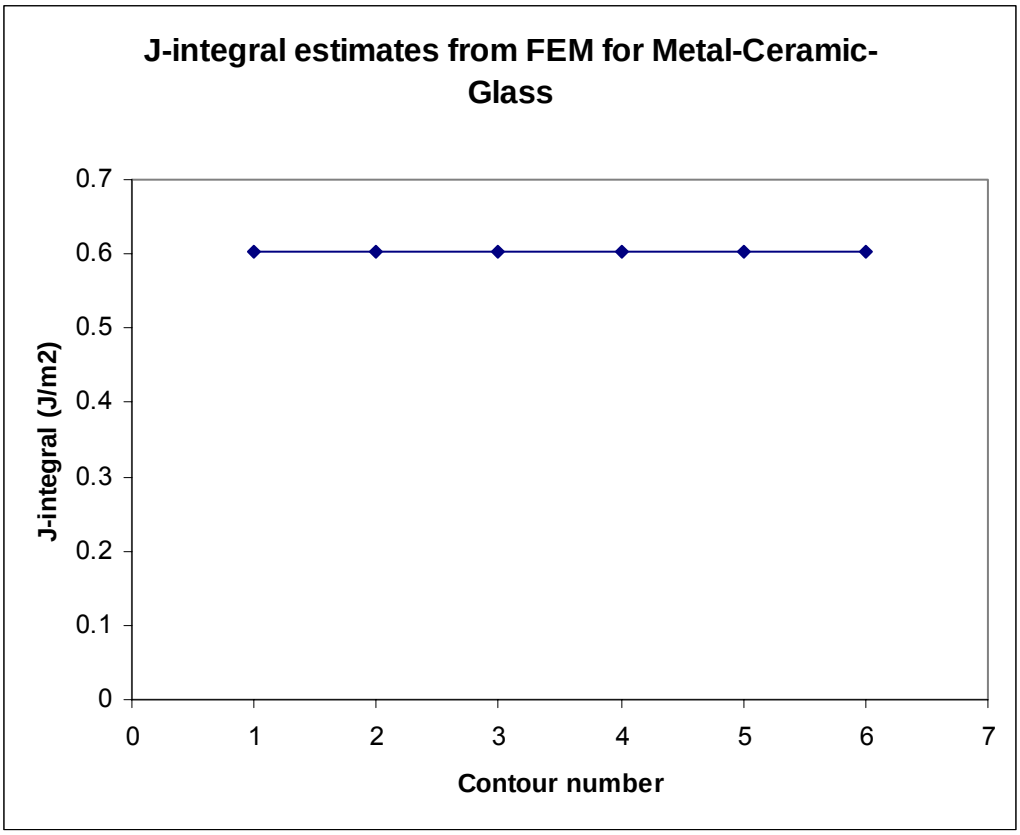

Figure 45 Contour independence of the J-integral

3.3.2 Stress intensity factor

The stress intensity factor is related to the energy release rate by

$$J = \frac{1}{8\pi} K^T \cdot B^{-1} \cdot K \tag{3.16}$$

Where B is known as the pre-logarithmic energy factor matrix. For homogenous, isotropic materials, B becomes diagonal, and Eq. 3.10 reduces to

$$J = \frac{1}{\bar{E}}(K_I^2 + K_{II}^2) + \frac{1}{2G} K_{III}^2 \tag{3.17}$$

The individual stress intensity factors are then extracted from J using the interaction integral method [21].

3.3.3 Four-point beam bending test

In modeling the 4-point beam bending test, symmetry simplifies the model to a

half-beam model. The model had the same dimensions as the test case, and symmetry boundary conditions were imposed on the half-plane. A crack length of 10 mm was chosen to be fairly representative of the experimental cases, and phase angles were extracted from the FEM models for this value of the parameter.

The model used eight-noded quad plane strain elements (CPE8). A refined mesh near the crack tip contained 6 rows of sweep-meshed quad elements meshed over a length ‘h/2’.

3.3.4 Three-point mixed mode flexure test

Due to the inherent lack of symmetry in the loading conditions in this test, the full specimen is modeled in Abaqus. This model had the same dimensions as the test specimen, and the load and supports are applied at the same corresponding spots. A crack length of 3 mm was used as it represented the typical crack length observed in the tests. The mesh used eight-noded quad plane strain elements (CPE8). The mesh near the crack tip contained 6 rows of sweep-meshed elements over a length ‘h/2’.

3.4 Experimental procedure

Two types of sandwich specimens were used in the test – type A which consisted of 2 Crofer beams with a layer of ESL 4460 glass in between, and type B which consisted of 2 ceramic coated Crofer beams with a layer of ESL 4460 in between.

The specimens consisted of bars of Crofer 22 with and without a ceramic layer (about 220 X 12 X 1.5 mm) sandwiching a layer of ESL 4460 glass (100 microns) in between. The bars were first cut to required size, and their edges ground using 600-grit sandpaper to remove burrs and provide a flat surface. They were then ultrasonically cleaned in water for 10 minutes, dried and swabbed with acetone to remove surface contaminants. They were handled using latex gloves throughout

this process. The glass layer was then applied on the metal surface to form a sandwich specimen. This specimen was then heated to a temperature of 125C for 1 hour. Next, the specimen was placed in a high temperature oven under pressure and heated to a temperature of 850C to cure the seal layer. The heating rate used was 3C/min and the cooling rate was 2C/min, and the specimen was maintained at 800C for 30 minutes to relieve thermal stress. All subsequent tests were carried out using an Instron 5800 testing machine equipped with a 1 KN load cell.

A pre-crack was generated in the top glass-metal by loading the specimen in a 3-point bending test fixture. This configuration is preferred for generating pre-cracks as the bending moment, which is the driving force for crack growth, decreases with increasing crack length. The crack is also arrested from progressing further by using clamps to hold the beam together. The crack length was monitored and measured visually, as well as by monitoring the specimen compliance as explained earlier.

The pre-cracked specimen was loaded onto the 4-point flexure fixture. The test was controlled by displacement control, which generates stable crack growth, at the rate of .0025 in/min. Since the glass layer is thin (60-80 microns) it is not easy to detect crack growth visually until the crack becomes long. Therefore, crack propagation is detected indirectly by monitoring the specimen compliance during loading. The load increases initially until the point when crack propagation starts. At this point, there is an increase in displacement that is not accompanied by an increase in load, indicating the onset of cracking. The load at this point is measured as the critical load for crack propagation, and is used for calculating critical energy release rate and fracture toughness using formulae derived earlier. The cracks generated in this stage were initially measured visually, but this was found to be subjective and lacked repeatability. Therefore, the compliance of the pre-cracked specimen was used to calculate the crack length. The specimen is then loaded into the mixed mode flexure test fixture. The loading here is also

accomplished using displacement control at .06 mm/min and crack propagation is monitored in the manner described earlier.

3.5 Results and discussion

The results followed the predictions of the analytical model fairly accurately, and steady state fracture occurred at constant (critical) load for the 4-point test. The critical load was also observed to decrease with increasing crack length in the mixed mode flexure test – which is consistent with a uniform interfacial fracture toughness model. A typical load-displacement plot for the four point bend test is shown below, which illustrates this point.

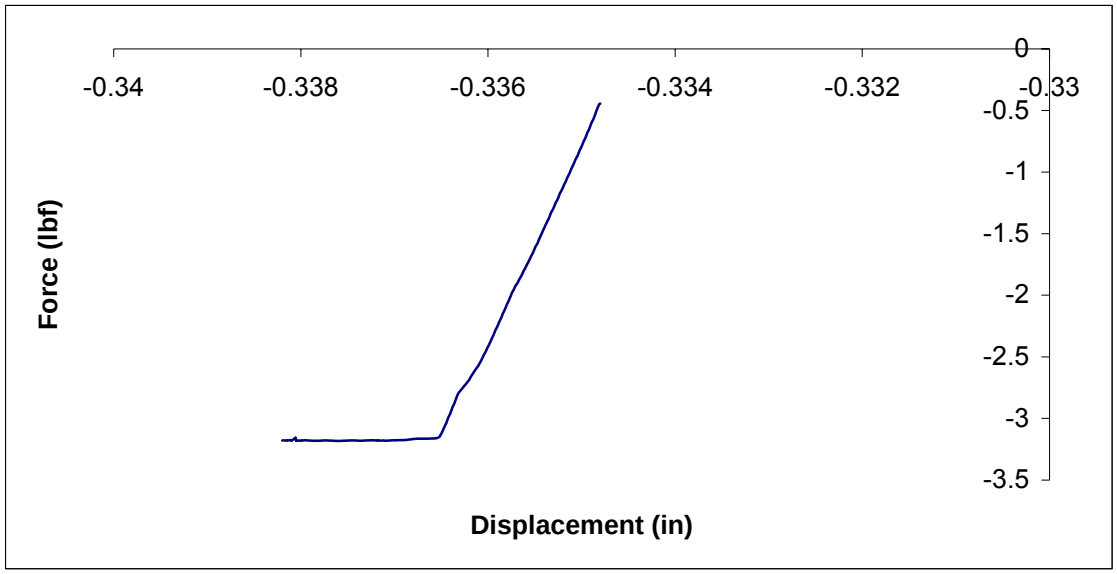

Figure 46 Sample Load-displacement plot

Table 10 Experimental Critical energy release rates

Specimen/Test	G_c (J/m^2) Trial 1	G_c (J/m^2) Trial 2	G_c (J/m^2) Trial 3
Four point bend			
(Metal-Glass)	0.663	0.6672	0.6589
(Metal-Ceramic-Glass)	0.5257	0.5094	0.5257
Mixed mode flexure			
(Metal-Glass)	4.1137	5.038	4.085
(Metal-Ceramic-Glass)	3.796	2.7126	2.6678

The critical energy release rate G_c was calculated by setting the load to the critical load P_c in the analytical model. The value of the critical energy release rate was found from 3 different samples for each test as shown in Table 9, and little variation is seen between the measured values. The interfacial fracture toughness K_c was then determined using Eq. 3.4.

The results of the 4-point bend test are summarized in Table 11 below.

Table 11 4-point beam bending test results

Specimen type	G_c (J/m^2)	K_c (MPa $m^{1/2}$)	Phase angle ψ
Crofer-Glass	0.6630	0.298	16˚
Crofer-Ceramic-Glass	0.5203	0.239	20˚

The mixed mode flexure test results showed more variation, possibly because of the dependence of the energy release rate on the initial crack length. The crack length in these experiments is obtained from beam stiffness calculations, and represents an averaged value rather than the position of the crack front (the average crack length was 0.3 mm for the series of experiments). The results obtained are very sensitive to the value of the crack length used, and hence the results are affected by inaccuracies in determining this parameter.

Table 12 Mixed mode flexure test results

Specimen type	G_c (J/m^2)	K_c (MPa $m^{1/2}$)	Phase angle

			ψ
Crofer-Glass	4.404	1.45	18˚
Crofer-Ceramic-Glass	3.2506	0.87	31˚

By comparing data in Table 10 and 11, one obvious inference that can be made is that the increase in mode mixity is accompanied by an increase in fracture toughness. This indicates that the glass is more resistant to shear than it is to mode I fracture. It should also be noted that the phase angles calculated are dependant on a number of factors that have been assumed – including elastic moduli of glass, ceramic and steel layers.

In addition, the phase angle for interfacial cracks does show a dependence on crack length [22], but the change in phase angle which depends on 'ε', is usually very small for materials with widely differing elastic modulus. Also, tension and shear effects are inherently coupled near interface crack tips, and particular external loadings may not be clearly demarcated as "mode I tension" or "mode II shear".

It is to be noted that the specimens returned to their original shape once the load was removed, which indicates that little plastic deformation occurred. Also, examination of the fracture surface of the Crofer-Glass specimen showed that most of the glass layer had debonded from the top metal surface, which is consistent with the assumptions made. However, for some of the Crofer-Ceramic-Glass specimens, due to the considerable surface roughness and porosity of the ceramic layer, there was some glass seen adhering to the top surface; though less than in the bottom surface. This seems to indicate that the
Also, when the glass was bonded to the metal specimen with a smooth surface, complete wetting was not achieved. This was seen from visual examination of finished samples. The interfacial properties described here are thus (in a way) averaged over the specimen width. The repeatability of the data suggests that

while inhomogeneity may be present in the micro scale, the bonding is fairly consistent when averaged over a larger area.

As an interesting aside, an attempt was made to measure the crack length during fracture more accurately using acoustic emissions monitoring. This involves detecting transient elastic (acoustic) waves generated by the release of energy within the material. In our case, it was expected that the energy released during cracking would generate sufficient acoustic signal to detect the onset of cracking and estimate the position of the crack front while the specimen was still under load. This technique uses 2 acoustic sensors fixed on each end of the specimen; the difference in times an acoustic signal from a fixed point is detected by each sensor is related to the position of the point generating the signal. The sensors were first calibrated to the material properties of the specimen, and then used to monitor cracking in 3-point and mixed mode flexure tests. The method was moderately successful in identifying the onset of cracking, but was not found to be particularly effective in detecting crack length, mainly due to the large signal produced by the crack.

5. CHEMICAL STABILITY STUDY

In this study, the authors attempt to characterize the effect of a ceramic coating (top coat) on the chemical stability of the composite seal samples. Interconnect-glass seal sandwich samples with and without a porous ceramic inter-layers were fabricated and characterized. Selected samples were then aged in air at 800°C for up to 168 hrs. After aging, the degrees of interfacial chemical interactions were characterized by SEM/EDX and EPMA and the results for the two types of samples were compared.

Test Procedure

Sample Preparation: Ferritic stainless steel AL 453 and Crofer were used in this study. The alloy composition of AL 453 is shown in Table 13. The 1.9mm rolled sheet was cut into 25mm disks (substrates) for applying ceramic coating. The substrates were grit blasted. A bond coat of $NiAl_5$ was applied to surface with APS. Subsequently, a ceramic top coat with the composition of Al_2O_3 (80wt%) and partially stabilized ZrO_2 (20wt%) was applied on the bond coat. The glass used in this study is from ESL ElectroScience (4460,) a nickel-free, alkali-free aluminosilicates glass ceramics, in the form of thick paste.

Table 13 Composition of AL453 [Product datasheet]

Element	C	Mn	P	S	Si	Cr	Ni	Ti	Al	Ce & La	Fe
Wt%	0.03	0.3	0.02	0.03	0.3	22.0	0.3	0.02	0.6	0.1	Balance

Sample Material Characterization: To establish the basic materials properties of the ceramic coating and glass. X-Ray diffraction (XRD) and linear thermal expansion coefficient (dilatometry) measurement were conducted. The XRD was performed on bare ceramic coating and on the glass with a Druker D8 powder X-Ray diffractometer. The angle scanned is from 10 to 80 degrees with low scan rates and multiple repeats. The Linear thermal expansion was performed using a NETZSCH model 402C pushrod dilatometer in accordance with ASTM E233. The measurement was conducted from room temperature to 1250°C in air with a heating rate of 5K/min.

Stability Tests: The stability study utilized metal-glass sandwich specimens made from AL453 with and without a ceramic interlayer. Alloy strips without the ceramic layer were cut into 10mm X 10mm squares, then ground and polished using 600-grit SiC paper. The samples were then ultrasonically cleaned in ethanol for 10 minutes and rinsed using acetone to eliminate contamination. The samples were handled using rubber gloves from this point. A thin layer of ESL 4460 sealing glass was applied in the form of paste to the samples. After a settling time of 10 minutes, the samples were dried at a temperature of 125°C for 1 hour. The samples were then transferred to a high temperature oven for curing. A dead load pressure of 7 KPa was applied to each of the specimens, and they were heated to 850°C at the rate of 3°C/min. They were held at that temperature for 30 minutes, followed by a dwell period of 30 minutes at 800°C. The samples were then cooled down to room temperature at the rate of 2°C/min. The sample preparation procedure for the ceramic coated specimens was identical except that they were not polished using SiC paper. Half of the specimens thus obtained were subjected to a high-temperature ageing test, and the other half were retained as controls. The aging test specimens were placed in a high temperature furnace and subjected to a constant temperature of 800°C for a week (168 hours) under a pressure of 7 KPa, with controlled heating (2°C/min) and cool-down rates (1°C/min). After aging, the specimens were mounted in epoxy, sectioned and polished to a surface finish of 1 micron for micro analysis.

Results

XRD results of the APS coating show numerous well-defined peaks as shown in Figure 47. The peaks were identified to be associated tetragonal ZrO_2 and cubic Al_2O_3 crystalline phases. The XRD results of cured ESL glass show the presence of large peaks indicating the presence of crystalline phases probably formed during the high temperature curing (Figure 48). The exact phases associated with the peaks were not identified due to the lack of compositional information on the glass.

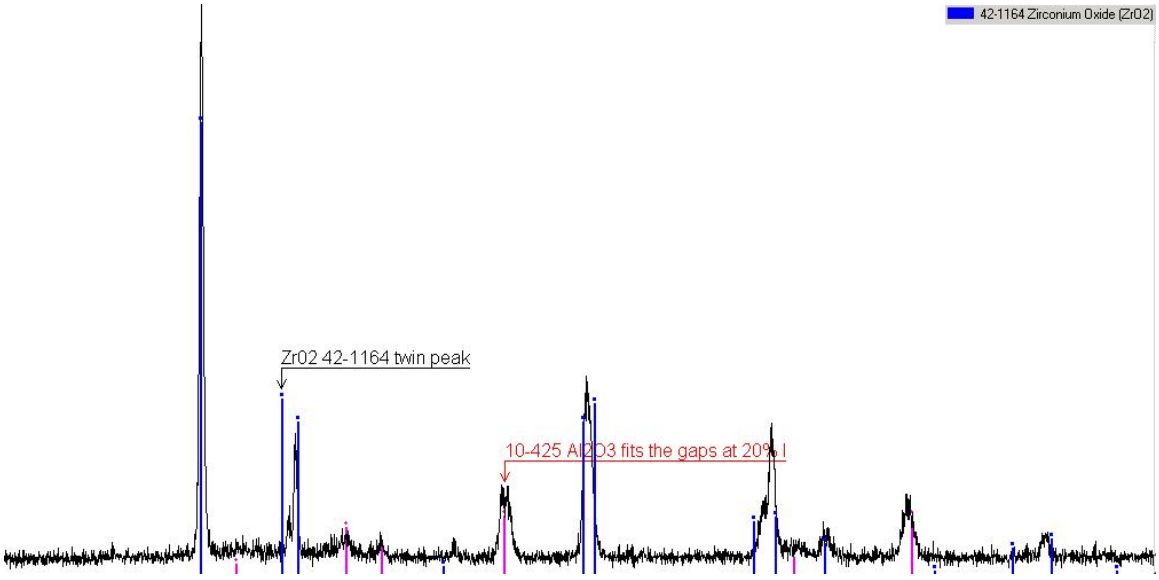

Figure 47 XRD results of ceramic coating, blue bars designate ZrO2 peaks and the pink bars designate Al2O3 peaks

.

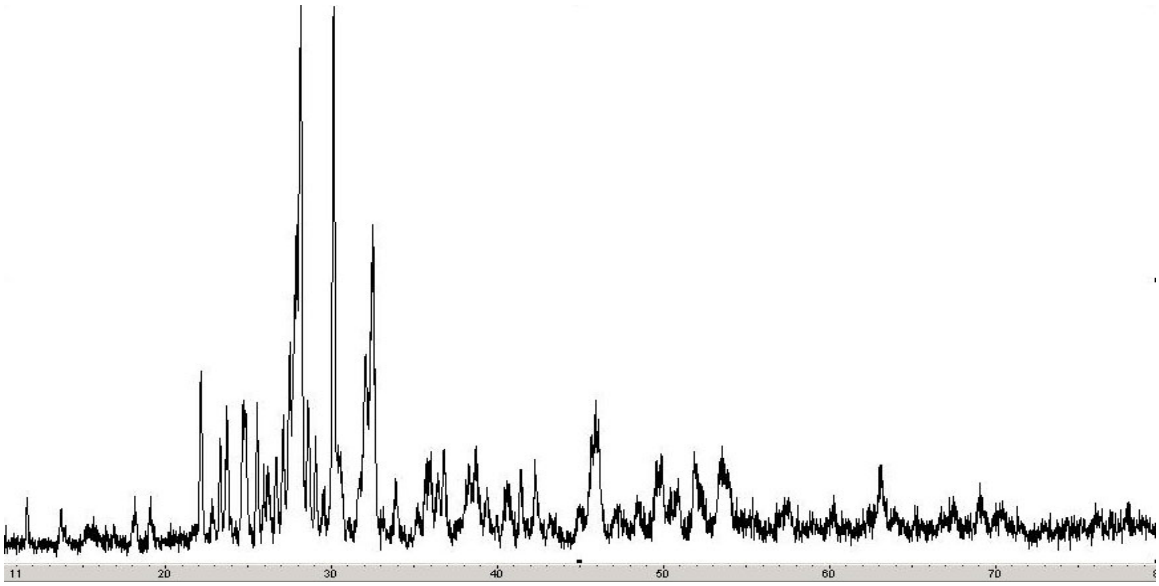

Figure 48 XRD results of cured ESL 4460 glass

The results of dilatometry are shown in Figure 49. The average CTE of ESL 4460 glass from RT to 850°C is about 7E-06 /°C and the average of CTE of AL 453 is about 12.8E-06 /°C. So there is a significant CTE mismatch. In this case the ceramic inter layers helps create a less abrupt transition of CTE from metal to glass. The linear expansion curve also indicates the glass transition temperuatre

(T_g) of the ESL 4460 is around 950°C and the dilatometer softening point (T_d) is around 1030°C.

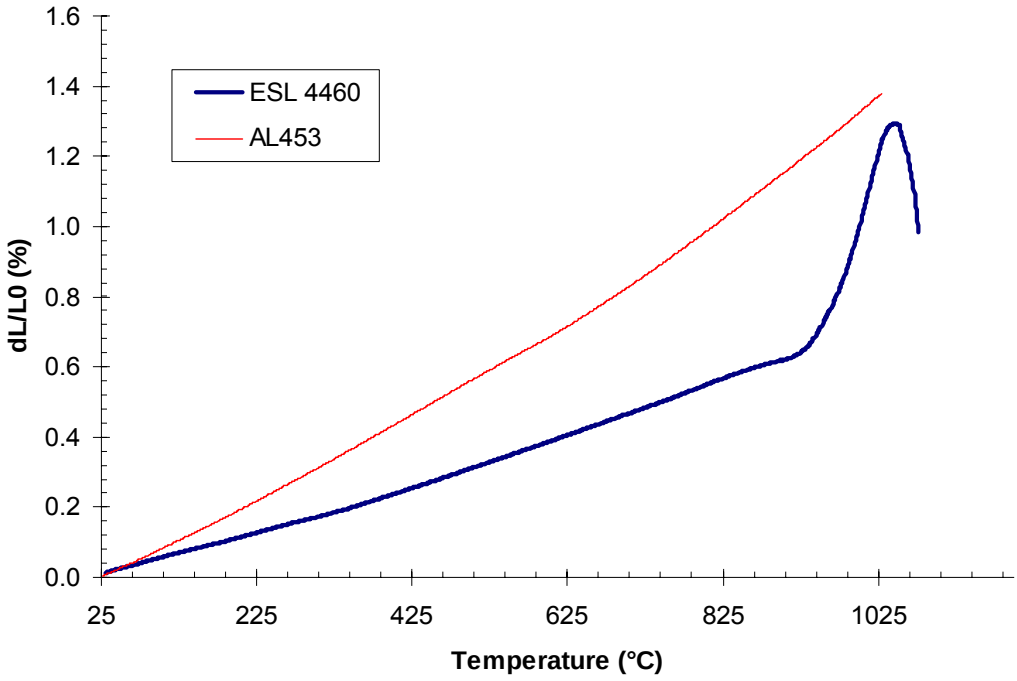

Figure 49 Linear thermal expansion of the glass (ESL 4460) and the stainless steel interconnect material (AL 453). dL—change in length, L0—original length

.

The aged and control samples were sectioned, polished, and mounted for analysis. Scanning electron microscopy (SEM) and electron probe micro-analysis (EPMA) were performed using a Cameca SX50 SEM operated at a voltage of 20 KV. Figure 50 shows the interfacial area of the control (un-aged) sample of the ESL4460-AL453 sandwich without the ceramic interlayer. The interfacial morphology changed notably. Porosity was seen developed in the glass near the interface. From the aluminum element map (Figure 51), the spurious dark regions developed near the interface seem to be the internally oxidized aluminum. The presence of small amount of aluminum in the AL 453 alloy composition (Figure 49) supports this observation.

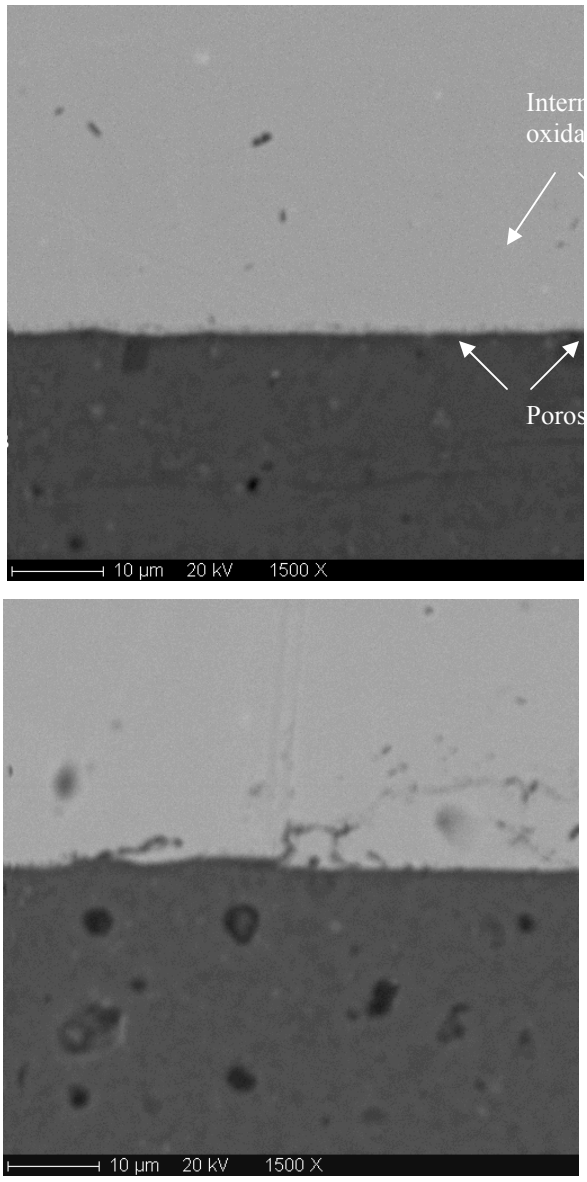

Figure 50. Back scattered electron image of AL453 and ESL 4460 interface before (left) and after aging (right.) Aging was conducted in air at 800C for approximately 186 hours.

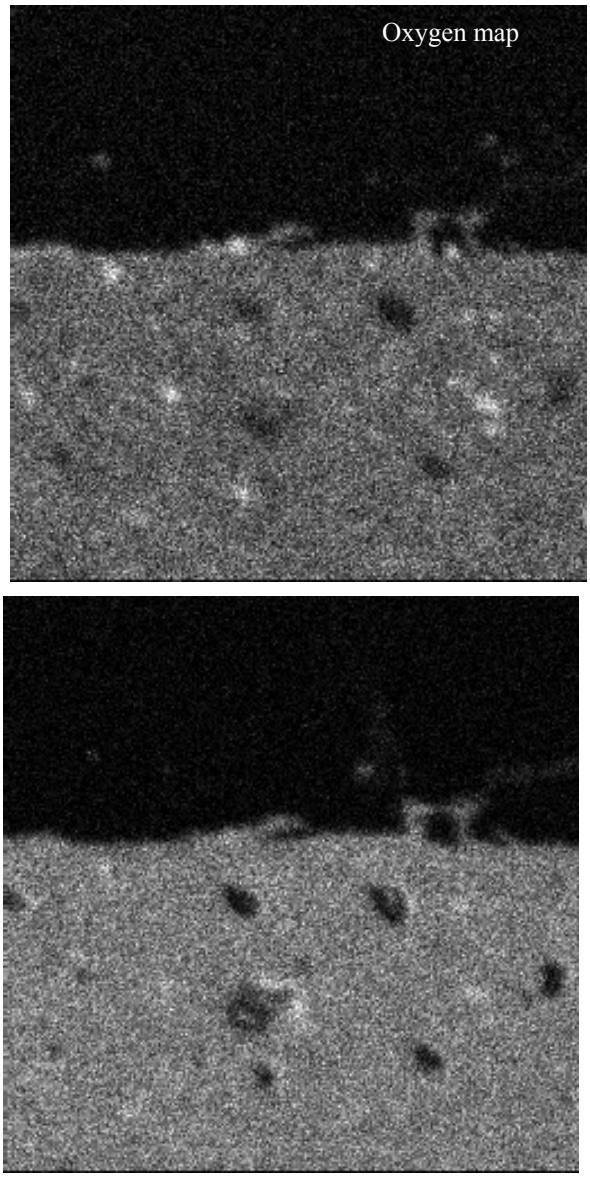

Figure 51 Elemental map of aluminum (left) and oxygen (right) of aged AL 453-ESL 4460 interface region generated with EPMA. The bright spot represent high centration of element Al.

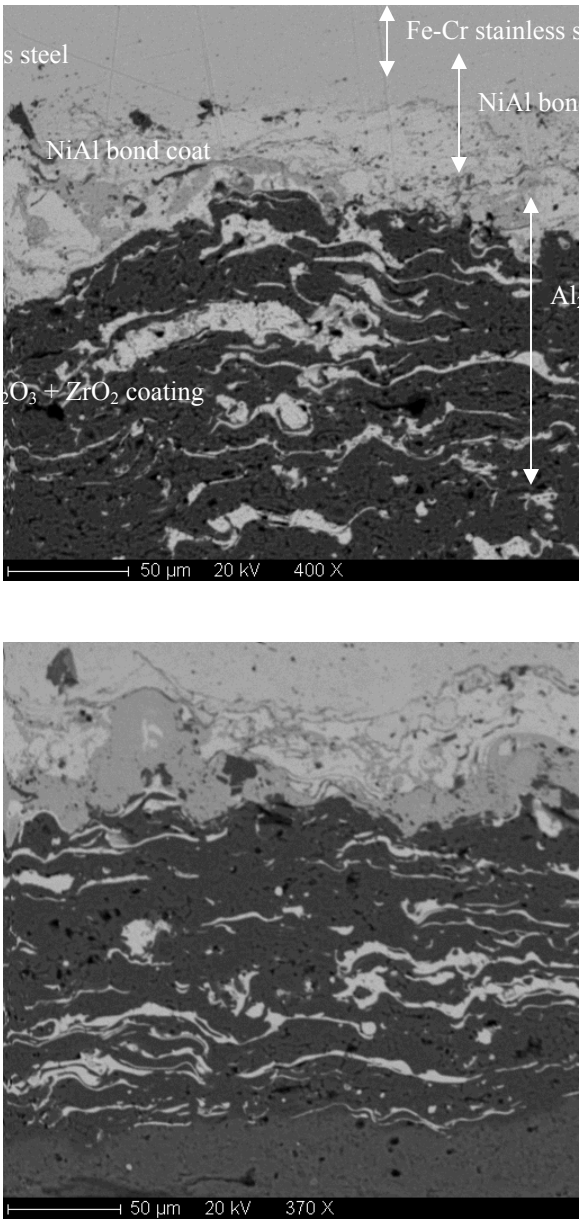

Figure 52 Control (left) and aged (right) sample of stainless steel-ceramic coating-glass sandwiched samples.

Fig 53 shows a sample of AL453 with the ceramic interlayer between the glass and the metal at both interfaces. Preliminary inspection shows uniform adhesion of the glass to the ceramic at the interface. The interface between the ceramic layer and the glass was further examined for signs of interaction between the calcium in the glass and aluminum and the YSZ in the layer. The elemental map of calcium showed little signs of this in the control sample.

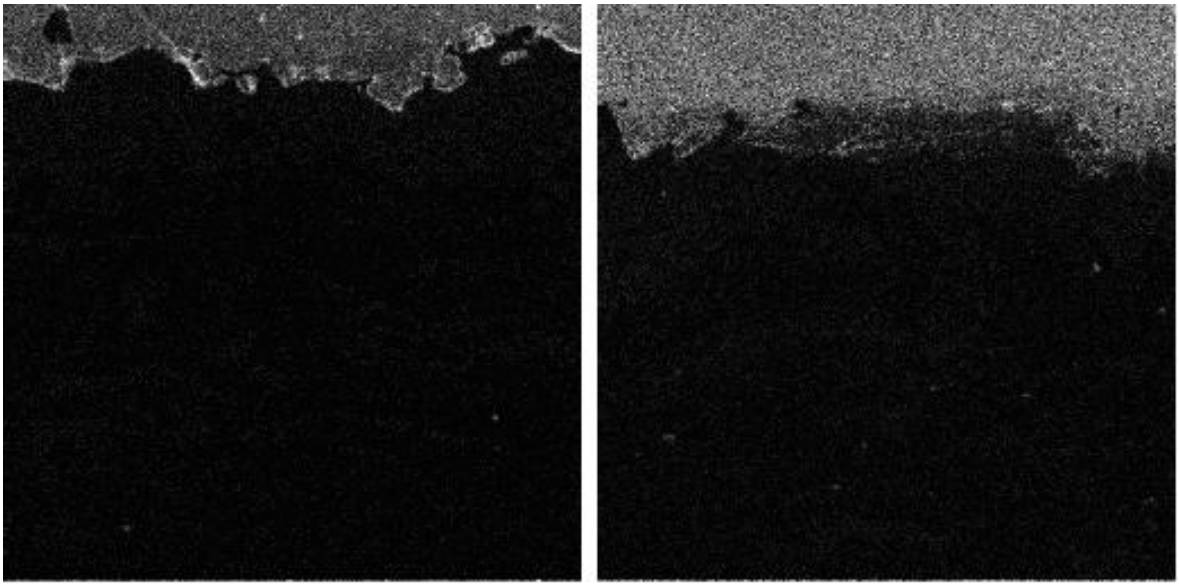

Figure 53 Elemental map of chromium of aged sample (left) and control (right.) After aging, chromium from the stainless steel concentrates at the interface of bond coat and substrate.

Figure 52 shows the interface region of 3-layered control and aged samples. There is little sign of interfacial interaction at the glass-ceramic interface. As one of the most active elements in AL 453 stainless steel, the Cr elemental maps were obtained before and after aging (Figure 53.) The results show that high temperate aging caused chromium to agglomerate at the Al453-bond coat (NiAl) interface. However, no sign of chromium was found in the ceramic and glass layers.

The results obtained in the comparison of the control and aged metal-glass sample suggest that the presence of voids at the interface increased by thermal ageing. This is consistent with a study on comparable materials. For the samples with a ceramic interlayer, high temperature aging causes chromium agglomeration at the bond coat-substrate interface. This is possibly due to chromium diffusion and the formation of chromium oxide. ESL 4460 used in this study is a Ni-free and alkali free aluminosiliate glass from ESL ElectroScience.

Elemental analysis reveals that it contains calcium, aluminum and silicon and almost no barium. XRD analysis shows that it develop crystalline phase after curing. After high temperature aging, no chemical interaction of chromium and glass was identified. The lack of barium is especially significant given that there are many cases in reported literature on the reactivity of barium in the glass with the chromium in the steel to form Barium chromate which precipitates out. This is one of the principal modes of interfacial degradation. The presence of calcium in the glass to replace barium suggests that the glass is less prone to chemical degradation, but it lacks the CTE matching property that the presence of barium gives [23]. In addition, the crystallization kinetics of barium aluminosilicate glasses is reported to be faster than that of corresponding calcium aluminosilicate glasses [24]. Another mechanism that could contribute to the resistance to interfacial interaction is the formation of a scale during heat treatment which is comprised of a top spinel layer of $(Mn,Cr)_3O_4$ and a chromium-rich sub-layer that has been reported for Crofer 22, a ferritic stainless steel similar in composition to AL 453 [25].

Based on the results, it can be concluded that the ceramic layer has certain effect in isolate the chemical interaction of glass and the Fe-Cr stainless steel. However, the relative inertness of the glass (ESL 4460) used resulted a comparison of less contrast. It is unclear how effective the ceramic coating can have provided a glass with high contents of, e.g., alkali oxide, barium oxide, or boric oxide contents. As such, another set of tests were conducted using a more aggressive glass (G18 from PNNL) to probe the effect of refractory ceramic coating in reducing chemical interactions between glass and metal substrates. Crofer22/G18 samples were compared with Crofer22/APS/G18 samples where and APS ceramic coating was displaced in between the Fe-Cr metal substrates and the G18 glass. After aging, SEM and EPMA analysis were conducted. The results are shown in the Figures below.

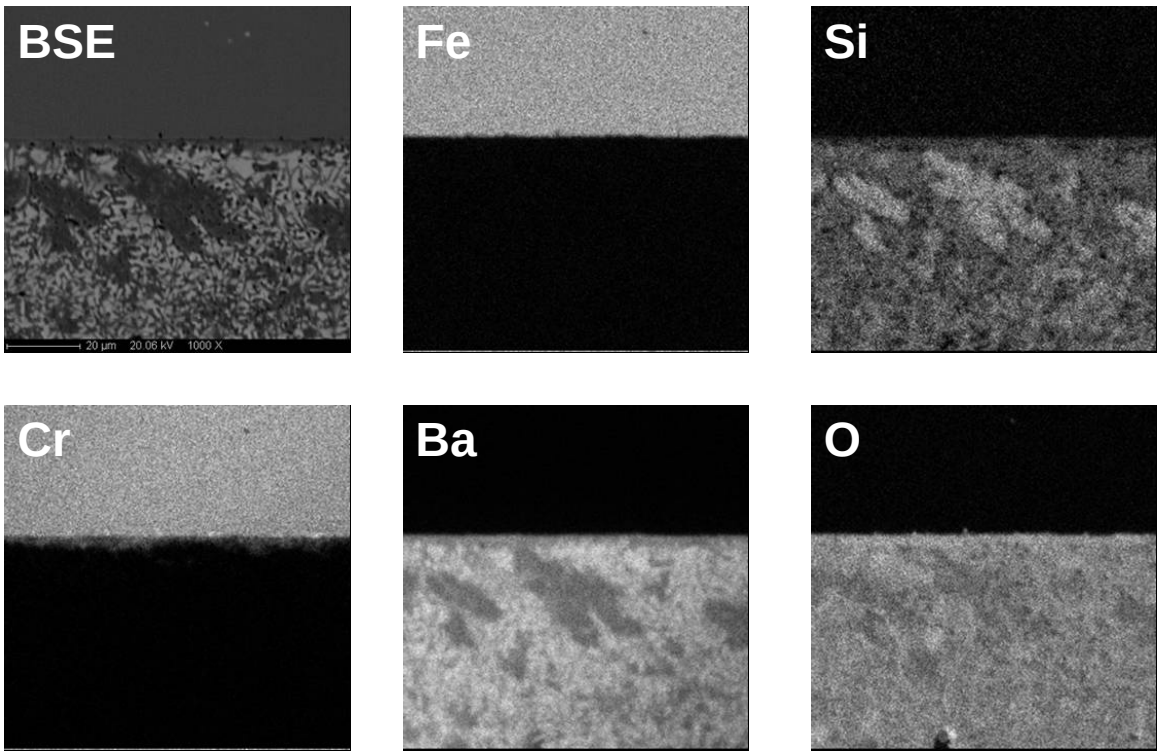

Figure 54. Crofer22/G18 glass sample after aging

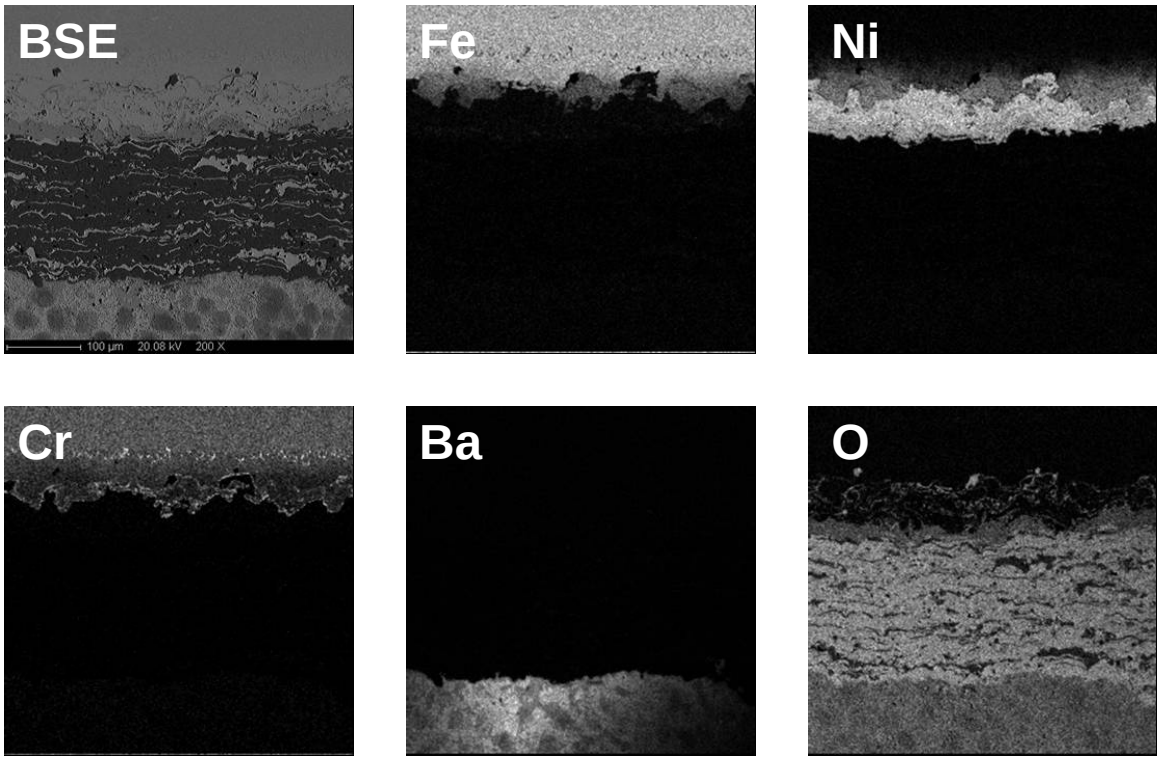

Figure 55. Crofer22/APS/G18 sample after aging

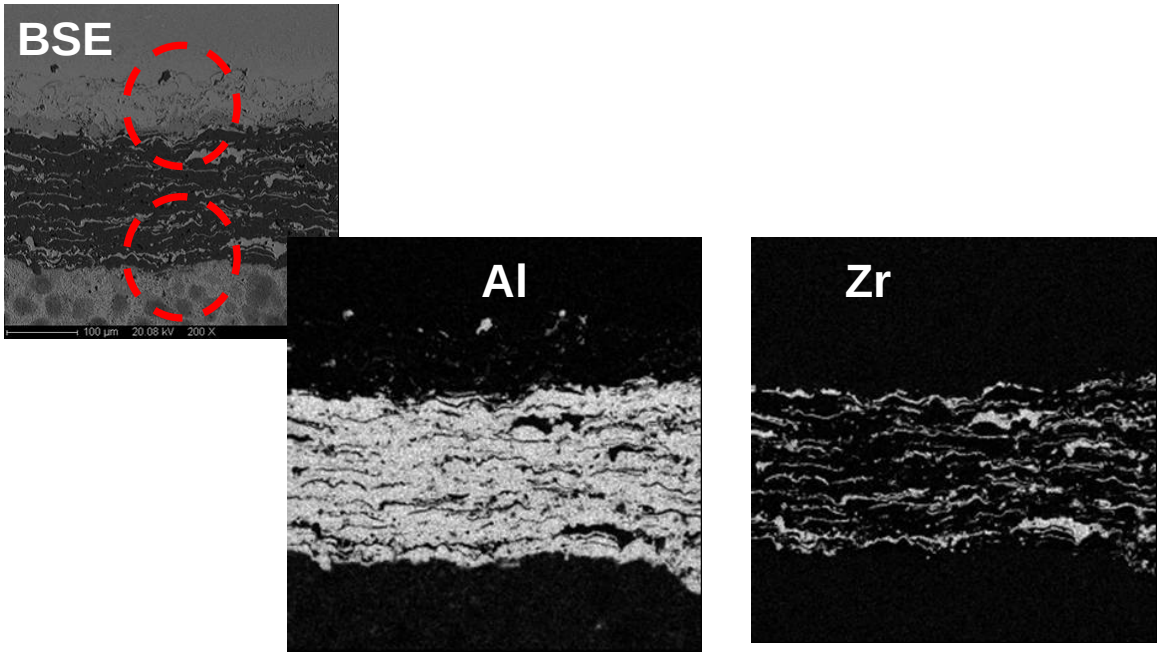

Figure 56. Al and Zr map of aged Crofer22/APS/G18 sample.

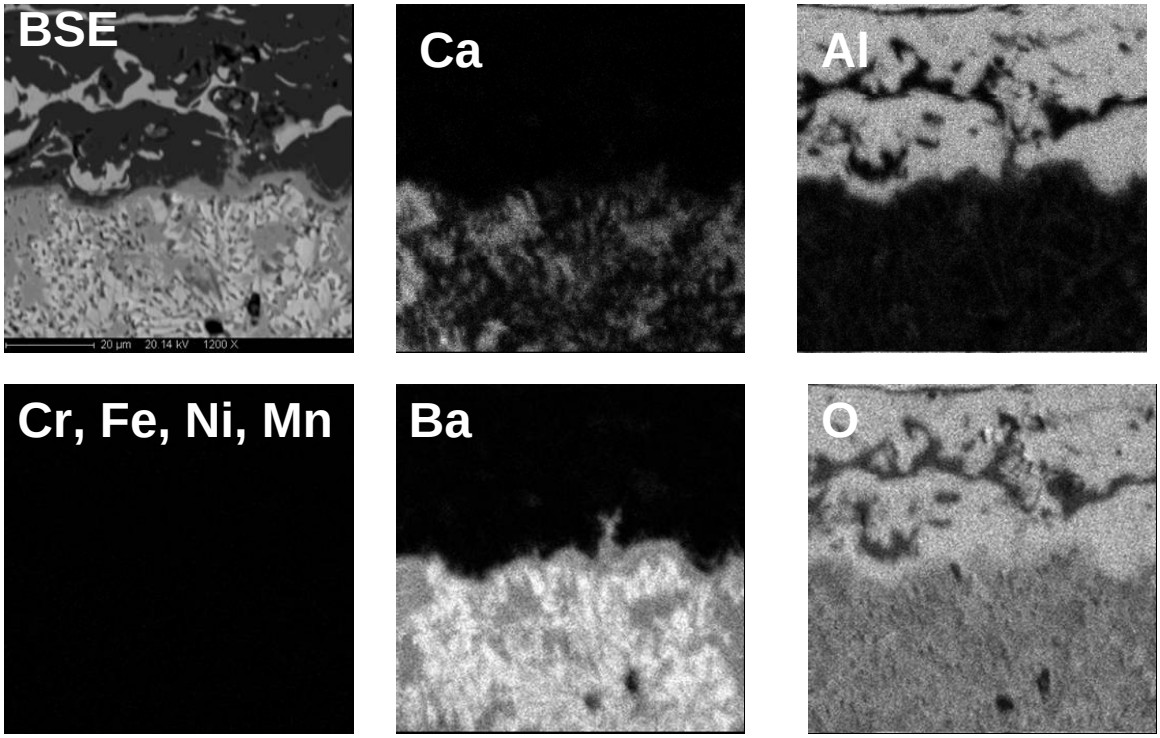

Figure 57. Close up look at the APS/G18 interface after aging.

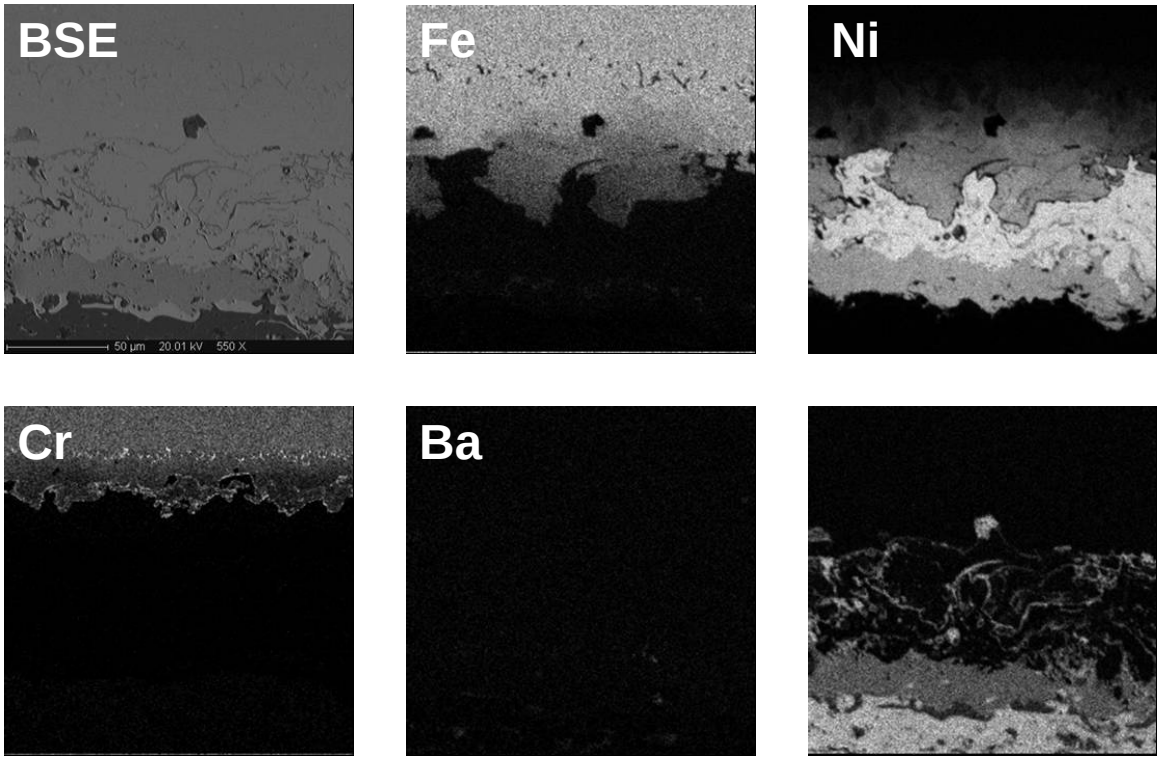

Figure 58. Close up look at the interface between Crofer22/APS after aging

There results clearly showed that APS coating is effective in limiting chemical interaction between active elements in Fe-Cr ally and any reactive ingredients in the sealing glass. Ni based bond coat form inter-diffusion zone with Fe and limit the cross over of Cr and Mn. ZrO2 and Al2O3 topcoat is found compatible with the glass (G18) tested.

6. ACOUSTIC-BASED DIAGNOSTIC METHOD

Methods based on acoustic emission acousto-ultrasound methods were developed to non-destructively evaluate the failure and degradation of the composite seal during thermo-cycling tests.

Acoustic Emission (AE)

ASTM E610-89 “Standard Terminology Relating to Acoustic Emission” defines acoustic emissions as “transient elastic waves generated by the rapid release of energy from localized sources within a material”. Acoustic emissions are used as a means for nondestructive evaluation (NDE) in which a material is given an input stimulus (i.e. applied stress) and energy is released from a source (i.e. crack) in the form of an elastic wave. The elastic wave is then detected by a sensor, typically piezoelectric, where the wave is converted into an electrical signal to be conditioned and analyzed by an AE instrument.

The purpose of using AE testing for SOFC performance evaluation is to capture critical temperatures or temperature differences that cause crack initiation and propagation in the proposed glass composite seal. Statistical cluster classification methods, principal components analysis (PCA) and k-means clustering are utilized to provide a failure mechanism diagnostic tool which can be used to discriminate between friction, non-catastrophic micro-cracking in glass and ceramic, gas leaks and catastrophic running macro-cracks. An AE location sensing test was also done to determine the feasibility of located cracks in a SOFC seal.

Acoustic Emissions (AE) Testing Background: The first users of acoustic emissions for a means of testing may well date back to 6,500 B.C. when artisans making pottery assessed the quality of clay vessels by the audible cracking sounds made while the clay cooled in the kiln. Very early on audible AE was observed in metals undergoing various stimuli. However, the start of today’s technology into acoustic emissions was done by Joseph Kaiser at the

Technische Hochschule Müchen in Germany [26].

AE has been used for many applications similar to the SOFC seal including fatigue cracking, stress cracking, stress corrosion cracking, crack growth in pressure vessels, and gas and liquid leak testing particularly in petroleum industry [26]. C.-K. Lin et al. C. Berndt et al., and Shankar et al. performed AE studies on thermal spray materials similar to those used in the proposed composite seal. These studies have shown that the AE response depends on the porosity, morphology, compositions, bond strength and thermal mismatch between substrate and coating. Additionally, they provided a quantitative assessment of cracking in thermal spray materials using “crack density functions” [27,28,29,30]. Most recently K. Sato et al. monitored the mechanical performance of SOFCs under simulated conditions using AE methods [31]. Apparatus similar to that shown in Figure 59 was used to monitor AE activity in order to detect and identify the fracture process. The AE method was shown to be capable of detecting delamination and vertical cracks within the electrolyte material.

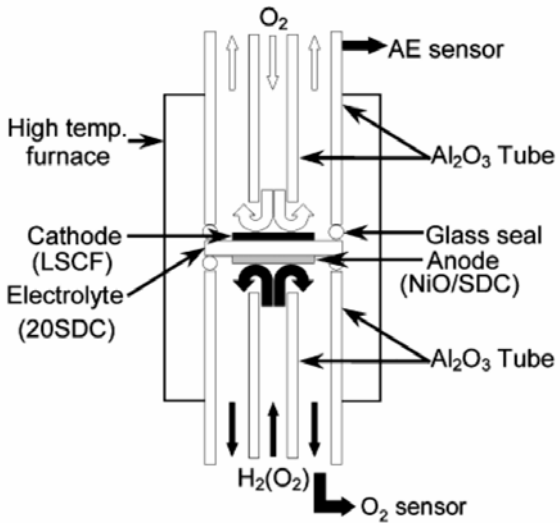

Figure 59 Schematic layout of the use of AE in determining SOFCs performance test apparatus

Automatic classification of AE signals has be used the determine generation mechanisms. These methods use algorithms for automatic clustering and

separation of AE events based on multiple features extracted from the raw experimental data. S. Rippengil et al. used statistical methods and neutral network on reduced data to classify AE data from a box girder system into subsets representing different generation mechanisms [32]. V. Emamian et al. used similar techniques and included a short-time Fourier transform (STFT) to classify signals from a fatigue test of stainless steel 13-8 [33]. G. Manson et al. used principal components analysis to reduce AE data from a box girder system similar to Rippengil et. al. In both cases, four traditional AE parameter rise time, peak amplitude, duration and ring down count were the parameters used for classification. Manson et al., however, also performed k-means clustering and Sammon mapping analysis in order to automatically classify AE signals [34].

AE, PCA and K-means clustering Theory: Acoustic emission (AE) is a nondestructive test (NDT) that involves a stimulus or applied energy sources such as a stress. The primary stimulus in the SOFC seal system case is a thermally induced stress due to differences in coefficients of thermal expansion in the composite material:

$$\sigma = \Delta T(\alpha_1 + \alpha_2) \tag{6.1}$$

Where σ is thermal stress, ΔT is the change in temperature for applied temperature, and α_1 and α_2 are the respective coefficients of thermal expansion. However, stimulus may also be gas movement or other mechanisms. Upon application of stimulus, a release of energy occurs at the sources such as cracking. The release of energy is in the form of an acoustic emissions wave. A sensor detects movement from this wave and converts it into an electrical signal via a piezoelectric effect. A generalization of AE testing system is shown in Figure 60.

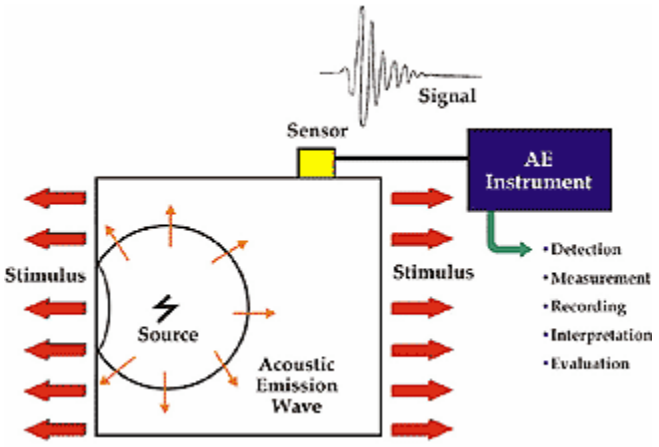

Figure 60 Acoustic emission (AE) basic process

The traditional generalized form of an acoustic signal is shown in Figure 61. For source determination analysis, the four parameters that are used are the peak amplitude, rise time, signal duration and ring down count. The peak amplitude of the signal is generally expressed in decibels by

$$A(dB_{AE}) = 20 \log V_p \qquad (6.2)$$

where V_p is the peak signal in microvolts at the preamplifier input. For the principal components analysis to be discussed later in this section, in order to put all parameters in the same coordinate system, the logarithm for the remaining three AE parameters was taken. Additionally, the data sets were standardized by dividing the mean corrected data by its respective standard deviation.

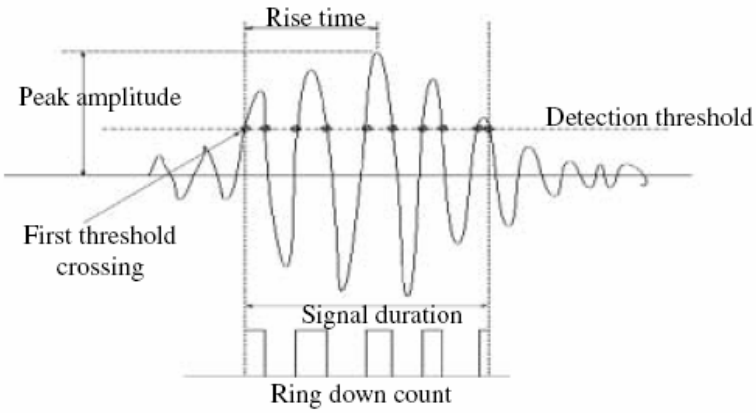

Figure 61 Traditional AE signal

The purpose of principal components analysis (PCA) is to maximize the variance

of a linear combination of the variables. This analysis is done on a single sample of p variables where none of the variables are presupposed to being dependant and no grouping of observations is assumed [35]. Principal components analysis seeks to perform a rotation of axis which the observations are maximally spread out.

The objective is to start with a random vector population, X, which is transformed to a new space, Z, which has the maximum variance. Consider the random vector population as $X = (\vec{x}_1,...,\vec{x}_n)^T$. The sample mean vector, $\overline{X}$, can be obtained by

$$\overline{X} = \frac{1}{n}\sum_{i=1}^{n} x_i = \begin{bmatrix} \overline{x}_1 \\ \overline{x}_2 \\ \vdots \\ \overline{x}_p \end{bmatrix} \tag{6.3}$$

The covariance matrix, S_x, is a matrix of variances and covariances of p variables expressed by

$$S_x = (s_{ij}) = \begin{bmatrix} s_{11} & s_{12} & \cdots & s_{1p} \\ s_{21} & s_{22} & & s_{2p} \\ \vdots & \vdots & & \vdots \\ s_{p1} & s_{p2} & \cdots & s_{pp} \end{bmatrix} \tag{6.4}$$

where the sample variance for the ith variable, s_{ii}, can be calculated by (6.5):

$$s_{ii} = \frac{\sum_{k=1}^{n}(x_{ki} - \overline{x}_i)^2}{(n-1)} \tag{6.5}$$

The sample covariance of the ith and the jth variable, s_{ij}, can then be found using equation (5.4):

$$s_{ij} = \frac{\sum_{k=1}^{n}(x_{ki} - \overline{x}_i)(x_{kj} - \overline{x}_j)}{(n-1)} \tag{6.6}$$

Two variables are considered to have positive covariance, if the variables are related such that the two variables have a tendency towards the same side of the

mean. Conversely, two variables are said to have negative covariance if two variables deviate simultaneously to opposite sides of the mean. If two variables are independent then their covariance will tend towards zero.

The principal components seeks to rotate axis, such that when correlated variables, $\vec{x}_i$ is multiplied by an orthogonal transformation matrix, *A*, a new variable, $\vec{z}_i$ is created. Since A, is orthogonal, $A^T A = I$, the distance to the origin is unchanged:

$$\vec{z}_i{}^T \vec{z}_i = (A\vec{y}_i)^T (A\vec{y}_i) = \vec{y}_i^T A^T A\vec{y}_i = \vec{y}_i^T \vec{y}_i \tag{6.7}$$

The new variables $\vec{z}_1, \vec{z}_2, ..., \vec{z}_p$ are now uncorrelated from matrix proof that if $\vec{z} = A\vec{x}$ then $S_z = AS_x A^T$ where S_z is the transformed covariance matrix and S_x is the sample covariance matrix of X. Thus the new variables $\vec{z}_1, \vec{z}_2, ..., \vec{z}_p$ then form a covariance matrix in the form

$$S_z = AS_x A^T = \begin{bmatrix} s_{z1}^2 & 0 & \cdots & 0 \\ 0 & s_{z2}^2 & & 0 \\ \vdots & \vdots & & \vdots \\ 0 & 0 & \cdots & s_{zp}^2 \end{bmatrix} \tag{6.8}$$

Since S_x is a symmetric matrix, A can be determined by finding the eigenvalues and eigenvectors of S_x. Thus A can be written as

$$A = \begin{bmatrix} \vec{a}_1^T \\ \vec{a}_2^T \\ \vdots \\ \vec{a}_p^T \end{bmatrix} \tag{6.9}$$

where $\vec{a}_i$ is the *i*th normalized (i.e. $\vec{a}_i^T \vec{a}_i = 1$) eigenvector of S_x. The eigenvectors, $\vec{a}_i$ and the corresponding eigenvalues $\lambda_1, \lambda_2, ...\lambda_p$ are solutions of the equation

$$(S_x - \lambda I)\vec{a} = \vec{0} \tag{6.10}$$

where the eigenvalues $\lambda_1, \lambda_2, ...\lambda_p$ of S_x are the variances of the principal components $\vec{z}_1, \vec{z}_2, ...\vec{z}_p$ i.e. $s_{zi}^2 = \lambda_i$. The eigenvalues $\lambda_1, \lambda_2, ...\lambda_p$ are found by determining the solutions to the characteristic equation

$$\left|S_x - \lambda I\right| = \vec{0} \tag{6.11}$$

For principal components analysis, the eigenvector $\vec{a}_1$ should correspond with the largest eigenvalue, λ_1 because it will produce the transformed coefficient z_1 with the maximum variance. All remaining eigenvectors should then be ranked accordingly. In principal components analysis, it is common to weight each *k*th principal components in terms of percent of variance for the *k*th eigenvalue:

$$\text{\% of variance}_k = \frac{\lambda_k}{\sum_{i=1}^{p} \lambda_i} \tag{6.12}$$

For the analysis presented, only the first two principal components are used so that the data may be represented in 2-D form and can be easily visualized.

$$z_{1i} = \vec{a}_1^T \vec{y}_i = a_{11} y_{1i} + a_{12} y_{2i} ... a_{1p} y_{pi} \tag{6.13}$$

$$z_{2i} = \vec{a}_2^T \vec{y}_i = a_{21} y_{1i} + a_{22} y_{2i} ... a_{2p} y_{pi} \tag{6.14}$$

For this case, the cumulative percent of variances of the first two eigenvalues are important such that there is an understanding of how much of the variance (or spread) is determined by the first two components:

$$\text{\% variance 2-D} = \frac{\lambda_1 + \lambda_2}{\sum_{i=1}^{p} \lambda_i} \tag{6.15}$$

Once the original matrix, X, has been mapped into the first two principal components, $\vec{z}_1$ and $\vec{z}_2$, k-means clustering can be performed. The goal of k-means clustering is to divide objects into k clusters such that the centroid of each kth cluster is positioned to minimize the sum of distances to all objects in the assigned to the kth cluster. The amount, k (number of clusters), has to be determined at the onset by the user. Unfortunately, there is no theoretical solution to find the optimum number of clusters for a given data set, instead the

user must make an intuitive estimate relative to the data being analyzed. Sometimes, multiple analysis such be performed to see which on fits best according to a given criteria.

In the case of our analysis, five (5) clusters were chosen as they intuitively fit the AE data presented and visually provided the best fit. The next step in the analysis is to chose starting points for the centroids of the clusters. This may be either done in a randomly or at user defined points. Then each point in the data set is assigned to the group that has the closest centroid. Once every point has been assigned, the centroids for k-clusters are recalculated. This process is repeated until the centroids no longer move. This algorithm seeks to minimize the objective function which measures the distance from a data point and the cluster center. The objective function is a squared error function expressed as

$$J = \sum_{j=1}^{k} \sum_{i=1}^{n} \left\| \vec{z}_i^{(j)} - \vec{c}_j \right\|^2 \tag{6.16}$$

A global optimization method is then used to minimize the metric. In the case of our analysis, the function pca and kmeans is used in MATLAB. Since the optimization within this function can converge on a local minimum, the process should be repeated to ensure that the global minimum is reached. Also, note that since the algorithm uses discrete assignments rather than a set of continuous parameters, the minimum found can not be properly call a local minimum.

Location sensing can be accomplished in different manners. 1-D location sensing was performed as a feasibility check for location sensing for a SOFC application. Location sensing for crack location for a simulated SOFC seal is shown in Figure 62. Event location sensing is performed by the PAC system. As a crack emits AE at the source, the wave travels through the material and AE transducers sense the movement. The time for the wave to travel from the source to the sensor 1 can be determined by

$$t_1 = \frac{x}{v_w} \tag{6.17}$$

where v_w velocity of the wave in the material. The time for the wave to travel to sensor 2 can be found by

$$t_2 = \frac{L - x}{v_w} \tag{6.18}$$

The difference in time is then expressed as

$$\Delta T_{12} = \frac{L - 2x}{v_w} \tag{6.19}$$

Finally the location of the crack front (source), x, can be determined by equation 6.20:

$$x = \frac{L - v_w \Delta T_{12}}{2} \tag{6.20}$$

When calibration is done, the source of the AE is located outside of the sensors and the wave velocity, v_w, can be determined by equation 4.21.

$$v_w = \frac{L}{\Delta T_{12}} \tag{6.21}$$

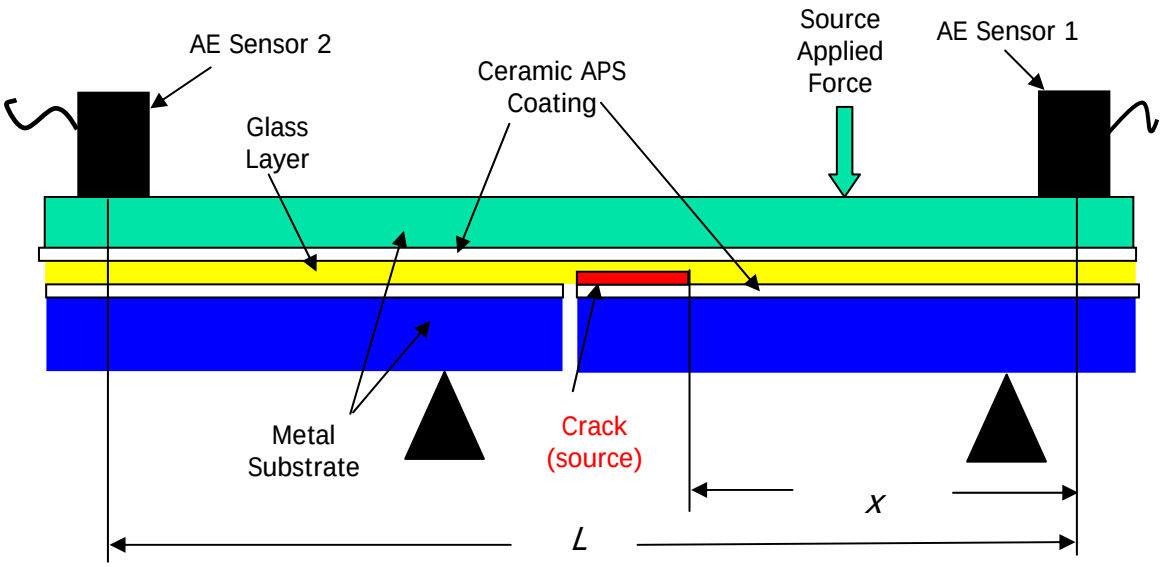

Figure 62 Schematic of 1-D location sensing of simulated cracking using AE methods

Acoustic Emission (AE) Testing Procedure: The focus of the AE testing was done on two glass composite systems, sample #2 (UM #27 glass) and sample # 9 (SNL glass) from
Table **5**. The test rig was setup for continuous leak testing as described in Section 3. Additionally, a wave guide was added to one or both of the pressure tap(s) and the AE sensor was adhered to the wave guide as shown in Figure 63. All the AE data to be presented was obtained using a Physical Acoustics Corp. (PAC) R15 general purpose resonant type sensor with an operation range of 50-200 kHz. A 40 dB gain was applied to the signal using a PAC model 2/4/6 preamplifier. The amplified signal was acquired using the main PAC 60120-2014 rev. 4 PCI board.

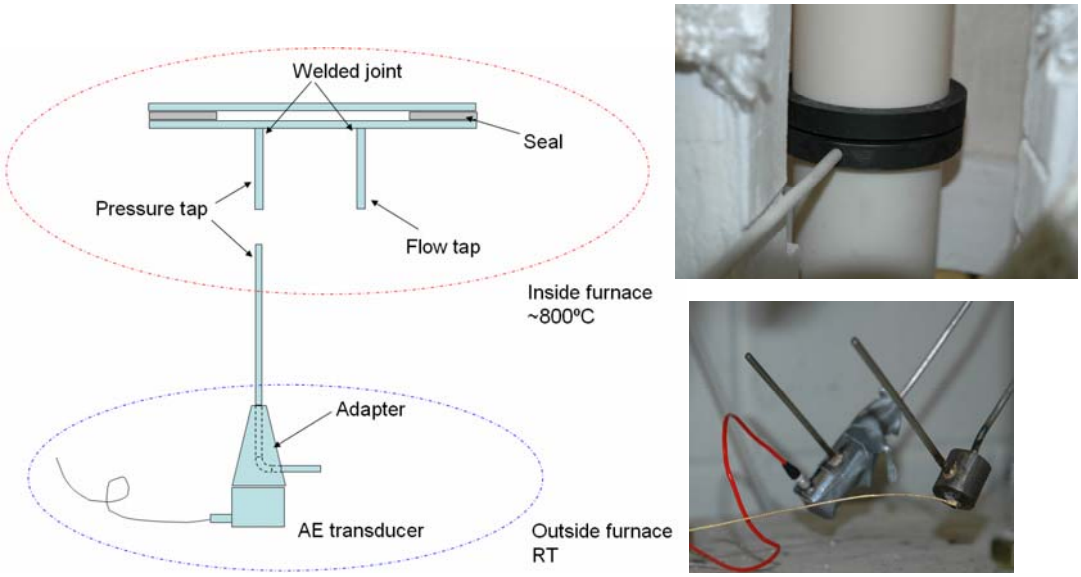

Figure 63 Wave guides and AE sensor attachment

The systems were then thermal cycled according to section 2.5.1 and AE data was collected. Initial data was collected using a 38 dB threshold and 20 kHz – 2 MHz band pass filter. Waveforms were collected for all hits with 100 μs pretrigger and 1000 μs length. After data was collected, further filtering was done to reduce the massive quantity of data. A data filter with a 3 μs minimum rise time and 40 minimum energy level was applied to the data.

For classification analysis, training sets were run. For the first set, a seal system was setup similar to that used during leak testing. The standard ferretic stainless steel sample with the standard APS coating was the main test substrate. For the first sample a glass sealed sample was made using the SNL glass as described by Figure 24. This sample was then manually pulled apart to simulate cracking. For the second training set, a frictional process was simulated by moving the bottom and top test specimens relative to each other. The third sample consisted of simulated mechanical vibration or noise similar to valves opening and closing or other mechanical induced vibrations. The fourth set was made by simulating a gross gas leak. A fifth set of data was collected with the uncoated sample inserted into the furnace and ramped to the operating temperature of 800^{o}C. All these data sets with the exception of the fifth set for reasons to be discussed were combined for cluster analysis. PCA analysis and k-means clustering were performed by a MATLAB computer program. Once the training set was complete, thermal cycle data from the sample #9 (SNL glass) was transformed using the transformation matrix found from PCA analysis of the training set by using MATLAB. The data was then clustered using the k-means clustering routine and the clustered data was compared to the training set. There were several deviations from the leak testing setup that should be noted; the system was not compressed using the air cylinder and all testing was performed at room temperature.

In order to have a training set that better reflects the SOFC thermal cycle leak testing system, a second training set was run that consisted of AE data collected from sample #7 (gold o-ring) from

Table 5 Seal test materials matrix (All APS coatings are 20% YSZ and 80% **Al2O3)**thermal cycle testing. Data was collected in the 200-500^{o}C range since it is known from previous leak test analysis to be the temperature region where cracking occurs. This data was combined with data taken for a glass sample (sample # 9 SNL glass) in the same temperature range. Since glass macro-cracking is thought to be the main failure mechanism of the glass seal, this

training set seeks to discriminate sets of data that are identical with the exception of the filler material. PCA and k-means clustering was performed on this data set and the same thermal cycle data from the first data set was compared in a similar manner to that of the first training set.

The final test that was performed using AE techniques was location analysis. A three point bend test, commonly used for mixed mode flexure (MMF) testing, was setup in a manner similar to that shown in Figure 62 and Figure 64. Three point bend test fixturing was accomplished using Instrom Cat# 2810-400 and #2810-405. The sample in this case were made up of Crofer 22 metal substrate, NiAl bond coat, and Al_2O_3 (80wt%) and a partially stabilized ZrO_2(20wt%) ceramic top coat bonded to opposed specimen of the same composition using ESL 4460 glass. The overall length of the specimen was 8.2 in. (208 mm) with each bottom pieces of equal length of 4.1 in. (104 mm). Cross sectional dimensions of the substrates were .078 in. (2.0 mm) by 0.50 in. (12.7 mm). Sensors were approximately equidistant from the ends and were 6.65 in. (168.9 mm) apart. The bottom fulcrums were placed 3.93 in. (100 mm) apart with the fulcrum closest to sensor 2 placed 0.01 in. (2.5 mm) from the crack initiation position (approximately the mid-point). The top fulcrum applied load 0.01 in. (2.5 mm) to the left of the fulcrum closest to sensor 2. Load was applied to the MMF setup using an Instrom 5866 load frame controlled by Instrom Merlin software.
Prior to location sensing, the wave velocity through the specimen had to be determined. This was accomplished using pencil lead breaks (commonly used in AE testing) outside of the sensors i.e. to the right of sensor 1 or left of sensor 2. Ten tests were done. The high and low were thrown out and the average ΔT was determined. Then using Equation 6.21 wave velocity, v_w, was determined to be 216,612 in/s. This value was then used throughout the 1-D location sensing testing. 1-D testing then was taken at four different time intervals.

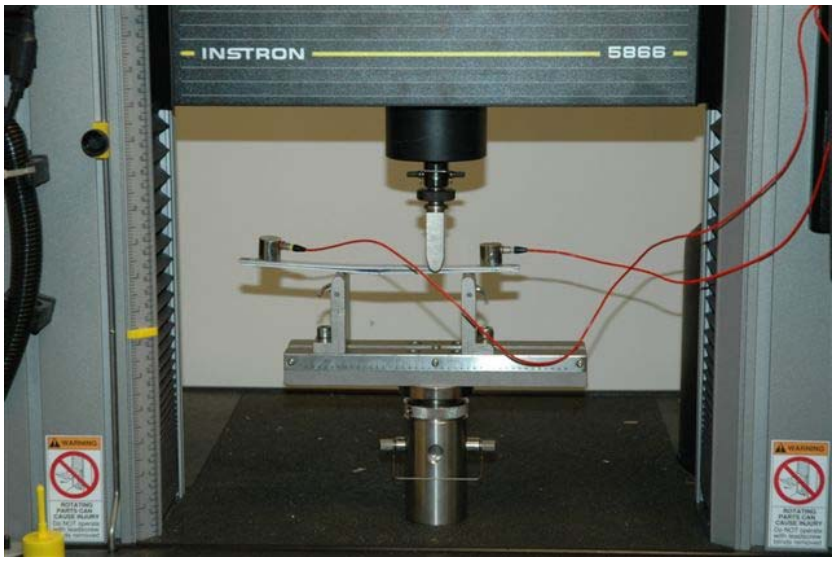

Figure 64 1-D location determination using AE methods

Acoustic Emission (AE) Testing Results and Discussion: Time, temperature, leak rate, gas pressure and AE data were taken simultaneously during the first cycle of sample #2 thermal cycle testing as shown in Figure 65. There is an obvious trend that as the leak rate increases the AE activity increases. One or two minutes prior to full failure of the seal there is a large increase in the amount of hits indicating there was likely some large mechanical failure either from macro-cracking or movement at the seal. Post test analysis, presented in Section 3, confirms that there was likely cracking and slippage of the seal (Figure 28). Following failure of the seal the AE continued, however at a lower amplitude and activity level. Frictional sources from continued movement at the seal due to slippage or CTE mismatch are the likely cause for this emission.

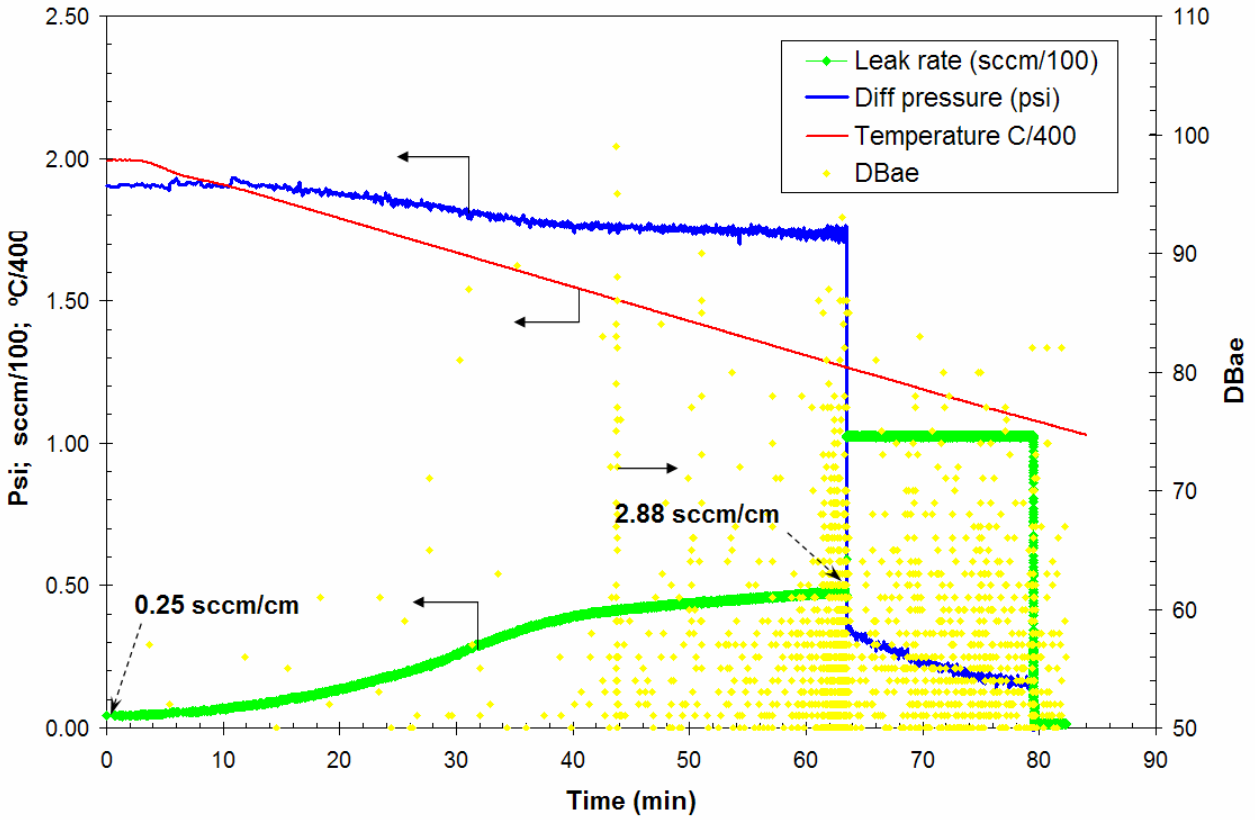

Figure 65 Sample 2 UMR#27 glass AE during thermal cycle

A similar analysis was completed during sample #9 thermal cycling (***Figure 66***). The 2nd thermal cycle was taken as a representative set. Again, there was an obvious trend that as temperature decreased from the operating temperature, in this case 700°C, the seal began to fail and the leak rate increased as did the AE activity. However, with this thermal cycle data, there are some aspects that indicate the need for further data analysis. First, as the temperature increased from 400°C to the operating temperature, there was significant amount of AE, yet the leak rate was decreasing indicating that the seal was being formed. This AE is likely due to frictional noises of seal materials moving relative to one another due to CTE mismatch but could also indicated glass transition. Secondly, after failure of the seal, AE continued likely due to frictional sources or gas leaking. In any case, it is important to be able to isolate AE data into different mechanical modes.

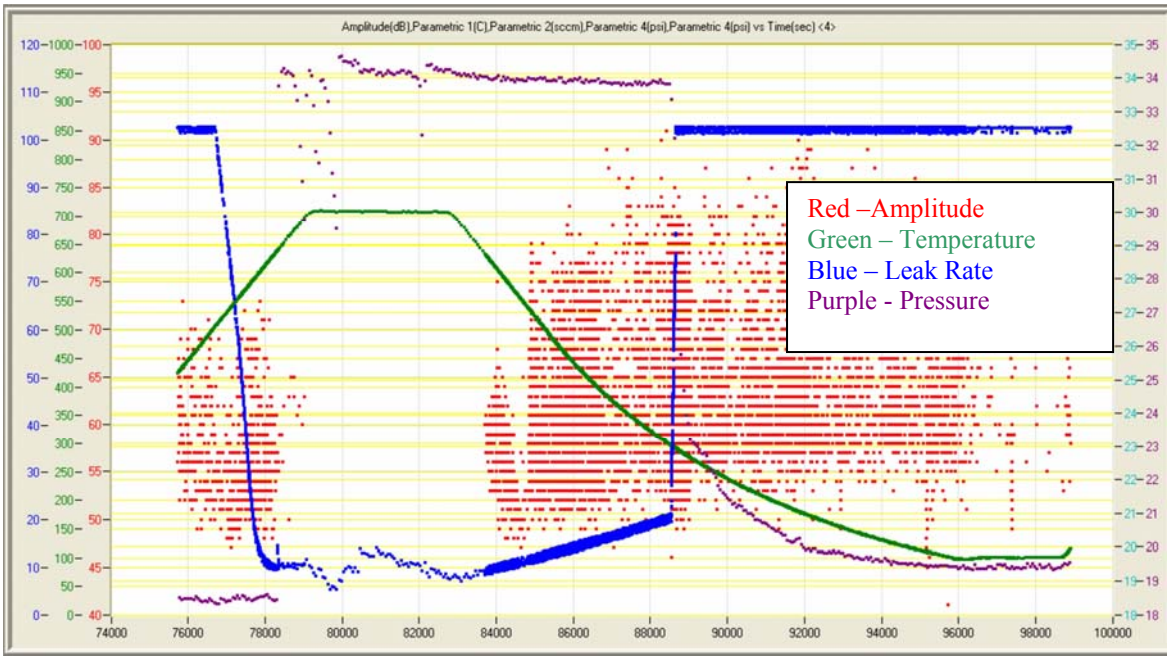

Figure 66 Sample 9 SNL glass 2nd thermal cycle AE activity screen

In most instances for glass SOFC seal applications, the most important mode is the running cracks at the seal causing catastrophic fracture failure. AE data other than this is less important, however, there may be other AE sources that are important to discriminate between i.e. gas leaks, mechanical noises, friction noise, crystal grain growth, corrosion, etc. Therefore, classification techniques were used to help discriminated between sources.

The PCA and K-means clustering techniques were employed (Figure 67). In the first analysis, AE was simulated for cracks, frictional noises, gas leaks, mechanical noises and thermal induced AE for a bare substrate. One of the concerns with the thermal induced AE was corrosion scaling, however, there were only two (2) AE hits found while the bare substrate was thermal cycled so this source was considered negligible and was eliminated from the analysis. As shown in Figure 67, the first two principal components accounted for 78.6% of the variance and the transformation matrix, A, was found to be used later in thermal cycle AE classification.

Five (5) clusters were found to best represent the simulated AE data. Sample waveforms for each cluster are shown in Figure 68Figure 72. Note that the maximum sample time for capturing a waveform was 1000 μs so duration and ring down count effects are not accurately shown. Mechanical noises were mostly grouped into cluster 1 which was dominated by high amplitude; low rise time AE signals (

Table 14, Table 15). Gas leaks, which typically have long duration signals, were grouped predominately in cluster 2.

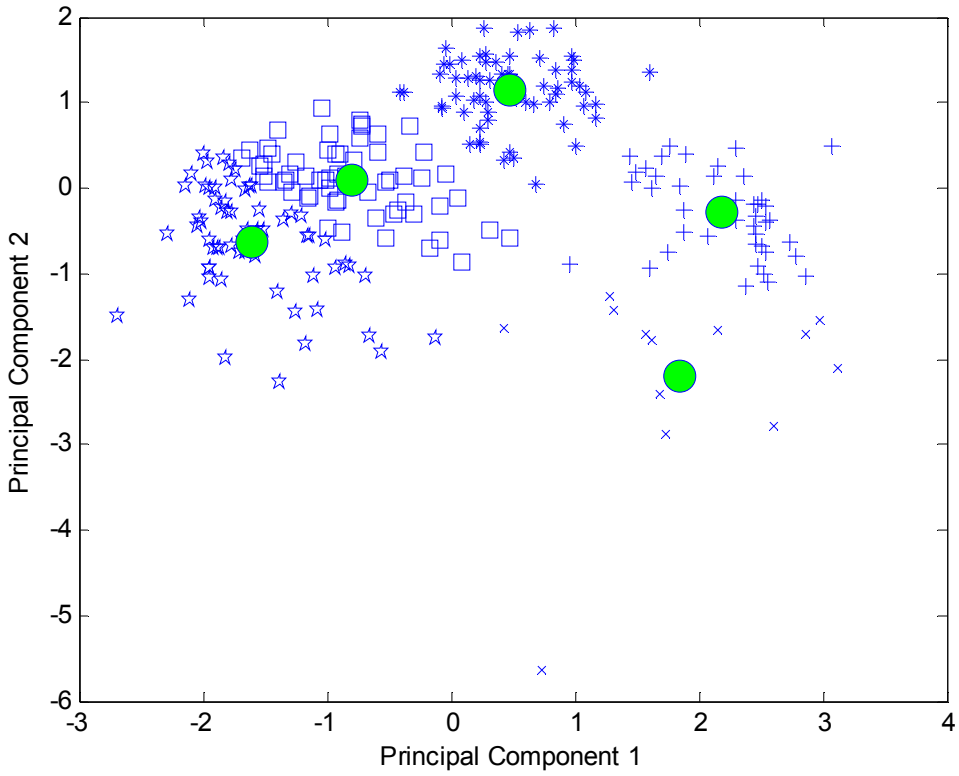

Centroids =

0.4714	1.1448
2.1788	-0.2885
1.8523	-2.1963
-0.7953	0.1014
-1.5982	-0.6276

A=

-0.2509	0.6886	0.6803	0.0016
-0.6687	-0.0441	-0.2003	-0.7147
-0.6536	0.0573	-0.3007	0.6922
-0.2505	-0.7215	0.6377	0.1002

PC #	Variance	
1	2.1352	53.38 %
2	1.0132	25.33 %
3	0.8322	20.80 %
4	0.0195	0.49 %

Figure 67 K-means clustering for simulated AE seal failure mechanism

Frictional noises and cracking data were more difficult to discriminate between as both signals are grouped predominately in clusters 4 and 5. AE activity taken during simulated cracking can actually consist of several potential types of AE sources; micro-cracking of glass and APS topcoat, frictional noises and running cracks or macro-cracks. Macro-crack generally initiate from propagation of non-

catastrophic micro-cracks which run together resulting in unstable crack growth and lead to catastrophic fracture. The micro-cracks release low amounts of energy resulting in lower amplitude AE signal than macro-cracks. Additionally, as micro-cracking occurs there may be some subsequent small movements in the material causing more low level emission. Consequently, macro-cracks release large amounts of energy hence large amplitude, long duration AE signals and are generally coupled with many low-level AE signals. Therefore, one can assume that micro-cracking and frictional noises are the AE sources for clusters 4 and 5 and the macro-cracks result in AE that is grouped into cluster 1. Although cluster 1 has only 5 hits from the crack simulation, it has AE features which are indicative of unstable cracking including low rise time, moderate duration and high amplitude. This also suggests some limitations of PCA /k-means clustering analysis. High frequency of hits in one cluster may not in itself indicate a particular mode. Instead, observations in several clusters should be considered. As an example, if you just considered cluster 1 without cluster 4 or 5, a mechanically induced noise could be misclassified as being macro-cracking and vice-versa.

Table 14 Cluster classification for simulated AE

		Simulated AE				
		1	2	3	4	5
	friction	1	0	3	22	17
	mechanical	58	1	1	14	10
	gas leak	1	40	9	3	1
	crack	5	2	0	21	34
				Cluster Number		
		1	2	3	4	5
Condition	friction	2.3%	0.0%	7.0%	51.2%	39.5%
	mechanical	69.0%	1.2%	1.2%	16.7%	11.9%
	gas leak	1.9%	74.1%	16.7%	5.6%	1.9%
	crack	8.1%	3.2%	0.0%	33.9%	54.8%

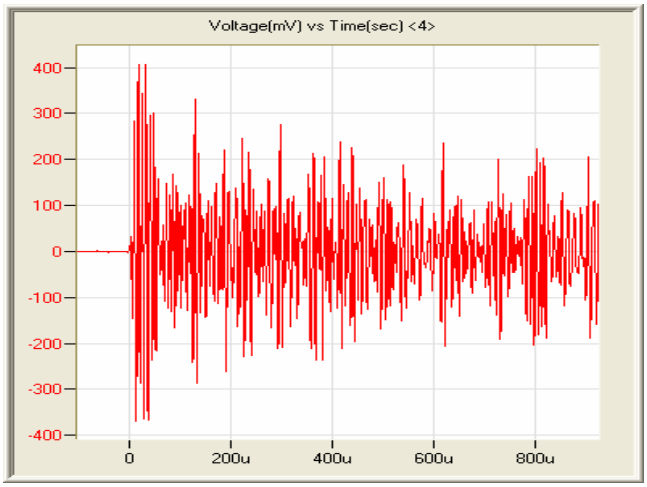

Figure 68 Cluster 1 waveform

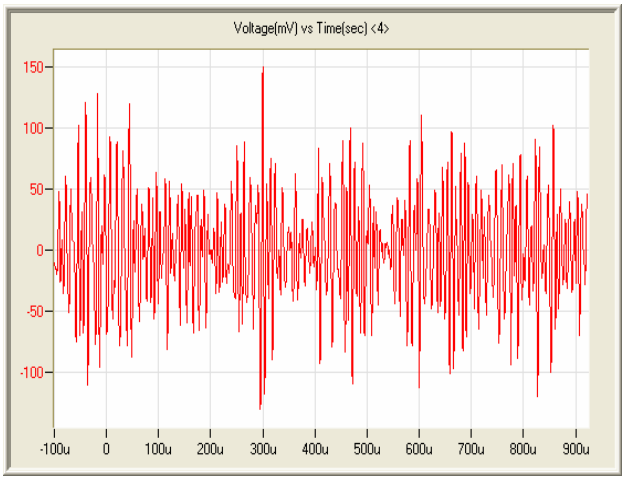

Figure 69 Cluster 2 waveform

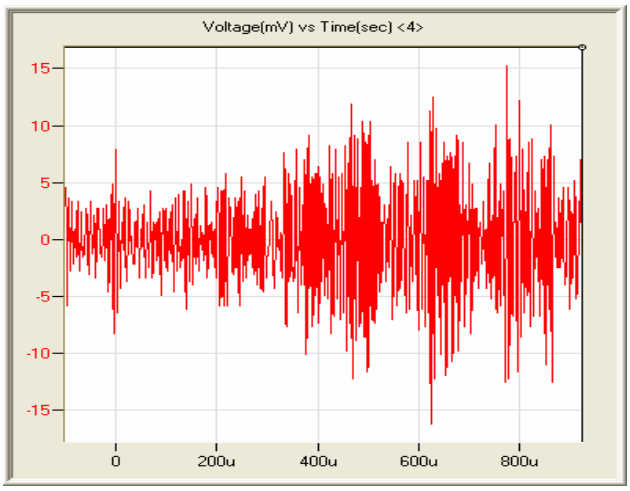

Figure 70 Cluster 3 waveform

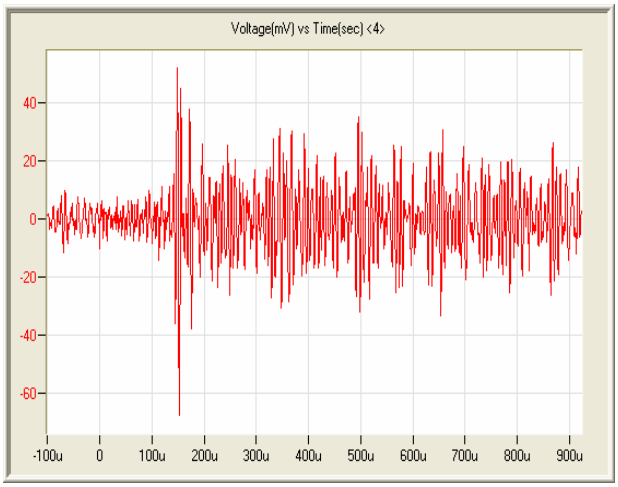

Figure 71 Cluster 4 waveform

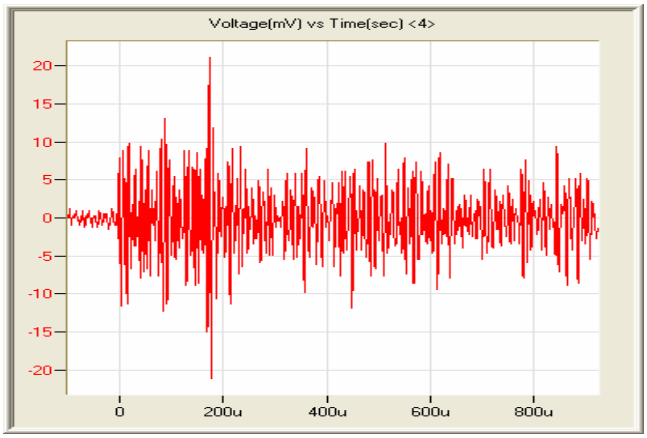

Figure 72 Cluster 5 waveform

Table 15 Average trend by cluster number for simulated AE training set

	Averages			
Cluster	rise	count	duration	amplitude
1	198.4	3799.6	37707.9	90.2
2	337.3	36796.9	652635.0	68.3
3	983.6	20331.5	408760.2	61.4
4	175.0	1195.1	15992.9	67.9
5	264.7	415.5	6175.1	59.3

After the training matrix was completed, the PCA transformation matrix was used to map data from the 2nd thermal cycle of the sample 9 (SNL glass) testing and k-means clustering was performed. In order to make computation easier and clustering more visible, the entire data set was reduced by taking every 50th AE hit. One should note that the results are not principal components only results from actual thermal cycle testing that are transformed to the same axis as the principal components of the simulated AE training set. The results of this analysis are shown in Figure 73. Since, the most interest is with Cluster 1 data, a time histogram was overlaid with time, temperature and leak rate data from the thermal cycle (Figure 74). There is a clear trend indicating that AE associated with detrimental cracking is the primary cause for seal failure.

The first simulated AE test was done primarily at room temperature and was also not subject to the same compressive stress as are actual seals. These

differences may lead to potential mischaracterization of AE data. In fact, by observing the simulated AE data cluster in Figure 67 to that shown for the seal during thermal cycling in Figure 73, there is an obvious shift of cluster centroids indicating that there is some difference. Even with these differences, cluster 1 data for this set provided useful trending.

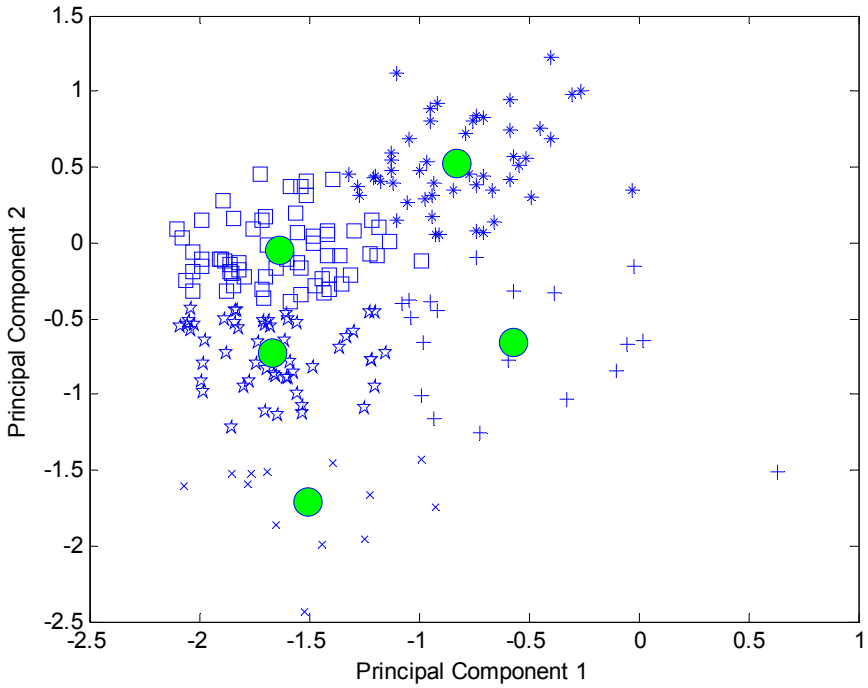

Figure 73 K-Means clustering for reduced AE data of thermal cycle 2 – sample 9 (SNL glass) using simulated AE training set

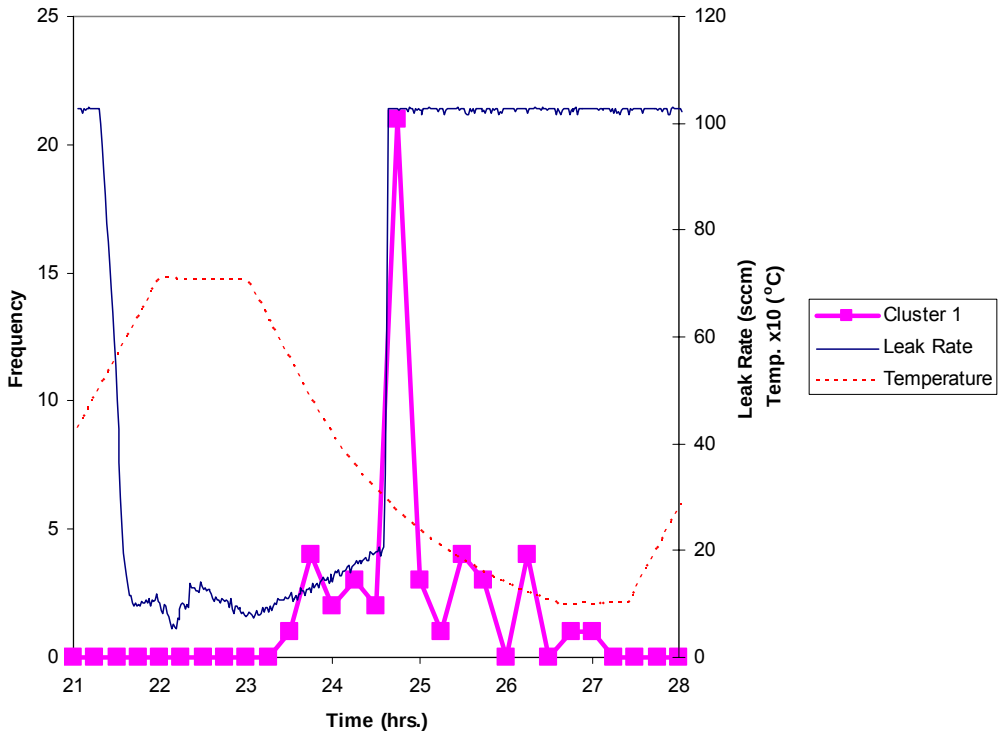

Figure 74 Cluster 1 of sample 9 thermal cycle test using simulated AE PCA transformation matrix

In order to better characterize the signal differences between frictional, micro-cracking and macro-cracking, a second learning set was made. For this analysis, AE from thermal cycling of a gold o-ring seal and glass seal were combined and PCA and k-means cluster analysis were performed. The concept behind this configuration was that the gold o-ring sample will not produce the running cracks like the glass seal. There may be some non-catastrophic cracking in the top coat but not the larger amplitude cracking seen by the glass cracking. However, in all other aspects the seal configuration was identical so analysis should be capable of discriminating between detrimental cracking and all other AE sources.

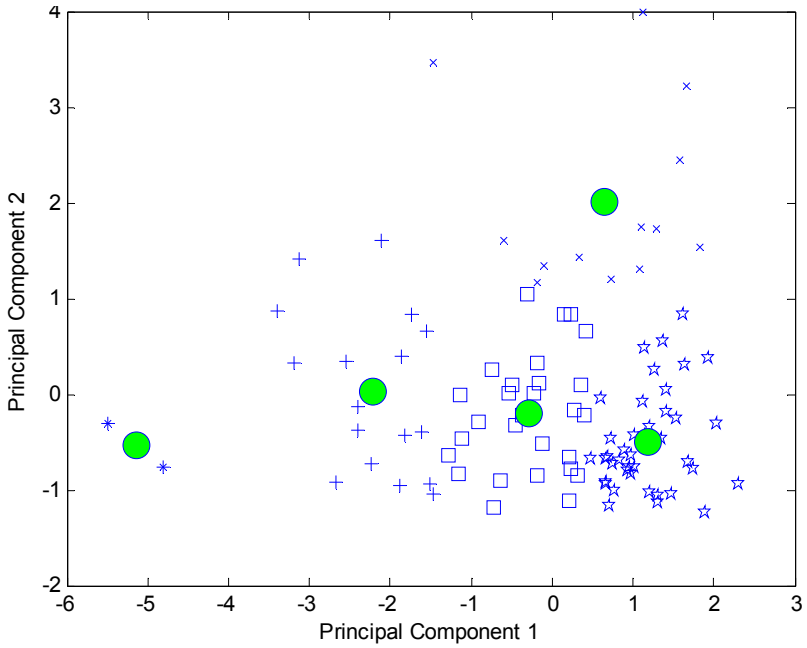

Centroids =		A =				variance		
-5.1487	-0.5403	-0.0231	-0.9258	0.3769	0.0146	2.3527	58.8163	%
-2.2096	0.0309	0.6273	-0.1112	-0.2058	-0.7428	1.0837	27.0932	%
0.6431	2.0157	0.5988	-0.1796	-0.4296	0.6516	0.4911	12.2775	%
-0.2836	-0.2054	0.4974	0.3134	0.7944	0.1531	0.0725	1.813	%
1.1860	-0.4974							

Figure 75 K-Means clustering for o-ring versus glass training set

Table 16 O-ring versus glass AE K-means clustering analysis classification summary

	Cluster Number				
	1	2	3	4	5
Glass	2	11	3	14	20
O-ring	0	6	10	14	20

Figure 75 demonstrates the clustering and Table 16 gives the breakdown by cluster. Both cluster 1 and cluster 2 are dominated by AE from the glass seal. Cluster 3 is largely dominated by gold o-ring AE data. Clusters 4 and 5 actually have identical counts indicating no difference in mechanisms that cause this type of AE. Although, it is inconclusive from this data, these clusters are likely dominated either by frictional noises or micro-cracking in the ceramic top coat. Table 17 shows the average trend for each cluster. Cluster 1 has a short rise

time, long duration and large amplitude which are representative of running cracks. Cluster 2 while it has a slightly longer rise time, it also has relatively high amplitude and duration. This information coupled with the Table 17 trends suggests that this cluster is dominated by cracking either micro- or macro- at the glass interface. Cluster 3 has characteristics more indicative of frictional noises i.e. long rise time and lower amplitude.

Table 17 Average trend by cluster number for o-ring versus glass training set

Average

cluster	rise	count	duration	amplitude
1	94.0	1535.5	22076.0	83.0
2	210.5	806.4	10943.4	68.5
3	590.3	417.9	6758.1	53.8
4	173.6	461.6	6929.2	62.0
5	127.7	302.4	4781.3	57.8

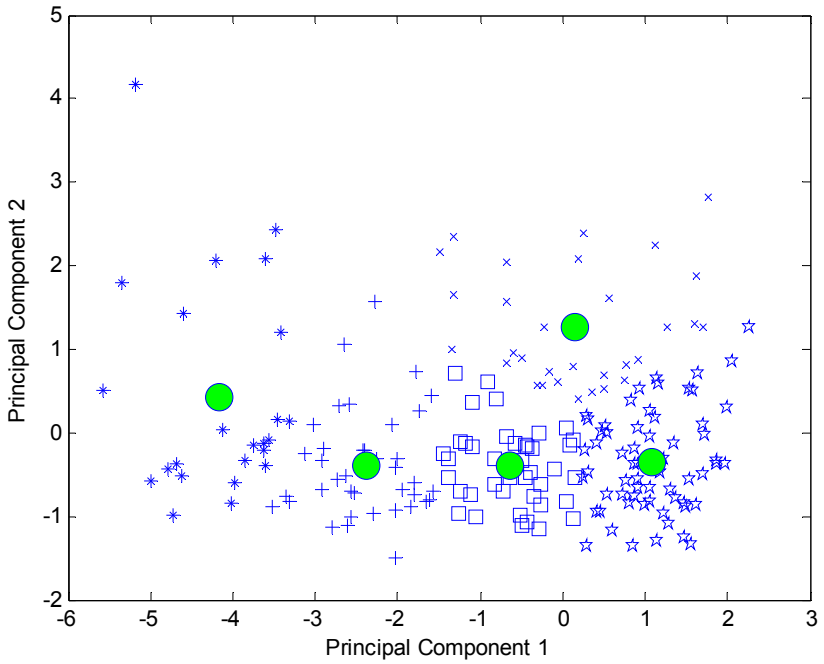

Figure 76 K-Means clustering for reduced AE data of thermal cycle 2 – sample 9 (SNL glass) using gold o-ring/glass training set

AE taken during thermal cycling of sample 9 (SNL glass) was mapped to the principal components axis of the combined o-ring and glass training set (Figure 76) Overlaid frequency histograms with process parameters were plotted for clusters 1,2, and 3 as shown in Figure 77 and Figure 79. Both 1 and 2 show a cracking trend that follows the leak rate data indicating that cracking was the main mode of failure of the seal. Interesting, cluster 2 actually shows a better trend than cluster 1. There is no obvious reason for this behavior, however, by observing the plot shown in Figure 76, the PCA transformation matrix, A, in Figure 75, and the raw data, there is evidence that the data grouped into cluster 1 was misclassified. Data that was greater than zero in the second principal component has a long rise time which is more likely to be frictional noise instead of cracking. Data classified in cluster 3, follows trending more likely to be frictional noise as cluster 3 AE hits are found more during resealing and also while there was little change in leak rate during cooling. One should also note that there will likely be an increase in frictional noise during cracking as the constraints on the materials are decreased and the materials are freer to move relative to one another.

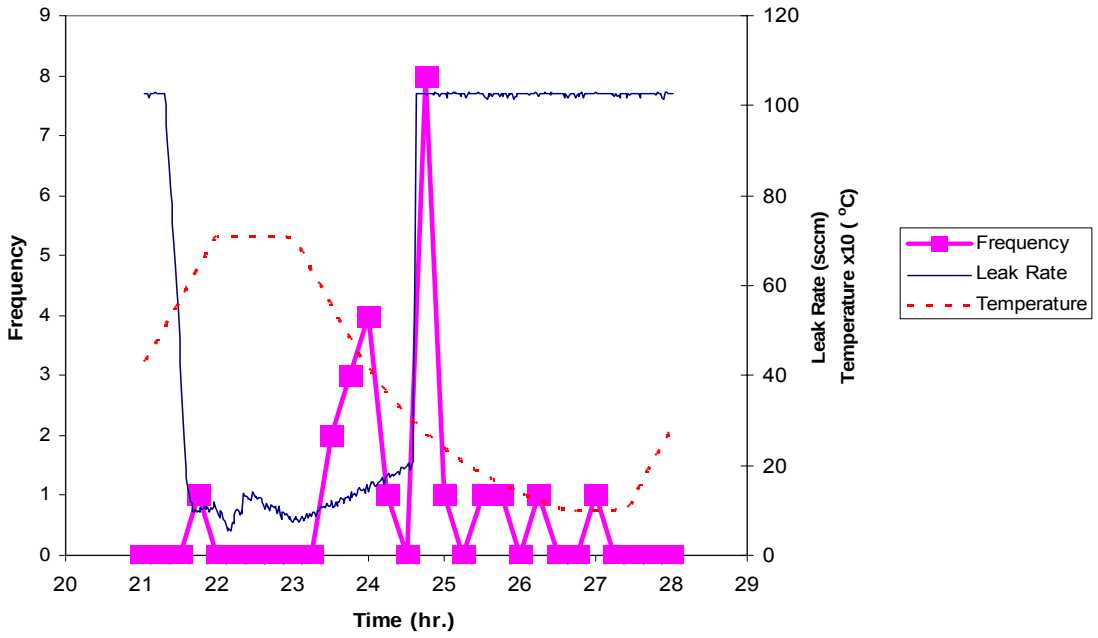

Figure 77 Cluster 1 of sample 9 thermal cycle test using O-ring versus glass PCA transformation matrix

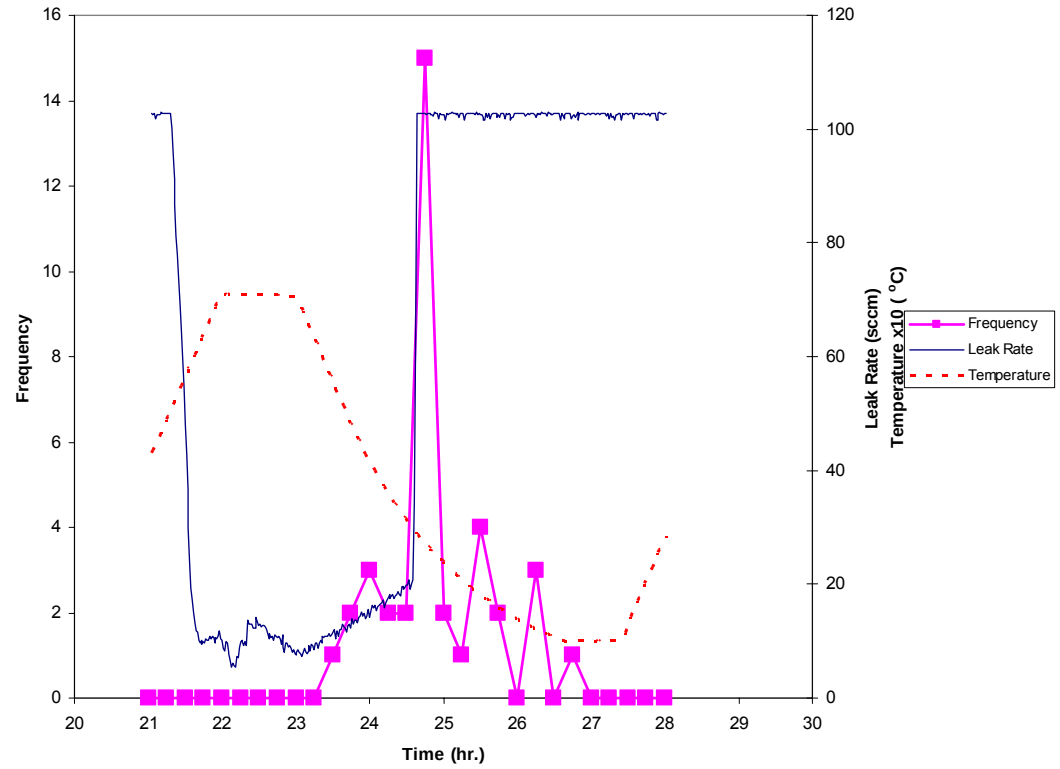

Figure 78 Cluster 2 of sample 9 thermal cycle test using O-ring versus glass PCA transformation matrix

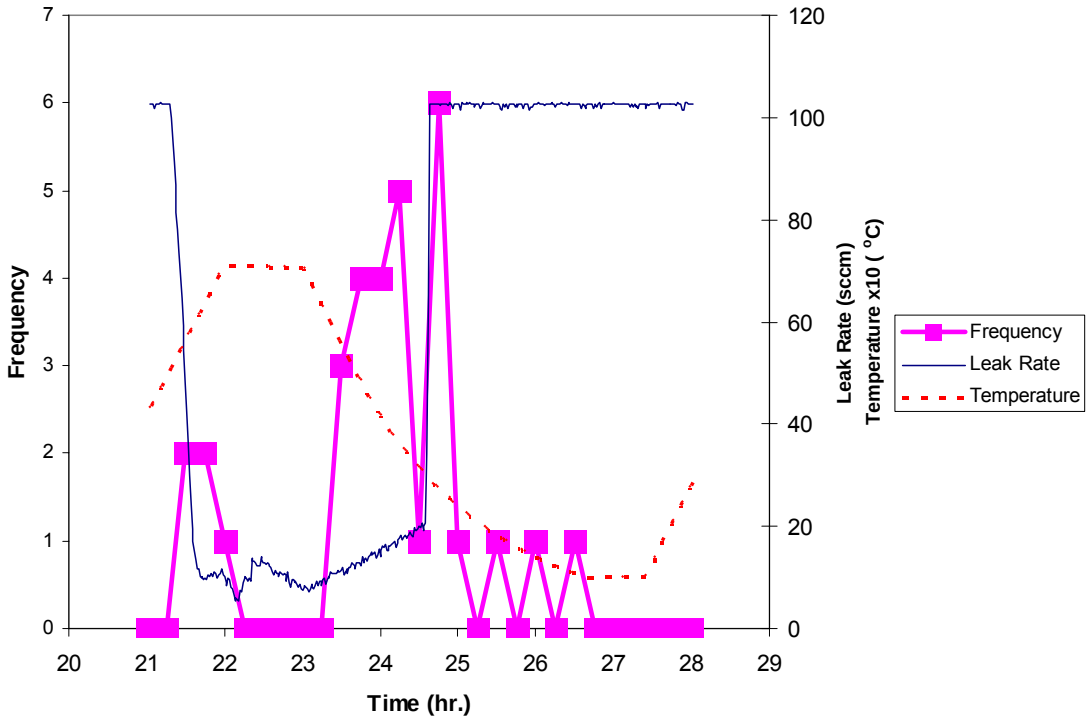

Figure 79 Cluster 3 of sample 9 thermal cycle test using O-ring versus glass PCA transformation matrix

Figure 80 shows the results from the 1-D location analysis using AE methods. The distribution for time, t=0 is very tight and corresponds well with the known initial crack position at 4 in. As the crack moves the AE distribution moves in the direction of the crack. At time, $t=t_4$, the crack tip has moved approximately 1 in. The distribution has becomes more spread out suggesting that the crack tip is no longer well defined or no longer perpendicular to the length of the metal strip. In any case, this experiment demonstrated that crack location sensing for SOFC seals is feasible.

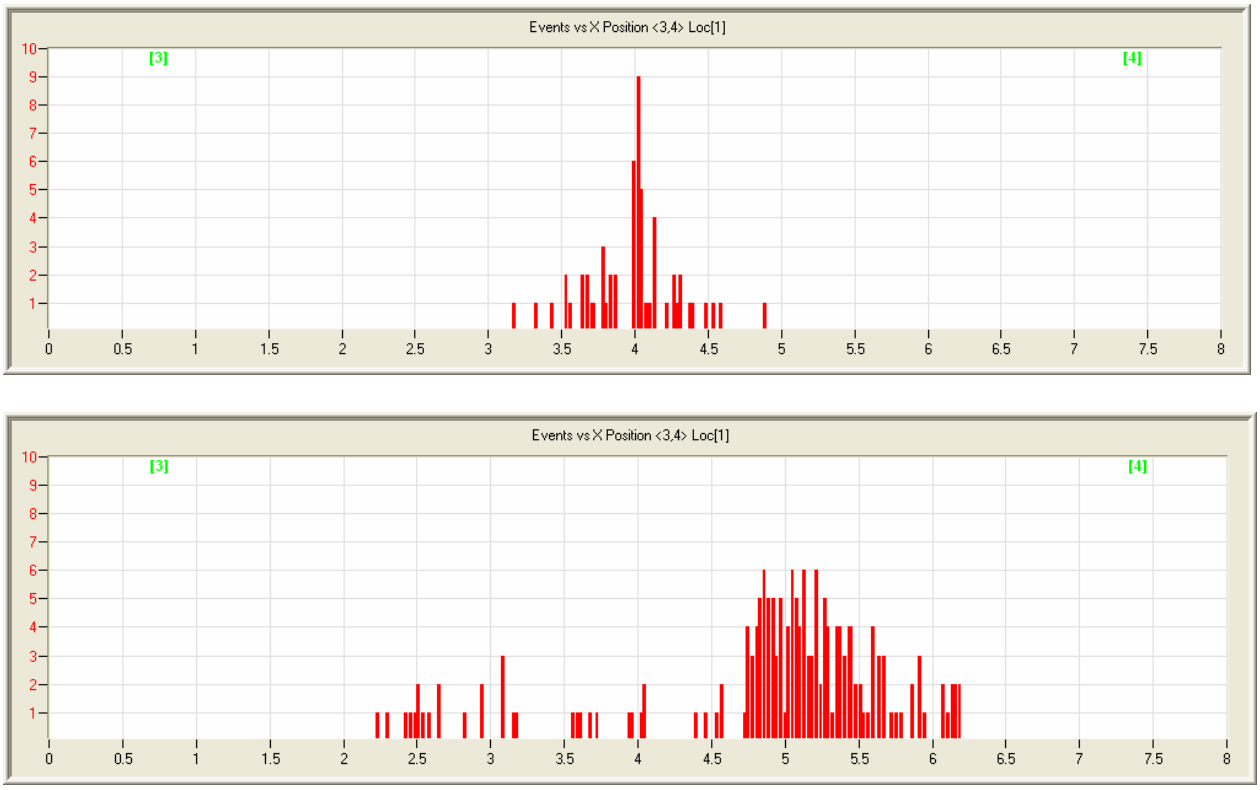

Figure 80 1-D crack tip movement determination using AE methods: Top: t0 Bottom: t4

Acousto-Ultrasound (AU)

Experimental Setup

Figure 81 shows the experimental setup. Four Mini 30 sensors were mounted on four corners using about 360 mm long wave guides. The pulsers sent a chirp signal with frequency range 100-800 kHz, duration of 50 □sec and 5 V amplitude

at 2 seconds time intervals. This pulsing-receiving sequence was repeated every 30 seconds as shown in Figure 82. The pulser 1 (P1) – receiver 1 (R1) pair controlled the side identified as S1 in Figure 1, P1–R2 S2, P2-R1 S3 and P2-R2 S4. AEWin was set as TR mode (only waveforms recorded) and channels were synchronized using the pulse channel as the trigger source. Filter, sample rate, record length and pre-trigger of receiving sensors were set as 20-2000 kHz, 5 MHz, 4K and 0.

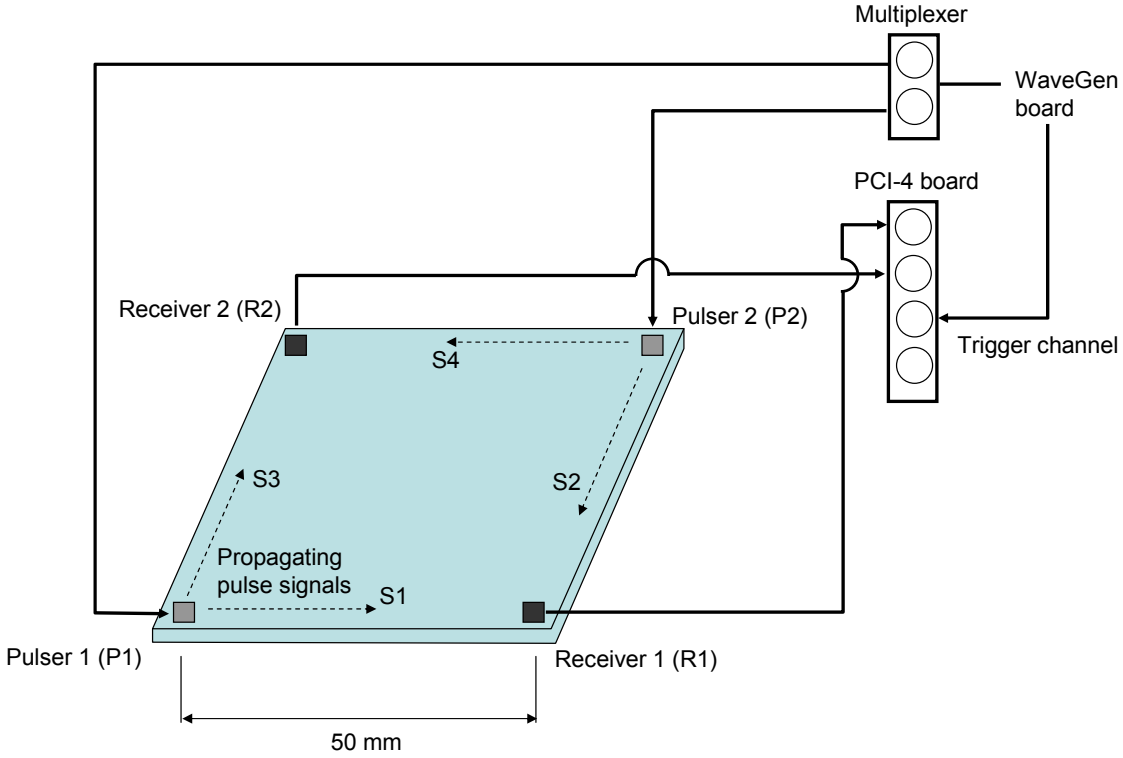

Figure 81. Experimental setup.

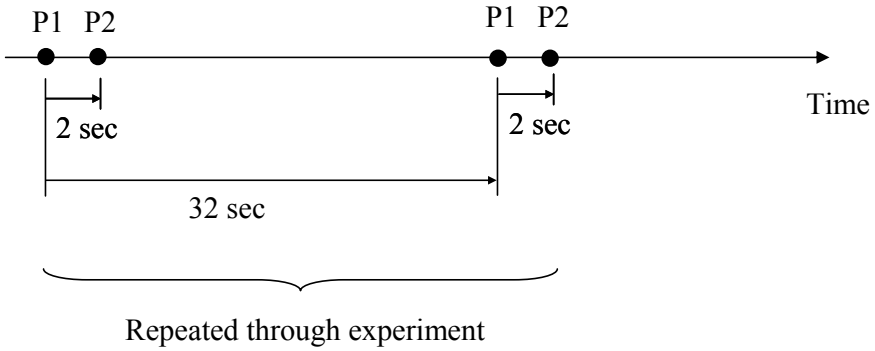

Figure 82. The pulse sequence.

Sample Description

In the AU test, the two square pieces (Figure 83. **Samples for AU test**) were bonded around the edge with SNL glass and compressed with two round platen (black colored parts in the pictures) with a fairly large force, i.e., a couple of hundred pounds. Four wave guides were attached to attached to each corner of the sample directly by welding.

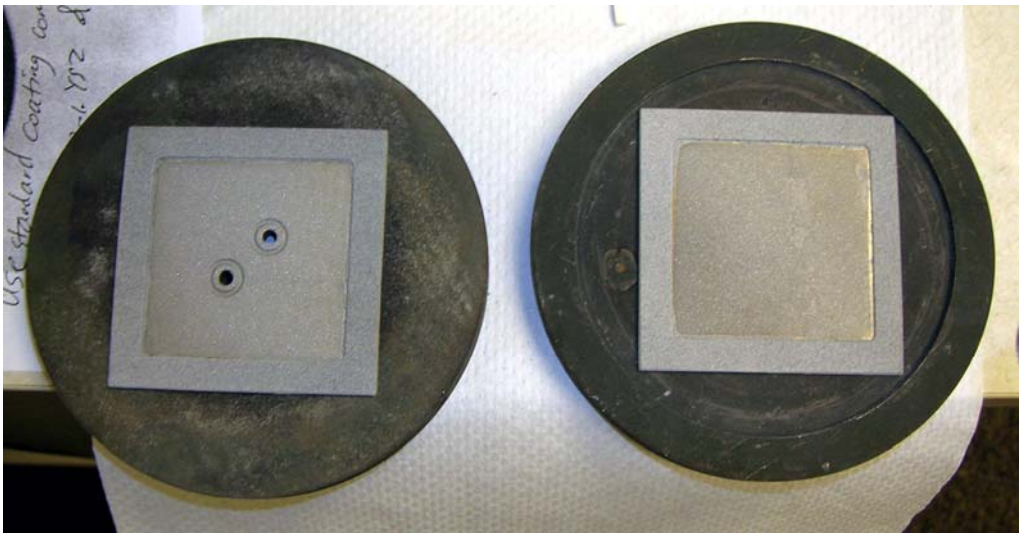

Figure 83. Samples for AU test

Experimental Results

Three experiments having different temperature loading histories were conducted:

- Case 1: Monotonically increasing temperature and returning to ambient temperature
- Case 2: Monotonically increasing temperature and starting cyclic temperature
- Case 3: Cyclic temperature loading

The responses of two receivers to each pulser are separated using the following method: If record time difference of two consecutive hits for a receiver is between 1.6 seconds and 2.4 seconds, place the first hit as receiver 1 response to pulser 1 and the second hit as receiver 1 response to pulser 2. This procedure is repeated for receiver 2 as well. Note that the responses of both receivers are separated using Noesis. There might be some hits recorded by a receiver and

clustered to a particular receiver-pulser pair due to AE sources other than AE sources generated by the pulsers. The receiving sensors were open to all other AE sources generating acoustic emissions higher than 99 dB.

CASE 1: Monotonic temperature loading

Figure 84 shows amplitudes of receivers 1 and 2 together with temperature history. Data presented in this figure include the responses of receivers to two pulsers and any other AE sources. When temperature increases, amplitude increases up to a level at a certain temperature, and then it starts to drop. When temperature is constant, signal amplitude is constant as well. At temperature about 400°C (decreasing branch), there are some AE hits which have high amplitude and high energy.

Figure 85 shows the absolute energies of receivers 1 and 2. As mentioned above, the sensors were open to any AE activity which creates acoustic emissions higher than 99 dB.

Figure 86 shows two waveforms corresponding to a high energy-high amplitude hit and a regular hit generated by a pulser. The hit generated by the pulser has a certain arrival time due to wave path between receiver-pulser; however the hit generated by other AE source has no arrival time. It is known that there was no leak in this temperature loading as shown in

Figure 87. It is also known that cooling process leads to serious cracking/debonding between sealant-plate interfaces.

AE hits recorded by two receivers as responses to each pulser are separated and presented in Figures 7 and 8. As shown in Figure 7, the signal amplitudes recorded at side 1 (S1-receiver 1&pulser 1) is smaller than those of S2 at the beginning of the experiment. The reason might be any variation in wave path between pulser and receiver, e.g., wave guide weld, sealant thickness, any material irregularity. The sensor calibration was performed before starting the experiments, and all sensors had similar frequency responses and sensitivities.

The change in amplitude at S1 at the end of experiment (end of curing process) as compared to the beginning of experiment is less than S2. This may indicate that the bonding at S2 is better than S1.

Table 18 presents the signal amplitudes for different receiver-pulser pairs at the beginning and at the end of the experiment. Except receiver 1-pulser 1 pair, the signal amplitudes were doubled at the end of experiment as the sealant was in solid state. At the beginning, the sealant was pasted between two plates and compressed with 5 psi force. At the end, the sealant provided good bond between two plates. This can be interpreted as that at the beginning, acoustic waves propagated through a single plate while some energy passed to sealant and led to energy loss; however at the end, acoustic waves propagated through two plates bonded very well with the sealant.

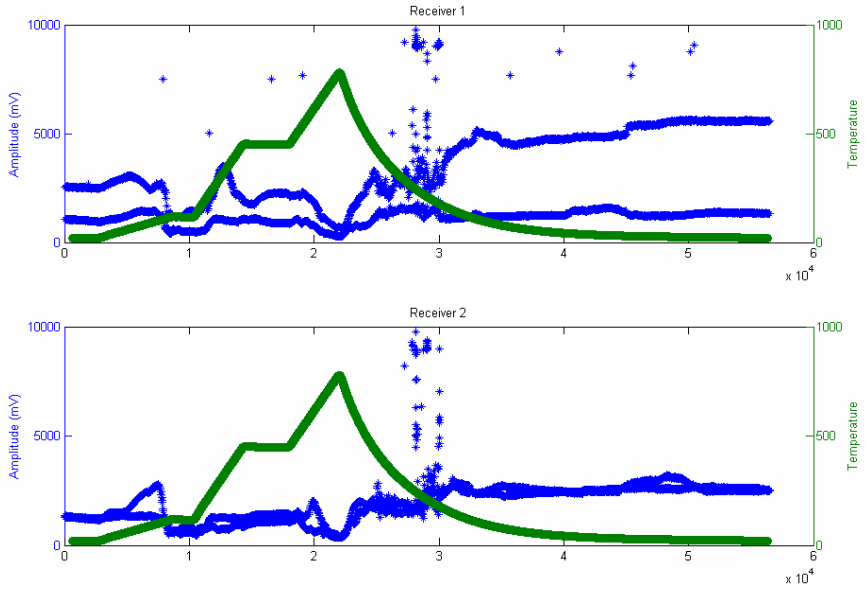

Figure 84. Amplitudes of receivers 1 and 2 together with temperature history for case 1.

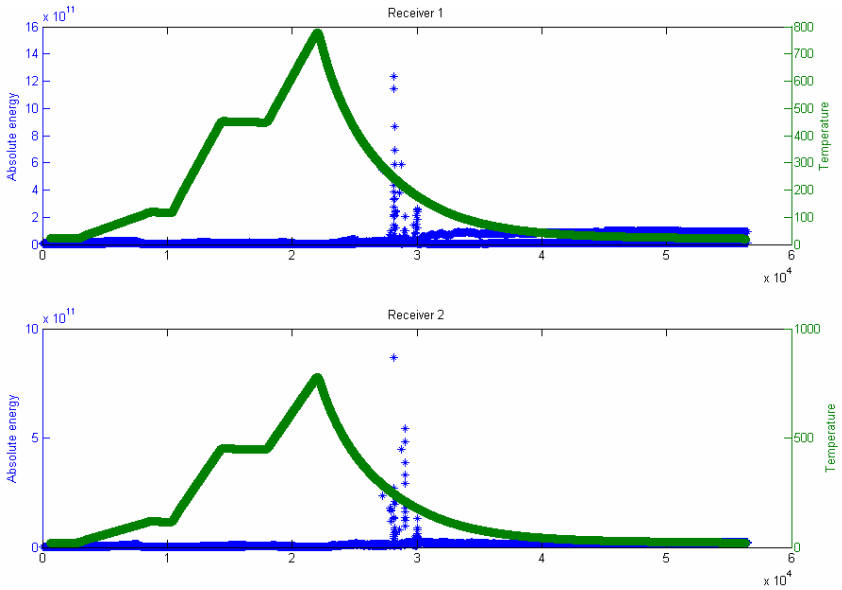

Figure 85. Absolute energies of receivers 1 and 2 together with temperature history for case 1.

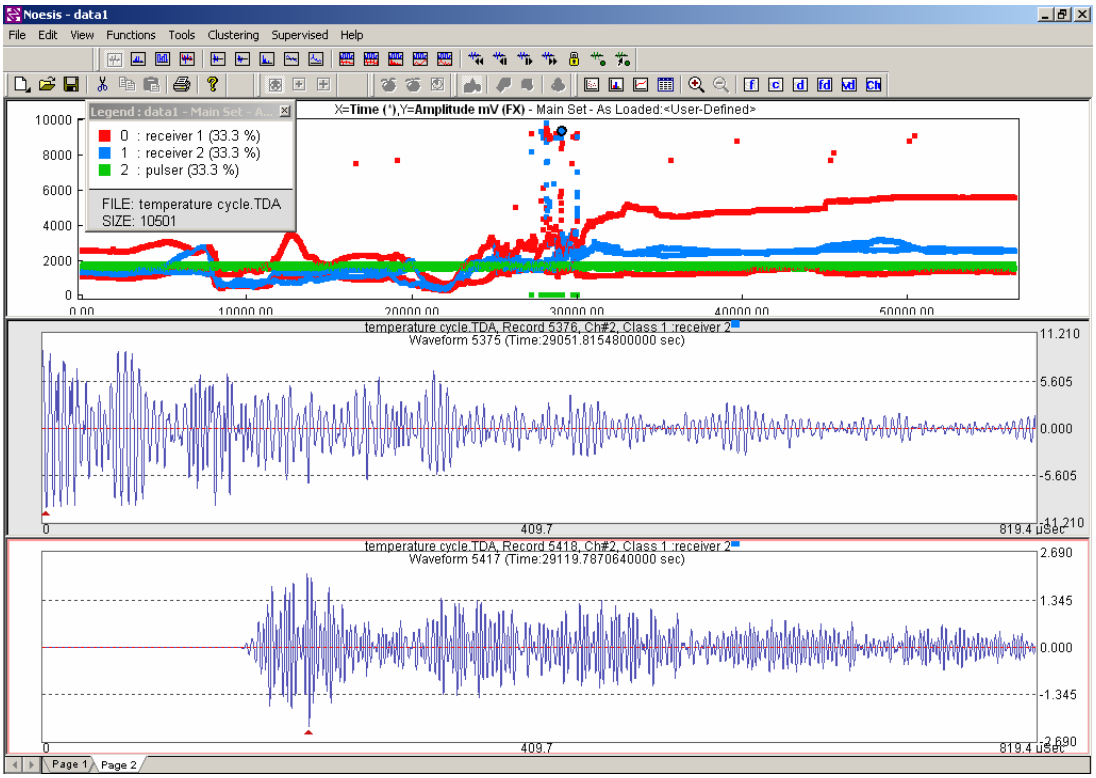

Figure 86. Amplitude distributions of three channels during case 1 and two waveforms.

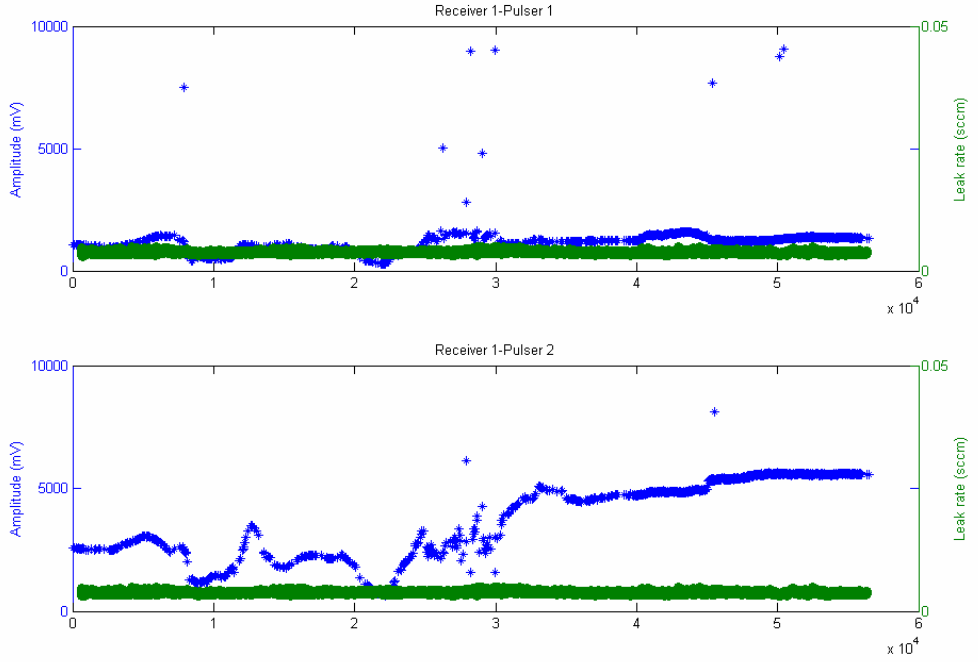

Figure 87. Amplitudes of receiver 1 as responses to pulsers 1and 2 together with leak history for case 1.

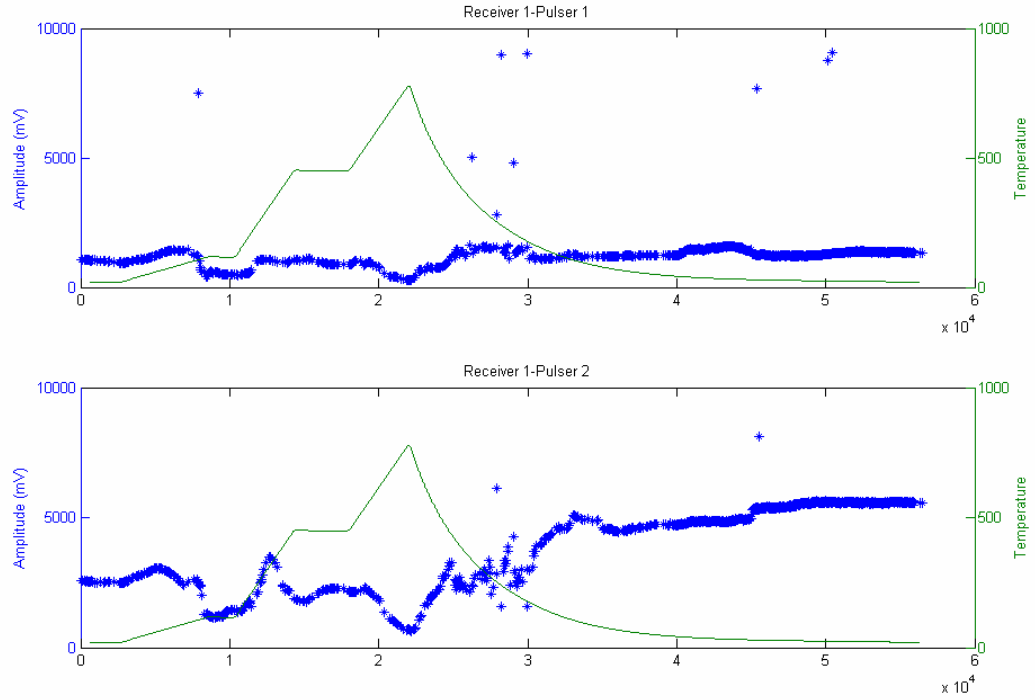

Figure 88. Amplitudes of receiver 1 as responses to pulsers 1and 2 together with temperature history for case 1.

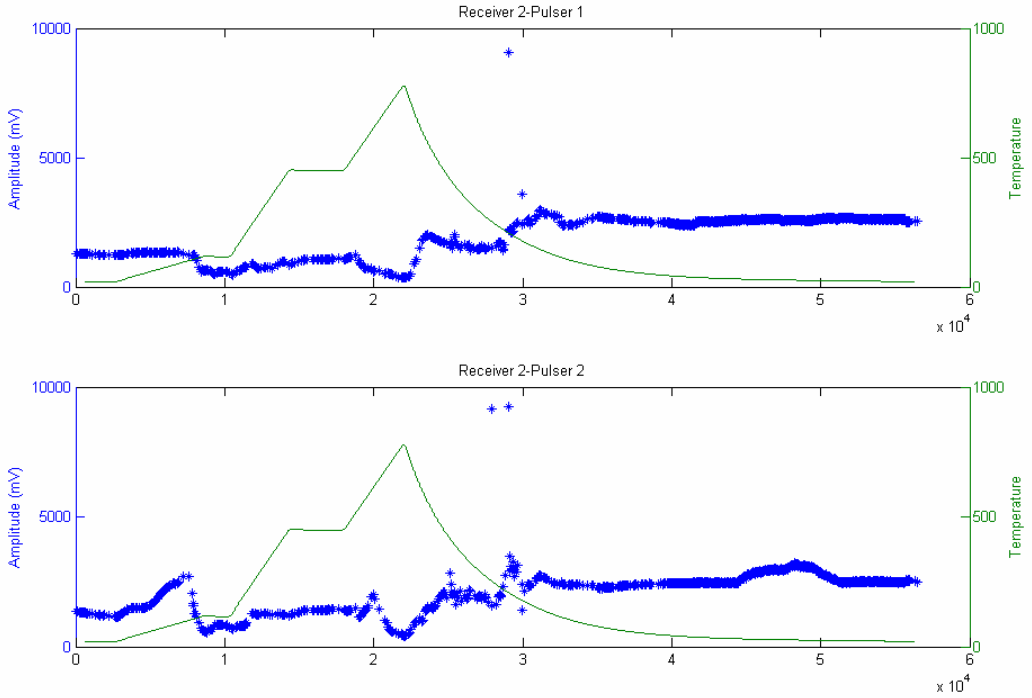

Figure 89. Amplitudes of receiver 2 as responses to pulsers 1and 2 together with temperature history for case 1.

Table 18. Signal amplitudes at the beginning and end of the experiment (case 1).

Sensor Pair	Plate Side	Initial Amplitude (V)	Amplitude at 800C (V)	Final Amplitude (V)
R1-P1	S1	1	0.3	1.4
R1-P2	S2	2.5	0.7	5.6
R2-P1	S3	1.3	0.3	2.6
R2-P2	S4	1.3	0.4	2.5

CASE 2: Monotonic temperature loading-2

Case 2 has a similar temperature loading as case 1. Figure 90 and Figure 91 show amplitude and absolute energy distributions of receivers 1 and 2 together with temperature history. At the increasing branch of temperature loading, there is no AE source other than pulse signal. However, high energy-high amplitude hits were recorded at the decreasing branch of temperature loading, starting at about 400°C. As compared to case 1, these other AE sources continued until temperature reached 200°C.

Figure 92 and Figure 93 present leak history together with amplitude distributions

of receivers 1 and 2 as responses to pulsers 1 and 2. There is significant leak when temperature reaches to maximum, and leak reaches to the maximum at 2E4 seconds and stays there. The record times of other AE hits match well with the time of occurrence of maximum leak. However, leak was very low during case 1 when other AE hits were recorded. This may indicate the formation of different types of AE sources, e.g., cracking, delamination.

Table **19** summarizes the signal amplitudes at the beginning, end and maximum temperature of the experiment. The signal amplitudes are very close at the maximum temperatures of case 1 and case 2. There is significant reduction between the beginning and end of case 2. It would be expected that if the final bond condition is the same during the transitions from solid to liquid and then liquid to solid state, the beginning and end amplitude readings of each receiver should be close. For side 2 (S2), there is about 50% amplitude reduction. This may indicate that there is serious delamination at side 2.

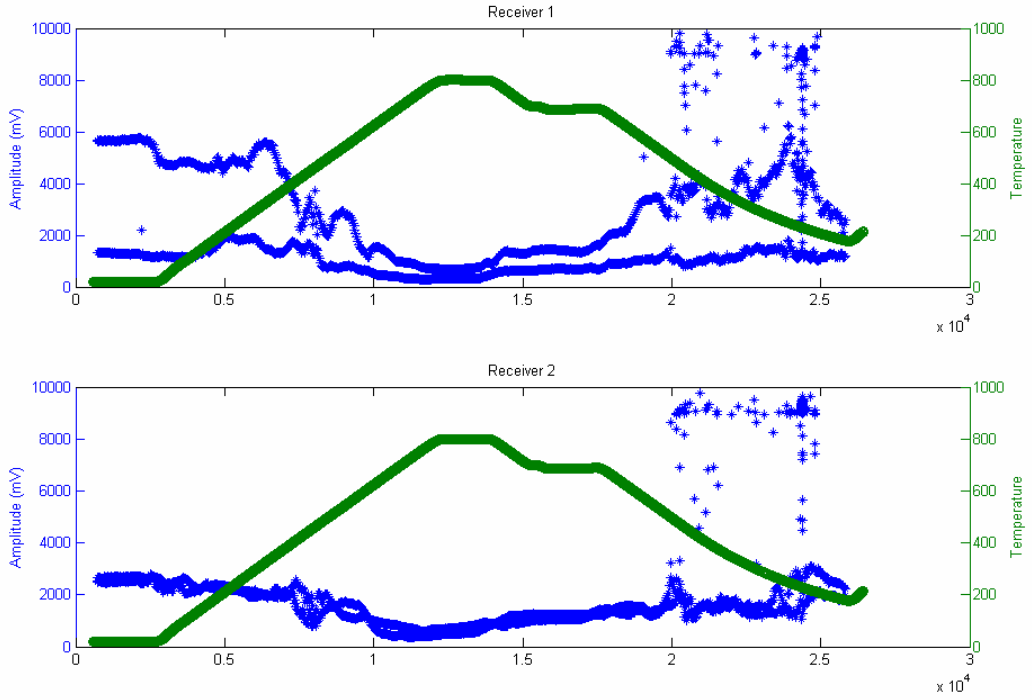

Figure 90. Amplitudes of receivers 1 and 2 together with temperature history for case 2.

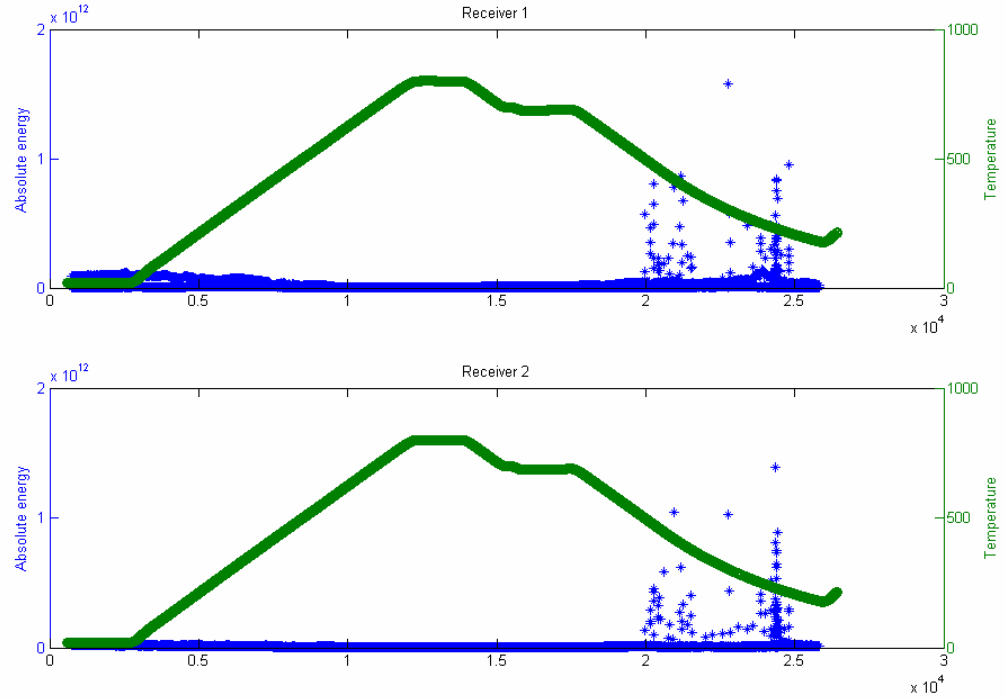

Figure 91. Absolute energies of receivers 1 and 2 together with temperature history for case 2.

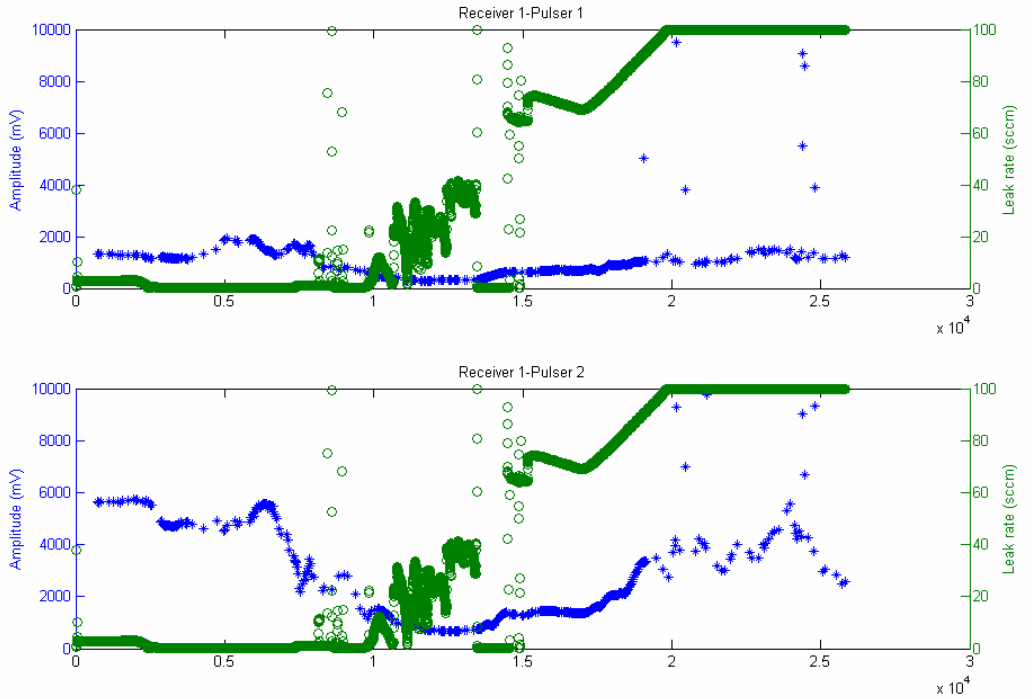

Figure 92. Amplitudes of receiver 1 as responses to pulsers 1and 2 together with leak history for case 2.

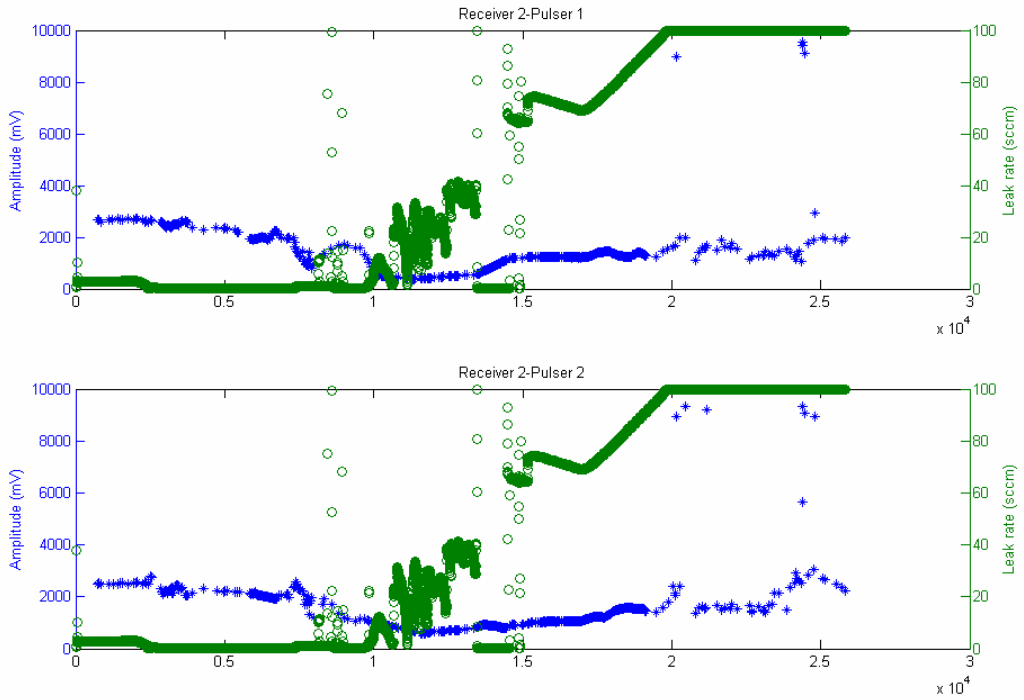

Figure 93. Amplitudes of receiver 2 as responses to pulsers 1and 2 together with leak history for case 2.

Table 19. Signal amplitudes at the beginning and end of the experiment (case 2).

Sensor Pair	Plate Side	Initial Amplitude (V)	Amplitude at 800C (V)	Final Amplitude (V)
R1-P1	S1	1.4	0.3	1.2
R1-P2	S2	5.6	0.7	2.6
R2-P1	S3	2.6	0.4	2.0
R2-P2	S4	2.5	0.7	2.2

CASE 3: Cyclic temperature loading

Figure 13 shows the amplitude distributions of three channels (receiver 1, receiver 2, pulse). There is considerable amount of AE activities created by AE sources other than pulse. In the figure, green data represents the amplitude of pulse which drops considerably during the record periods of other AE sources. These time periods correspond to the decreasing branches of temperature cycles and the highest leak values as shown in

Figure 95 and

Figure 96.

The separation of receiver-pulser pairs (Figure 16 and Figure 17) indicates that the variation in signal amplitude during the peak leak periods is more apparent for sides 2 (R1-P2) and 4 (R2-P2) as compared to sides 1 (R1-P1) and 3 (R2-P1). This may indicate that delamination occurred at sides 2 and 4.

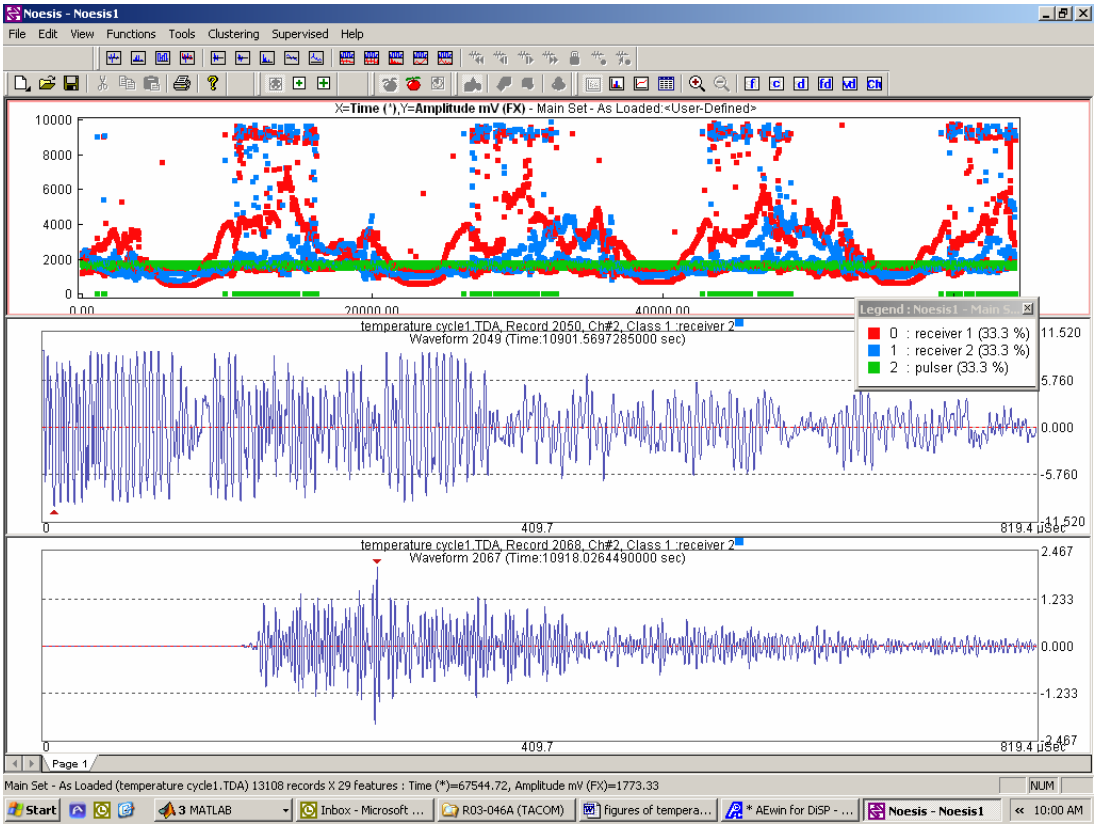

Figure 94. Amplitude distributions of three channels during cyclic temperature loading and two waveforms.

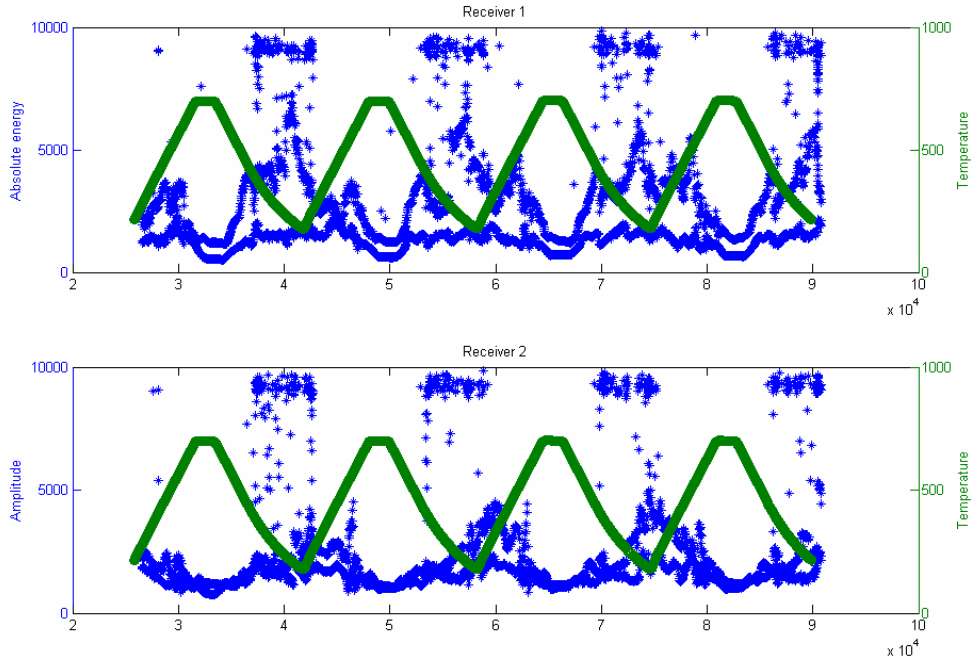

Figure 95. Amplitudes of receivers 1 and 2 together with temperature history for case 3.

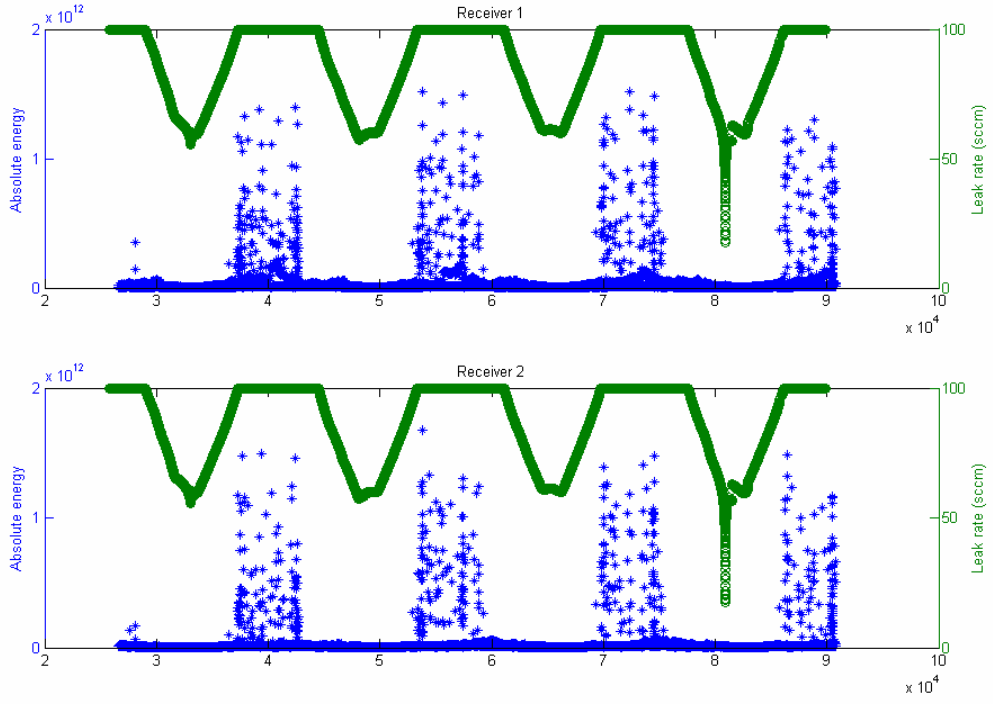

Figure 96. Absolute energy distributions of receivers 1 and 2 together with leak

history for case 3.

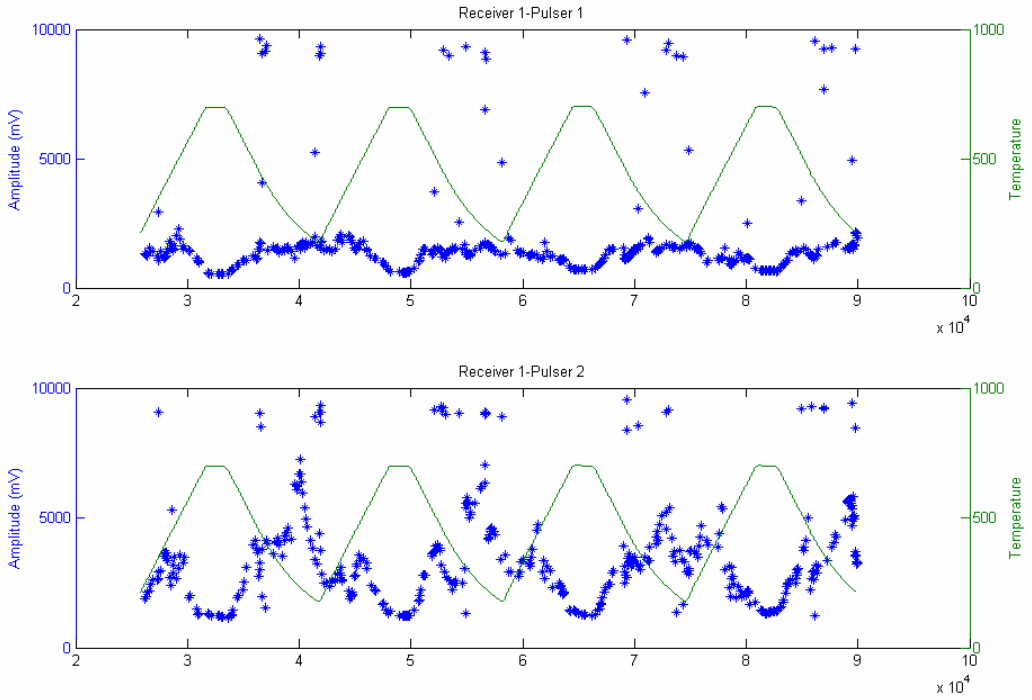

Figure 97. Amplitudes of receiver 1 as responses to pulsers 1and 2 together with temperature history.

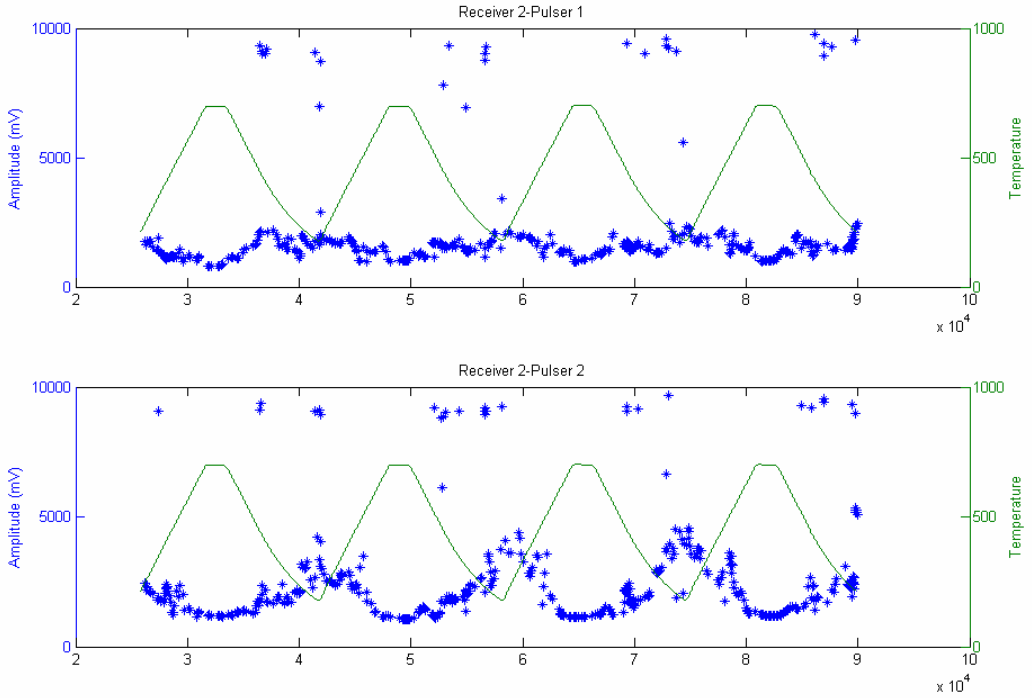

Figure 98. Amplitudes of receiver 2 as responses to pulsers 1and 2 together with temperature history.

In conclusion, AE provided clear indication when the cracking of seal occurred during thermo-cycling. And AU test was demonstrated to be able to provide qualitatively information about where cracking occurred (on which edge). However, noises and coarse location accuracy can mask the results and it remains fairly difficult to interpret test data without extensive training of the algorithms and running numerous control tests.

GRAPHICAL MATERIALS LIST(S)

LIST OF ACRONYMS AND ABBREVIATIONS

AE – Acoustic Emission
APS – atmospheric plasma spray
ASR – Area specific resistance
CTE – Coefficient of thermal expansion
CGFCC—Connecticut Global Fuel Cell Center
EPMA – electron probe micro analysis
PCA – principal component analysis
PNNL – Pacific Northwestern National Lab
sccm – standard cubic centimeter per minute
SEM – scanning electron microcopy
SOFC – solid oxide fuel cell
XRD – X-ray diffraction
YSZ – yttria stabilized zirconia

REFERENCES

1 S.-H. Leigh, C.-K. Lin, C. Berndt, Elastic response of thermal spray deposits under indentation tests, *Journal of America Ceramics Society* [8] 2093-99 (1993)

2 A.C. Fox, T.W. Clyne, Oxygen transport by gas permeation through the zirconia layer in plasma sprayed thermal barrier coatings, *Surface and Coatings Technology* 184 (2004) 311-321

3 D.A. Nield, A. Bejan, *Convection in a Porous Media,* Springer-Verlag New York, Inc. 1992 pp. 3-9.

4 Y.-S. Chou, J. Stevenson, L. Chick, Ultra-low leak rate of hybrid compressive mica seals for solid oxide fuel cells, *Journal of Power Sources* 112 (2002) 130-136.

5 S. Simner, J. Stevenson, Compressive mica seals for SOFC applications, *Journal of Power Sources* 102 (2001) 310-316.

6 W.Fergus, "Sealants for solid oxide fuel cells," *Journal of Power Sources* 147

7 Y.-S.Chou, J. Stevenson, L.A. Chick, Novel compressive mica seals with metallic interlayers for solid oxide fuel cell applications, *Journal of American Ceramic Society* 86 (6) (2003) 1003-1007

8 S. Misture, S. DeCarr, Interaction of sealing glasses with metallic interconnects in solid oxide and polymer fuel cells, Center for environmental and energy research at Alfred University Project Summary May 2005

9 K. Eichler, G. Solow, P. Otschik, W. Shaffrath, BAS (BaO-Al_2O_3-SiO_2)-glasses for high temperature applications*, Journal of the European Ceramic Society* 19 (1999) 1101-1104

10. I.Hofinger, M.Oechsner, H.A.Bahr, M.V.Swain,"Modified four-point bending specimen for determining the interface fracture for thin, brittle layers," *Int. J.Frac.* 92 (1998) 213.

11. Anderson.T.L, "Fracture Mechanics:Fundamentals and Applications", CRC Press (1995)

12. Hutchinson.J.W, Suo.Z, "Mixed mode cracking in layered materials", *Advances in Applied Mechanics*, 29 (1992) 63

13. Dundurs.J "Mathematical theory of dislocation", ASME New York (1969) 828

14. Suo.Z,Hutchinson.J.W,"Interface crack between two elastic layers", *Int. Journal of Fracture*, 43 (1990) 1

15. Suo.Z,Hutchinson.J.W,"Sandwich test specimens for measuring interface crack toughness", *Material Science and Engineering* A107 (1989) 135

16. Gu.P."Multilayer material with an interface crack", *Trans. Of the ASME* 60(1993) 1052

17. Charalambides.P.G, Lund.J, Evans.A.G.,McMeeking.R.M,"A test specimen for determining the fracture resistance of bimaterial interfaces", *ASME Journal of Applied Mechanics*, 56 (1989) 77

18. Ritter.J.E, Lardner.T.J, Stewart.A.J, Prakash.G.C,"Crack propagation in adhesive/glass sandwich specimens*", J.Adhesion*, 49 (1995) 97.

19. Gere.J.M. "Mechanics of materials", Thomson Learning, (2001)

20. Rice.J.R,"A path independent integral and the approximate analysis of strain concentration by notches and cracks", *Journal of Applied Mechanics*, 35 (1968) 379.

21. Shih.C.F., Asaro.J, "Elastic-Plastic Analysis of Cracks on Bimaterial Interfaces: Part I—Small Scale Yielding," *Journal of Applied Mechanics*, (1988) 299

22. Rice. J.R, "Elastic fracture mechanics concepts for interfacial cracks", *ASME Journal of Applied Mechanics*, 55 (1988) 98

23. J.W.Fergus, "Sealants for solid oxide fuel cells", *J.Pow. Sources* 147 (2005) 46.

24. N.Lahl, D.Bahadur, K.Singh, L.Singheiser, K.Hilpert, *J.Electrochem.Soc.* 149 (2002) A607

25. Z. Yang, M.S. Walker, J. Hardy, G. Xia, and J.W. Stevenson: "Structure and Electrical Conductivity of Thermally Grown Scales on Ferritic Fe-Cr-Mn Steel for SOFC interconnect Applications," submitted to the *Journal of Electrochemical* Society, 2003.

26 R. Miller, P. McIntire, *Nondestructive Testing Handbook 2nd Edition*, American Society for Nondestructive Testing (1987)

27 N.R. Shakar, C.C. Berndt, H. Herman, Failure and acoustic emission response of plasma-sprayed ZrO_2-8 wt% Y_2O_3 coatings, Dept. of Materials Science and Engineering

28 C.C. Berndt, Acoustic emission evaluation of plasma-sprayed thermal barrier coatings,

Journal for Gas Turbines and Power, 107 (1985) 142-146
29 N. R. Shankar, C. C. Berndt, H. Herman, Acoustic emission from thermally cycled plasma-sprayed oxides, *American Ceramic Society Bulletin* 62 (1983) 614-618
30 C.-K. Lin, C.C. Berndt, Acoustic emission studies on thermal spray materials, *Surface and Coatings Technology* 102 (1998) 1-7
31 K. Sato, T. Hashida, K. Yashiro, H. Yugami, T. Kawada, J. Mizusaki, Mechanical damage evaluation of solid oxide fuel cells under simulated operating conditions, *Journal of the Ceramic Society of Japan* 113 [8] (2005) 562-564
32 S. Rippengil, K Worden, K.M. Holdford, R. Pullin, Automatic classification of acoustic emission patterns, *Strain* (2003) 39, 31-41
33 V. Emamian, M. Kaveh, A. H. Tewfik, Z. Shi, L. J. Jacobs, J. Jarzynski, Robust clustering of acoustic emission signals using neural networks and signal subspace projections, *Journal of Applied Signal Processing* 3 (2003) 276-286
34 G. Manson, K Worden, K. Holford, R. Pullin, Visualization and dimension reduction of acoustic emission data for damage detection, *Journal of Intelligent Material Systems and Structures* 12 (2001) 529-535
35 A. Rencher, *Methods of Multivariate Analysis,* John Wiley & Sons, Inc. 1995 pp.415-442